



**REHABILITATION OF OLD FRANCIS TURBINES USING REVERSE
ENGINEERING AND COMPUTATIONAL FLUID DYNAMICS
SIMULATIONS**

OĞUZHAN ULUCAK

SEPTEMBER 2020

**REHABILITATION OF OLD FRANCIS TURBINES USING REVERSE
ENGINEERING AND COMPUTATIONAL FLUID DYNAMICS
SIMULATIONS**

**A THESIS SUBMITTED TO THE GRADUATE SCHOOL OF NATURAL
AND APPLIED SCIENCES OF CANKAYA UNIVERSITY**

BY

OĞUZHAN ULUCAK

**IN PARTIAL FULFILLMENT OF THE REQUIREMENTS FOR
THE DEGREE OF MASTER OF SCIENCE IN
MECHANICAL ENGINEERING**

SEPTEMBER 2020


STATEMENT OF NON-PLAGIARISM PAGE

I hereby declare that all information in this document has been obtained and presented in accordance with academic rules and ethical conduct. I also declare that, as required by these rules and conduct, I have fully cited and referenced all material and results that are not original to this work.

Name, Last name: OĞUZHAN ULUCAK

Signature

:



Date

:

15.09.2020

ABSTRACT

REHABILITATION OF OLD FRANCIS TURBINES USING REVERSE ENGINEERING AND COMPUTATIONAL FLUID DYNAMICS SIMULATIONS

OĞUZHAN ULUCAK

M.Sc., Department of Mechanical Engineering

Supervisor: Assist. Prof. Dr. Ülkü Ece AYLI İNCE

Co-Supervisor: Assist. Prof. Dr. KUTAY ÇELEBİOĞLU

SEPTEMBER 2020, 129 Pages

In the last decades, the refurbishment and upgrading of hydro-turbines have been increasingly demanded due to the performance loss, reliability reduction, and frequent maintenance need. Before, starting the rehabilitation process, a key point is presenting the state of the power plant. Without understanding the current problems, which cause a reduction in efficiency, generated power and reliability, starting the rehabilitation process can cause unnecessary expenses and modification to the units with no substantial increase in the performance. The objective of this research is to undertake Computational Fluid Dynamics analyses of selected hydroelectric power plants for the purpose of evaluating upgrade potential as well as identification of operational characteristics. For this purpose, turbine parts were scanned in the field then a hybrid reverse engineering methodology were developed which combines the traditional reverse engineering steps with the flow dynamics of hydraulic turbines. Steady state analyses are performed to determine the efficiency and power output of the turbine. A hill chart is generated to investigate the behavior of the turbine at different head and flow rate values. Obtained CFD results are compared with the site measurements. The CFD results showed that at the full-load condition the turbine has

93.8% efficiency with 51.56 MW power output which are consistent with the guaranteed values from manufacturer. In the sixth part of the study, the problems that decrease the turbine efficiency are detected by performing transient analysis. According to the CFD results, cavitation zones are observed on the runner blades and these zones also matches with the site photos. Transient analysis and visualization techniques are used for diagnostics of turbine which enabled identification of different cavitation mechanisms. Results depicted that blades suffers from cavitation close to the trailing edge. In addition to this, especially at the part load conditions, powerful draft tube swirl is observed, and it is reason of the severe vibrations in the powerhouse. It is recommended that modifying the conventional runner blade to the X-blade will increase the performance and prevent the cavitation. With the additional fins on the draft tube cone or with the pressurized water injections system draft tube performance can be increase and this will also cause that turbine operate more stable and efficient.

Keywords: Rehabilitation, CFD, Reverse Engineering, Francis Turbine, Renewable Energy, Transient Analysis

ÖZ

TERSİNE MÜHENDİSLİK VE HESAPLAMALI AKIŞKANLAR DİNAMIĞI KULLANILARAK ESKİ FRANCİS TURBİNLERİN REHABİLİTASYONU

OĞUZHAN ULUCAK

Yüksek Lisans, Makine Mühendisliği Anabilim Dalı

Danışman: Assist. Prof. Dr. Ülkü Ece AYLİ İNCE

Eş-Danışman : Dr. Kutay ÇELEBİOĞLU

EYLÜL 2020, 129 SAYFA

Son yıllarda, performans kaybı, güvenilirlik azalması ve sıklıkla bakım ihtiyacı nedeniyle su türbinlerin yenilenmesi ve yükseltilmesi giderek daha fazla talep edilmektedir. Rehabilitasyon sürecine başlamadan önce, santralin mevcut durumunu gösteren çalışmalar yapılması önem arz etmektedir. Verimlilik, üretilen güç ve güvenilirlikte azalmaya neden olan mevcut sorunları anlamadan rehabilitasyon sürecini başlatmak, performansta önemli bir artış olmadan ünitelerde gereksiz masraflara ve değişikliklere neden olabilir. Bu araştırmanın amacı, iyileştirme potansiyelini değerlendirmek ve operasyonel özelliklerin belirlenmesi amacıyla seçilen hidroelektrik santrallerinin Hesaplamalı Akışkan Dinamiği analizlerini yapmaktır. Bu amaçla öncelikle türbin parçaları sahada taranmış ve geleneksel tersine mühendislik adımlarını hidrolik türbinlerin akış dinamikleri ile birleştiren hibrit bir tersine mühendislik metodolojisi geliştirilmiştir. Beşinci bölümde, türbinin verimini ve güç çıkışını belirlemek için zamandan bağımsız analizler yapılmıştır ve böylece türbinin farklı düşü ve debi değerlerinde davranışını incelemek için bir tepe diyagramı oluşturulmuştur. Elde edilen HAD sonuçları saha ölçümleri ile karşılaştırılmıştır. HAD sonuçları, tam yük durumunda türbinin, üreticinin garantili

değerleri ile tutarlı olan 51,56 MW güç çıkışı ile%93,8 verimliliğe sahip olduğunu göstermektedir. Çalışmanın altıncı bölümünde, türbin verimini düşüren sorunlar zamana bağlı analizler yapılarak tespit edilmiştir. HAD sonuçlarına göre, çark kanatlarında kavitasyon bölgeleri görülmektedir. Farklı kavitasyon mekanizmalarının tanımlanmasını sağlayan türbin teşhisi için geçici analiz ve görselleştirme teknikleri kullanılmaktadır. Sonuçlar, saha fotoğraflarında da görüldüğü üzere, kanadın, kuyruk kenarına yakın noktalarda kavitasyon olduğunu göstermektedir. Buna ek olarak, özellikle kısmi yük koşullarında, emme borusunda şiddetli girdaplar olduğu görülmektedir ve bu olgu santraldeki şiddetli titreşimlerin sebebidir. Geleneksel çark kanadının X-kanadına değiştirilmesinin performansı artırması ve kavitasyonu önleyeceği öngörülmektedir. Emme borusu konisi üzerindeki ilave kanatçıklar veya basınçlı su enjeksiyon sistemi ile çekiş borusu performansı artırılabilir ve bu da türbinin daha kararlı ve verimli çalışmasına neden olacaktır.

Keywords: Rehabilitasyon, HAD, Tersine Mühendislik, Francis Türbini, Yenilenebilir Enerji, Zamana-Bağlı Simulasyon



To My Mother

ACKNOWLEDGEMENTS

This research would not have been possible without the gracious support I have received throughout my time working on this thesis. I would first like to thank my thesis advisor Assist. Prof. Dr. Ulku Ece AYLI INCE whose continued assistance guided me throughout my work. I am also grateful to Dr. Kutay CELEBIOGLU who would not only teach me about turbines, creative problem solving, and perseverance in research, but who would also provide guidance and personal support.

I would also like to express appreciation to head of the TED University Mechanical Engineering Department, Prof. Dr. Selin ARADAG. Lastly, Cankaya University and our department head Prof. Dr. Hasmet Turkoglu for their support throughout my thesis.

I am grateful to the European Union for initiating and funding this work, and to EUAS for sharing their know-how with us.

Above all, I am thankful for my mother, for her support and encouragement to me during my study.

TABLE OF CONTENT

ABSTRACT

ÖZET

ACKNOWLEDGEMENTS

TABLE OF CONTENTS

LIST OF TABLES

LIST OF FIGURES

LIST OF ABBREVIATIONS

LIST OF SYMBOLS

1	CHAPTER 1	17
1.1	MOTIVATION AND AIM OF THE THESIS	17
1.2	LITERATURE SURVEY	20
1.2.1	Cavitation.....	22
1.2.2	Reverse Engineering	25
1.3	CONTRIBUTION TO LITERATURE	26
2	CHAPTER 2	27
2.1	DEFINITION OF THE PROBLEM	27
2.2	THEORETICAL BACKGROUND.....	28
2.2.1	Coordinate System	28
2.2.2	Turbine Efficiency	29
2.2.3	Spiral Case and Guide Vane Efficiency.....	30
2.2.4	Flow Kinematics for Francis Turbine	30
2.2.5	Turbine Energy Equation.....	32
2.2.6	Pressure Recovery Factor	33
3	CHAPTER 3	34
3.1	REVERSE ENGINEERING METHODOLOGY	34
3.1.1	3D Digitalization	35
3.1.2	CAD Model Creation	36
3.1.3	Determination of Blade Design Parameters	37
3.2	NUMERICAL METHODOLOGY.....	39
3.2.1	Governing Equations	42
3.2.2	Advection Schemes	45
3.2.3	Boundary Conditions	45
3.2.4	Static Pressure Boundary Condition	46
3.3	SIMULATION STRATEGY.....	46
3.4	Post Process Methods and Tools.....	47
3.4.1	Cavitation, Cavitation Types and Thoma Number	47

3.4.2	Fast Fourier Transform	50
4	CHAPTER 4.....	52
4.1	UTILIZATION OF REVERSE ENGINEERING APPROACH FOR TURBINE PARTS	52
4.1.1	Runner.....	52
4.1.2	Guide Vanes and Stay Vanes.....	57
4.1.3	Verification with IEC Standards and Model Runner	58
4.1.4	Drawings for Draft Tube And Spiral Case	61
4.1.5	3D Geometric Model of The Gezende.....	65
5	CHAPTER 5.....	67
5.1	COMPONENT-BASED CFD ANALYSIS	68
5.1.1	Mesh Independency Study.....	69
5.2	FULL TURBINE STEADY STATE CFD ANALYSIS	71
5.3	DETERMINATION OF OFF-DESIGN PERFORMANCE OF THE TURBINE	82
5.4	LOSSES IN THE GEZENDE HPP AND COMPARISON OF THE CFD RESULTS WITH REAL DATA.....	84
6	CHAPTER 6.....	86
6.1	INTRODUCTION.....	86
6.2	THE METHODOLOGY OF THE TRANSIENT ANALYSIS	86
6.3	EVALUATION OF TRANSIENT HYDRAULIC FEATURES IN FLUID DOMAIN	89
6.3.1	Transient Hydraulic Features in Fluid Domain	92
7	CHAPTER 7.....	100
7.1	PRESSURE DISTRIBUTION AND SWIRL FORMATION IN THE DRAFT TUBE.....	100
7.2	AXIAL AND CIRCUMFERENTIAL VELOCITY DISTRIBUTION	105
7.3	PRESSURE RECOVERY FACTOR EFFECT ON TURBINE PERFORMANCE	111
7.4	COMPARISON OF STEADY AND UNSTEADY RESULTS.....	117
8	CHAPTER 8.....	118
	REFERENCES	121

LIST OF TABLES

Table 2-1: Gezende HPP Characteristics	27
Table 4-1: Comparison between reverse engineering blade and scanned blade	60
Table 4-2: Performance Comparison between reverse engineering blade and scanned	61
Table 4-3: Measurements of the Spiral Case of Gezende HPP	62
Table 5-1: Mesh independency results for turbine components	71
Table 5-2: Performance comparison for CFD and field measurements	85
Table 6-1: Time Variables.....	88
Table 6-2: Problems identified in powerhouses together with specific reason.....	88
Table 6-3: Passing Frequencies.....	92
Table 7-1: Component Based Efficiency Table and Cp (Full Turbine).....	113
Table 7-2: Cp variations with the Volume Flow Rate	114
Table 7-3: Performance comparison between transient (average) and steady state.	117

LIST OF FIGURES

Figure 1.1 : Cavitation formation regions [adapted from 32]	23
Figure 2.1: Gezende HPP Site View	28
Figure 2.2 : Coordinate System	29
Figure 2.3: Velocity Triangles for Radial Flow Turbine Runner [adopted from 20]	31
Figure 2.4: Velocities at the Edge of the Runner Blade [adopted from 20]	33
Figure 3.1: Flow chart of the Reverse Engineering Process	35
Figure 3.2 :Reference Blocks	36
Figure 3.3 : Scanning of the turbine runner	36
Figure 3.4: (a) Scanning (b) Point cloud (c) Solid model of the guide vane	37
Figure 3.5: Meridional profile of the runner blade	37
Figure 3.6: View of the flow angles in the camber line	38
Figure 3.7: (a) Machine Gezende (b) Mesh Structure	41
Figure 3.8: CFD Methodology	42
Figure 3.9: DaVinci Turbulent flow sketch	43
Figure 3.10: Phase Diagram for a Simple Substance	48
Figure 3.11: Cavitation in Francis Turbines (a)leading-edge cavitation (b) traveling edge cavitation (c) draft tube swirl cavitation (d) Inter-blade vortex cavitation [adapted from 32]	50
Figure 4.1: Runner reverse engineering procedure	53
Figure 4.2: View of the meridional profile	53
Figure 4.3: Sectional Drawing of the Francis Runner	54
Figure 4.4 : Meridional section of the scanned runner	55
Figure 4.5: Defined spans on the blade	55
Figure 4.6 : (a) Thickness definition (b) Camber Line definition	56
Figure 4.7: Thickness, Wrap Angle, Metal Angle distribution of Gezende HPP runner	57
Figure 4.8 : Solid model of the Guide vane	58
Figure 4.9: (a) The Flow Field of The Guide Vane (b) Solid Model of The Guide vane	58
Figure 4.10 : (a) Scanned Blade (b) Reverse Engineered Blade (c) Superposed Blades	59
Figure 4.11 : Geometry Generation Process for Spiral Case	63
Figure 4.12: Buffer vane of the spiral Case	63
Figure 4.13 : Solid model of the Spiral Case	63
Figure 4.14 : Technical Drawing of Draft tube	64
Figure 4.15: Technical Drawing of Elbow	64
Figure 4.16: The geometry of Draft Tube	65
Figure 4.17: Additional Cone for Runner	65

Figure 4.18: Full turbine of the Gezende HPP	66
Figure 5.1 : Mesh Structures for components of the Gezende	67
Figure 5.2: CFD Methodology	68
Figure 5.3: Mesh refinement regions for (a) Spiral case (b) Draft tube.....	69
Figure 5.4: Mesh Refinement Regions For Runner Blades	70
Figure 5.5: Mesh Refinement Regions For Guide Vanes	70
Figure 5.6: Simulation process for Gezende Hill Chart.....	72
Figure 5.7: CFD operating conditions to obtain Hill Chart	73
Figure 5.8: Hill Chart for GEZENDE HPP with BEP point.....	73
Figure 5.9: Operating region for GEZENDE HPP	74
Figure 5.10: For different loadings Thoma number distribution through the runner (a) 68% loading (b) 87 % loading (c) 101 % loading (d) 110 % loading	75
Figure 5.11: a) Runner blades b) Thoma Number distribution.....	76
Figure 5.12 : Thoma number distribution for different spans (101% loading).....	76
Figure 5.13: Pressure distribution for the runner (H=154 m, Guide Vane Opening= 25°).....	77
Figure 5.14: For full loading conditions streamlines and velocity vectors (H=154 m, guide vane opening=25°)	78
Figure 5.15: Circumferential velocity distribution from hub to shroud for 101% loading.....	79
Figure 5.16: Meridional velocity distribution from hub to shroud for 101% loading	79
Figure 5.17: Total Pressure distribution on meridional surface for 101 % loading..	80
Figure 5.18: Velocity Vectors and Magnitude in the Runner (%50)	81
Figure 5.19: Pressure distribution on the Guide Vane (%50 Span).....	81
Figure 5.20: Loading- efficiency graphic (For 154 m head).....	82
Figure 5.21: Guide vane efficiency versus turbine power output.....	83
Figure 5.22: Flow rate versus turbine power output	83
Figure 5.23: Turbine efficiency curve (H= 154 m).....	84
Figure 6.1: Operation range and selected simulation points (corners)	87
Figure 6.2: Observation points in the Draft tube	89
Figure 6.3: Observation points in the Spiral Case	90
Figure 6.4: Observation points in the blade, (Left) suction side (Right) Pressure side	90
Figure 6.5: Torque and Efficiency fluctuations with respect to time.....	91
Figure 6.6: FFT analysis for spiral casing (a) SC1 (b) SC2 (c) SC3 (d)SC4.....	93
Figure 6.7: FFT analysis for guide vane (a) GV1 (b) GV2 (c) GV3	94
Figure 6.8 : FFT analysis for runner pressure side (a) PS1 (b) PS2 (c) PS3 (d) PS4.....	96
Figure 6.9: FFT analysis for runner suction side (a) SS1 (b) SS2 (c) SS3 (d) SS4 ..	97
Figure 7.1: Draft tube pressure distribution and vortex structure for 144 m head and 19° guide vane.....	101

Figure 7.2: Draft tube pressure distribution and vortex structure for 144 m head and 27° guide vane opening.....	102
Figure 7.3: Draft tube pressure distribution and vortex structure for 154 m head and 25° guide vane opening.....	103
Figure 7.4: Draft tube pressure distribution and vortex structure for 174 m head and 19° guide vane opening.....	104
Figure 7.5: Draft tube pressure distribution and vortex structure for 174 m head and 23° guide vane opening.....	105
Figure 7.6: Defined lines on the draft tube cone.....	106
Figure 7.7: Axial and Circumferential Velocity Distribution on Line 1.....	108
Figure 7.8: Axial and Circumferential Velocity Distribution on Line 2.....	109
Figure 7.9: Axial and Circumferential Velocity Distribution on Line 3.....	110
Figure 7.10: Axial and Circumferential Velocity Distribution on Line 4.....	111
Figure 7.11: Draft tube pressure distribution and vortex structure for (a) 144 m head and 19 ° guide vane opening (b) 174 m head and 23° guide vane opening.....	112
Figure 7.12: Streamlines on the cross-sectional area for 144 meters Head 19 degree Opening.....	114
Figure 7.13 : Streamlines on the cross-sectional area for 144 meters Head 27°.....	115
Figure 7.14: Streamlines on the cross-sectional area for 154 meters Head 25 ° Opening.....	115
Figure 7.15: Streamlines on the cross-sectional area for 174-meters Head 19° Opening.....	116
Figure 7.16: Streamlines on the cross-sectional area for 174-meters Head 23 ° Opening.....	116
Figure 8.1: Process chart for the CFD study of the Gezende HPP.....	119

LIST OF ABBREVIATIONS

CAD	: Computer Aided Design
GGI	: General Grid Interface
CFD	: Computational Fluid Dynamics
IEC	: International Electrotechnical Commission
MFR	: Multiple Frames of Reference
RANS	: Reynolds Averaged Navier - Stokes
RE	: Reverse Engineering
HPP	: Hydro-Electric Power Plant
DFT	: Discrete Fourier Transform
FFT	: Fast Fourier Transform
RES	: Renewable Energy Systems

LIST OF SYMBOLS

P	Pressure
P_{atm}	Atmospheric Pressure
g	Gravity
H	Head
H_n	Net Head
Q	Volumetric Flow Rate
ρ	Density
ω	Angular Velocity
T_M	Mechanical Torque
V	Absolute Velocity
v_m	Meridional Velocity Component
v_u	Circumferential Velocity Component
M_0	Moment
H	Efficiency
Γ	Circulation
x_i^{cc}	X Coordinate of Any Point on Camber Line
y_i^{cc}	Y Coordinate of Any Point on Camber Line
z_i^{cc}	Z Coordinate of Any Point on Camber Line
θ_i	Wrap Angle
β	Metal Angle

Δt	Thickness of The Blade
U'_1	Fluctuating Component of Velocity,
\overline{U}_1	Average Velocity
φ	Dimensionless Mass Flow Rate
ψ	Dimensionless Energy
σ_p	Thoma Plant
σ_i	Thoma Number for Any Point
C_p	Pressure Recovery Factor
X_{Rms}	Root Mean Square Value of The Signal
f_N	Dimensionless Frequency Value



CHAPTER 1

INTRODUCTION

1.1 MOTIVATION AND AIM OF THE THESIS

In recent years, competitive electricity prices, the trend of electricity demand and greenhouse effect of the non-renewable energy sources forced countries to utilize renewable energy sources which are domestic and has a great potential on a local and national level without depending to the international fuel sources. RES becomes more attractive, considering that the energy sector is responsible for 95 % of atmospheric pollution as it is clean and sustainable [1]. Hydropower offers many advantages over other RES sources. It is an intermittent energy source that can respond to the fluctuations in demand for electricity. The flexibility and storage capacity of HPP make them superior when it is compared with wind or solar energy. Due to the World Energy Council [2], hydropower is the leading RES with supplying 71% off all renewable electricity. The first hydroelectrical power plant was constructed in the United States along the Fox in the 19th century [3] and spread around the world. Although the HPP have long power plant life, they need rehabilitation due to the wear, cavitation, and repairs that disturb the flow zone [4]. Nowadays, number of rehabilitation projects increase worldwide aiming to improve turbine efficiency, power output and to rise the power plant life. The efficiency of the Rio Cali I HPP, which is in operation for more than 100 years, decreases to 70 %. This efficiency value can be increased up to 93 % by using modern turbines and modern manufacturing processes [4]. Thakur [5] claimed that almost 55 % of the power stations in India needs refurbishing.

Celebioglu et al. [6][72], performed a rehabilitation project for Kepez HPP, which was constructed in 1960s. Firstly, with using Computational Fluid Dynamics (CFD) technology, they analyze the current situation of the power plant in different heads and guide vane openings. In the second stage, they rehabilitated the guide vane and runner of the old turbine. With the new design, efficiency and power generation performance is increased with better cavitation characteristics. Jackson et al. [7] revealed that turbine runner refurbishment improves reliability and rises efficiency and power generation of the turbine. Mack et al. [8], performed a modernization project for Pelton type turbine and the maximum output of the turbines got increased to 56 MW. Vitvar [9], increased the Dahua power plants power output from 103 MW to 117 MW by modifying the turbine runner with a technological one. Manjean et al. [10] switch the old mechanical governing system with the new hydraulic governor, which is more efficient and reliable. Ferme et al. [11] used a digital speed governor in the refurbishment of the Vainden power plant. They also see that the performance of the governing system increases using modern technology governors. Rahi and Chandel [12] publish a review article about the rehabilitation project of hydro power plants. Several projects are given in the area of refurbishment.

Before refinement projects, understanding and defining the problems of the current situation of the HPP is crucial. If the current situation is not defined totally, wrong investments can be done, which will not increase the efficiency, power, or power plant life. At this point, presenting the current situation accurately is as important as the rehabilitation procedure. There are several critical studies in the literature that develop a methodology to model the current situation of the power stations. Garcia et al. [13] introduce the current situation of a mini-power station in Columbia. They use a reverse engineering method for reconstruction of Francis turbine. Kaplan et al. [14] developed a methodology for reverse engineering method, and that used their methodology for a HPP which has no technical drawings. A Point cloud of the turbine runner is obtained by using laser scanning devices, and geometry is generated as a CAD model with reverse engineering methodology. In the second part of their study, they introduce the cavitation zones in the runner, incorrect inflow angle, which causes

a reduction in efficiency and power. Celebioglu and Kaplan [15], used their reverse engineering methodology on the turbine runner of Kahta HPP. They observed that reverse engineering runner and the actual runner has similar performance. As a rehabilitation suggestion, which will increase the Kahta HPP power generation from 2453 kW to 3539.6 kW, the runner is modified to zero circulation in the trailing edge. In addition, metal angles are smoothed, and curvature is defined in the hub of the blades. Zivkovic et al. [16], presents a reverse engineering procedure for turbine blades of Iron Gate I Hydroelectric Power Station, which is in operation for almost 50 years. In their reverse engineering process firstly, scanning is performed to obtain point cloud, and secondly, the Computer Aided Design (CAD) model is aligned. Then deviation calculation is utilized. Ciocănea et al. [17] obtained geometric data for a broken blade of a horizontal axis micro-hydrokinetic turbine by reverse engineering. Their new blade generates 5% more power than the old one. They claimed that to obtain accurate blade surface, a high number of points should be used in the scanning surface.

The main motivation of this study determines and define conditions of a turbine while it is operating. In other words, it is a preliminary research of the rehabilitation. This motivation brings with several pillars of study such as hydraulic performance and cavitation, general situation of the runner, mechanical vibrations, structural condition of the bearing, and electronic parts of the turbine such as sensors or other control equipment. A turbine is going to be investigated in line of vision hydraulic performance, cavitation and hydro vibration in this thesis.

In the scope of this thesis, Gezende HPP is handled in terms of the hydraulic performance by means of CFD methodology. The numerical solutions of turbine have been verified by site reports.

In the fourth part of this thesis, a method for geometry reconstruction of a Francis turbine for Gezende HPP is presented. In order to obtain the CAD models of the current parts of the turbine product scanning, surface approximation, and CAD model development steps are performed. After obtaining the CAD models and validating the reverse engineering parts with the existing turbine parts fifth part of the study starts which aims to present the current situation of the turbine with Computational Fluid Dynamics (CFD) techniques. This case study represents a general procedure about integrated reverse engineering approach of a hydraulic

turbine. In addition to that, the simulation for the whole of the parts are performed both separately to provide mesh independency and used the whole of the components as full turbine analysis. In the sixth part, transient simulations are given. Cavitation, vortices, or any other flow disorders inside the turbine flow path, are investigated in this part. In the seventh part, draft tube performance is examined in detail. Consequently, rehabilitation suggestions are discussed in eighth part to improve hydraulic performance and to reduce vibration in the powerhouse.

1.2 LITERATURE SURVEY

Hydraulics is defined as the science of the conveyance of liquids through pipes. In a hydraulic turbine, water is used as the source of energy. Hydraulic turbines convert kinetic and potential energies of the water into mechanical power.

The main types of the hydraulic turbines are impulse and reaction type turbines. In an impulse machine, all the pressure change takes place in one or more nozzles, the fluid being directed onto the rotor. The main type of the impulse type turbines is Pelton turbine. In the reaction type turbines pressure changes through the nozzle/diffuser and the rotor. The potential energy of water is converted to kinetic energy by a speed rise. Examples of the reaction turbines are Francis, Propeller and Kaplan turbines.

Francis turbine was invented in 19th century by Howd and Francis. Francis type is most common type of water turbine because they can be operated in wide range of mass flow rate and head with high efficiency values.

Francis type has 5 main different components. These are, according to water flow, spiral case, stay vanes, guide vanes, runner, and draft tube, respectively. Water comes from the reservoir through penstock and enters to the spiral case. Then, flows to the guide vanes from the gaps of the stay vanes. Finally, pressurized water arrives to the runner and gives its hydraulic energy to the runner. Water enters to runner at the radial direction and flows through to the draft tube in axial direction. After that, water is evacuated from the draft tube and exits to the river [19].

The design procedure of the hydraulic turbine components is based on the model test that are expensive and time consuming. In this context, with the development of the technology, in the hydroturbine design process, Computational Fluid Dynamics (CFD) methods become a popular, robust, and cheaper way. In literature, several

studies are performed numerically and experimentally. Also, the verification studies show that CFD is a reliable tool and gives satisfactory results when compared with the experimental studies.

Ayli et al [20] examined the effects of runner parameters on the performance. They observed that, blade theta angle, metal angle, blade thickness, and blade leaning has a direct impact on the generated power and efficiency.

Guide vanes are the component of the turbine, which is responsible to transmit the water to the runner. This component also rotatable on its own axis and mass flow rate inside the turbine is adjusted with changing guide vane opening angle. Outlet flow angle and optimum guide vane opening angle are the most important parameters in the guide vane design [21,22].

According to Akin [23] and Ayancik [24] starting to design process with runner is the most useful way as it is the major component and controls the power output. Efficient turbine runner should be cavitation free, provide the required head and flow rate to the system with desired power output and high efficiency.

Shukla et al. [25] compared the experimental and CFD results of the Francis turbine with each other. In that study, results show that difference between experimental and CFD results are negligible. Many researchers claimed that the source of the differences comes from the calibration mistakes and meshing problems.

According to Sanjay Jain et al. [26], numerical simulations using pressure inlet and pressure outlet boundary conditions were not converged. When they started to use mass flow inlet, total pressure outlet boundary conditions, solution was robust. According to their results, these boundary conditions are more suitable for the CFD analysis of Francis Turbine than the other boundary conditions.

Zhifang Yao et al. [27] found that by reducing the flow velocity at the runner outlet, the runner outlet diameter can be increased. This helps improve performance of the turbine. Blade profiles should be arranged cautiously to avoid von-Karman vortices [69]. CFD method can help find optimum one.

Hyen-Jun Choi et al. [28] presented that CFD approaches can aid to understand the current situation of a Francis turbine. Several different designs can be investigated by using CFD methods, and the best design can be manufactured for model testing. For their 500 kW Francis turbine, CFD results of the final design and model test results was approximately the same. It was shown that, CFD approach can be used

for design of a Francis turbine, and it has a cost and time-effective system, while improving the turbine performance.

In order to investigate the operating range of a turbine, steady-state CFD analysis is performed. In line with the steady state results, the hill chart of the turbine is obtained. On the other hand, turbines do not work on the same steady conditions all the time, transient flow characteristics are frequently observed such as startup conditions. During this time, the flow inside the turbine is unstable. To observe the effect of this instability, transient CFD analysis should be performed. J Nicolle et al [29] simulated of a Francis turbine about 40 seconds during startup condition. The main flow physics are observed.

Every single turbine is custom designed specifically to meet the requirements of each hydroelectric power plant. Generally, turbine components design is performed with utilizing CFD techniques in the today's technology. However, IEC standards advise model tests to ensure performance and accuracy instead of numerical studies. Providing geometric and kinematic similarity laws model turbines are tested and validated [30,31].

1.2.1 Cavitation

Turbines can operate out of the optimum design conditions due to seasonal fluctuation and variable electricity demand. Therefore, designer should try to make the turbine cavitation-free in a wide operation range. Cavitation, which is also called cold boiling, is the most harmful phenomena for Francis turbines. It can cause instability, pressure fluctuations, torque fluctuations, vibration, even it can break blades [32][43].

Cavitation can be observed in different types and location in the turbine. Flow separations, sudden fall in local pressure and submergence can cause the cavitation. Therefore, the reason of the problem may be due to design or operation. Avellan [33], has defined 4 different types of cavitation which are leading edge, traveling bubbles, draft tube swirl and inter-blade vortex [32]. In Figure 1.1, main types and locations for cavitation are shown in figure, comprehensive investigation is given in chapter 3.4.2.

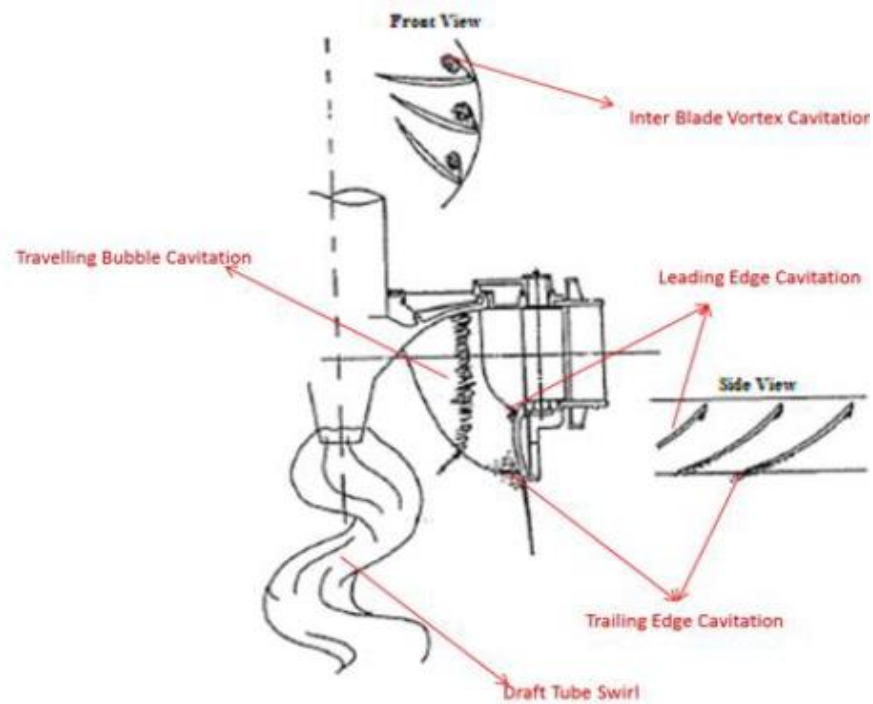


Figure 1.1 : Cavitation formation regions [adapted from 32]

Many experimental studies are available in literature about destructive effect of the cavitation. Researches states that most dangerous type is the leading-edge cavitation. It occurs at the inlet of the runner and continues through the flow path. Due to the pressure drop along the blade, it gets bigger time by time and it causes damaging all over the blade surface [64].

Escaler et al, has discovered a way to detect cavitation inside the turbine. The cavitation by nature, is unsteady and cause structural vibration. By following the pressure fluctuations, it can be perceivable and detectible. Moreover, this phenomena occur in just few milliseconds. High frequency content in the data, which is taken from the pressure sensors, leaves a mark from the cavitation [35][78]. This is the main methodology in order to detect cavitation and vortices. Pressures sensors or microphones can be used during the test. Also, guide vane passing frequency, stay vanes passing frequency and runner passing frequency can be observed in the results. These are the expected frequencies that should be seen in the results. Flow inside the turbine is unsteady because of the runner movement [36].

Moreover, CFD is the other valid way to detect cavitation and vortices in the turbine. Using numerical methods, unsteady behavior in the flow can be observed. It located monitoring points in the flow, fluctuating pressure data is saved. This data is so

complicated that hard to resolve and understand. FFT is used for the processing that signal so components of the signal can be interpreted. [37,38]

Thoma number is the dimensionless cavitation number and it represent vaporization tendency of the fluid. Celebioglu et al [38] calculated this number and showed this tendency in colorful contour on every point of the blade surface. Thoma number has also effects on the draft tube vortex. Wack [39] states that low Thoma level can cause bigger vortex rope in the draft tube.

If the local pressure is under the boiling pressure of the water, starts to vaporize. But cavitation is not the vaporization. After the vaporization, water particles turn back to the fluid phase again due to the pressure increase. In this case, due to the sudden change in the water volume, enormous forces expose [40].

Li has studied vortices which can occur in runner, guide vanes, and stay vanes. This can also cause cavitation if its local pressure at the core is under the boiling pressure of the water. Most of time this type of cavitation occurs due to the design-driven problems. On the other hand, vortices by nature, has a circular pattern and high-speed circumferential velocity. If it touches blades or other solid body inside the turbine, it can erode the solids and cause vibration all of the turbine [41-44].

Another different phenomenon is draft tube vortex, that occur inside the draft tube. Actually, it is observed all of the Francis turbines due to flow characteristics at the outlet of the runner. At the outlet of the runner, flow velocity has 2 components which are circumferential and axial. Due to circumferential velocity, flow continue to turn inside the draft tube cone. This is most important phenomena because many research states that recovery factor of the draft tube depends on this vortex's magnitude. Also, this is the main reason of the vibration in the turbine and even plant. Moreover, draft tube performance has indirect effects on the runner performance as well as general efficiency of the turbine [45,46].

At the part load conditions the draft tube vortex can cause cavitation in the draft tube. Also, vortex induced vibration has harmful effects on the bearings and others mechanical component. It decreases useful life time of them [46,47,48].

Turbine components overcomes 2 different load types which are stationary and dynamic. Mostly, reason of the failure is not the stationary loads. The source of the dynamic loads is pressure fluctuations caused by the rotor stator interaction, cavitation, vortices. Luna and Ramirez conducted a research about the fatigue crack

on the runner. They state that high level vibration due to the von-Karman vortices, produced high cycle fatigue failure on runner [49,50,51].

Many researchers have studied to the increase draft tube performance due to its importance. Javadi et al, has developed an injection system that injecting pressurized water in the draft tube. This is the passive method which means that there is no extra energy required. Pressurized water is taken from the spiral case and transferred to the draft tube. In this respect of this method, there are many applications in the plants [51-55].

Mostly water jet method has been tried in order to prevent cavitation at the draft tube cone. But this is the not only problem that can be seen at the draft tube. Therefore, Q S Wei and Van Thanh Tien has studied on J-groves which is placed at the draft tube cone. The Purpose of this modification to avoid exceed circumferential velocity in the draft tube which cause vibration [56].

1.2.2 Reverse Engineering

The components of the turbine must be mathematically modelled in order to fully understand water flow inside the turbine according to the rehabilitation motivation. Mostly this is not process that is easy to overcome. There are 2 reasons that makes this procedure difficult, the plants which required rehabilitation are old and drawings are not available. Secondly, manufacturers of the turbine are not eager to share know-how of the turbine. The method to handle such a case is called reverse engineering (RE).

Chen and Lin [58] utilized RE methodology and generated gas turbine blades. Garcia also followed same methodology to model of the Francis blade [57]. Celebioglu and Kaplan [59], have used this methodology and generated Francis type blade model from the point cloud obtained by 3D scanner. The RE blade and existing blade CFD results are consistent with each other.

There are 3 steps to carry on the reverse engineering methodology. Scanning, management of the data and generation 3D CAD model. This process can be different depending on the case of the geometry.

This methodology has many benefits. Firstly, the presence of the fully defined mathematical blade model provides more accurate mesh structure. Secondly, by

utilizing this methodology, data takes much less memory, so 3D modelling, meshing and simulations takes less time. It makes the processes faster.

In this study, runner of the turbine model is generated by using point cloud which is taken inside the turbine. Also guide vane, stay vanes are scanned by using 3D robotic arm and same methodology followed as runner. Therefore, most effective geometries could be modelled same as the plant. Draft tube and spiral case modellings have been carried on by using manufacturer drawings.

1.3 CONTRIBUTION TO LITERATURE

To the best of author knowledge, it is the first study in the literature that used model & prototype similarity laws for the existing & the scanned turbine, which is defined in the IEC 60193.

The critical decision for rehabilitation of an old turbine, can be taken with the methodologies presented in this study. The steps that determine this decision to take are defined step by step.

CHAPTER 2

DEFINITION OF THE PROBLEM AND THEORETICAL BACKGROUND

2.1 DEFINITION OF THE PROBLEM

Gezende Hydro Electric Power Plant is located at Mut which is the district of Mersin. The generating units at Gezende HPP (1994) are originally installed with three identical vertical Francis turbines. Each turbine is directly connected to synchronous generators with a nominal capacity of 54.2 at nominal flow of 38.6 m³/s and nominal net head of 154.0 m. The Gezende Hydro Electric Power Plant is located on Ermenek River as shown in Figure 2.1. The main characteristics of Gezende HPP are given in Table 2-1.

Table 2-1: Gezende HPP Characteristics

Type	Vertical Francis
Power	54.2 (MW)
Net HEAD	154 (m)
Flow Rate	38.6 (m ³ /s)
Speed	333.3 rpm



Figure 2.1: Gezende HPP Site View

Gezende HPP has 12 stay vanes, 20 guide vanes, and 13 runner blades, which generates 54.2 MW of power with 154 m net head and 38.6 m³/s flow rate. A comprehensive investigation regarding the hydraulic performance of the power plant with Computational Fluid Dynamics (CFD) techniques are performed. Reverse engineering methodology is utilized for extraction of the blade's geometry. The model of the spiral case and draft tube components are obtained by examination of technical drawings. Therefore, 2 distinct methodology are used for the modelling geometries and simulations.

2.2 THEORETICAL BACKGROUND

2.2.1 Coordinate System

The coordinate system which is used in the simulations is shown in the CAD model of the Gezende HPP in Figure 2.2. Z-axis is defined at the center of the turbine runner, according to the right-hand rule. X-axis is defined parallel to the spiral case inlet direction and draft tube and y- axis is defined perpendicular to the rotational axis.

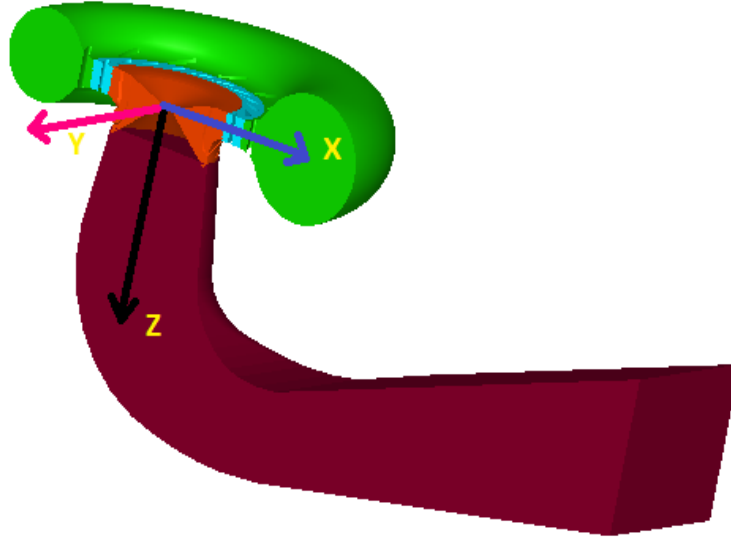


Figure 2.2 : Coordinate System

2.2.2 Turbine Efficiency

According to the IEC 60193 standard, hydraulic energy at the various points is defined as it is given in Eq (2.1) [31].

$$gH_1 = \frac{P_1}{\rho} + \frac{V_1^2}{2} + gz_1 = \frac{P_1}{\rho} + \frac{Q^2}{2A_1^2} + gz_1 \quad (2.1)$$

Where z_1 is the tailwater level. By using the hydraulic energy definition, specific energy at the turbine inlet and outlet can be calculated as it is given below.

$$E = gH_1 - gH_2 \quad (2.2)$$

Turbine hydraulic power is calculated using Equation (2.3).

$$P_h = \rho QE \quad (2.3)$$

Some of the flow is lost due to the leakage through the space between the turbine runner and stationary parts. The turbine flow rate, Q_t , is calculated considering the leakage loss that occurs in the turbine runner as it is given in Eq (2.4).

$$Q_t = Q\eta_q \quad (2.4)$$

In the Eq (2.4), η_q , is the volumetric flowrate. The specific energy that is transferred to the turbine is calculated using Eq. (2.5).

$$E_t = E\eta_e \quad (2.5)$$

The mechanical power that is transmitted to the turbine shaft is defined in Eq (2.6).

$$P_t = \rho Q_t E_t = T_m \omega \quad (2.6)$$

Where ω , is the turbine angular velocity and T_m is the torque value transmitted from runner to shaft. The turbine hydraulic efficiency is calculated using Eq (2.7) as it is given below.

$$\eta_h = \frac{P_t}{P_h} = \frac{\rho Q_t E_t}{\rho Q E} = \eta_q \eta_e \quad (2.7)$$

The opening in the geometrical model is not considered in the CFD studies, due to this simplification the leakage related losses in Eq (2.4) is disregarded. Therefore, $Q_t = Q$ and $\eta_q = 1$ in the CFD simulations. Zero leakage loss assumption is made generally in the Francis type turbine CFD studies. Maruzewski [60], compare the zero-leakage loss assumption numerical studies with experimental studies and revealed that these assumptions do not change the reliability of the CFD studies.

2.2.3 Spiral Case and Guide Vane Efficiency

Total pressure loss is calculated by equation 2.8

$$P_{loss} = P_{inlet} - P_{outlet} \quad (2.8)$$

Component efficiency can be calculated based on total pressure loss between inlet to outlet.

$$\eta_{component} = \frac{P_{inlet} - P_{loss}}{P_{inlet}} \quad (2.9)$$

2.2.4 Flow Kinematics for Francis Turbine

With the interaction between the runner blades and the flowing fluid, the hydraulic energy of the liquid is converted to the mechanical shaft energy in the turbine runner. This energy conversion is the result of the two main motions in the runner which are known as relative and transportation motion. The sum of the relative and transportation motion is known as absolute motion as shown in Eq (2.10). In this equation v , u and w denote absolute velocity, relative velocity, and transportation velocity, respectively.

$$v = u + w \quad (2.10)$$

These velocity components are stated with velocity triangles. To obtain the velocity triangles; flow is assumed as irrotational, inviscid, and composed of the infinite

number of runner blades. As each turbine has its head and flow rate value, turbine geometries are specific for itself. Therefore, all turbines have their designing process. To make generalization which is applicable for all of the Francis turbine runners velocity triangles are defined which are shown in Figure 2.3.

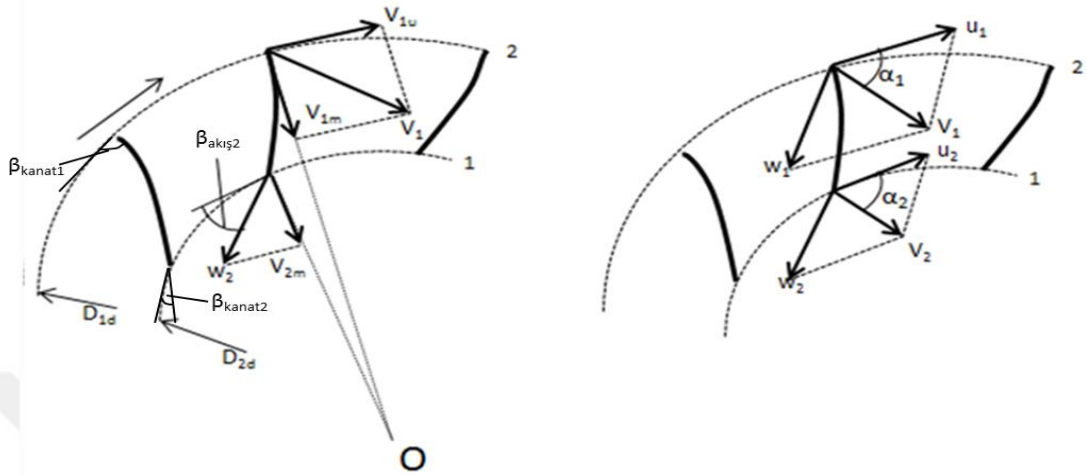


Figure 2.3:Velocity Triangles for Radial Flow Turbine Runner [adopted from 20]

The turbine operating conditions are defined with the two parameters, which are flow rate (Q) and rotational speed (n) of the runner. When the geometrical parameters of the runner are known, it is possible to calculate the velocity component values. Meridional component, v_m is found with the relation given above with using the continuity equation.

$$V_m = \frac{Q}{F_i} \quad (2.11)$$

Where F_i is the flow area in the runner. By inserting the flow are in the equation (2.11), equation (2.12) can be obtained.

$$v_m = \frac{Q}{\pi D_1 b_0} \quad (2.12)$$

Where b_0 is the height of the inlet opening of the runner. The circulation that is generated in the wicket gate is conserved to the runner inlet. Then, the mathematical definition of this situation which is shown in Eq (2.13), the peripheral velocity component, v_{1u} , can be calculated.

$$v_{1u} = v_{0u} \frac{D_{02}}{D_{1d}} \quad (2.13)$$

The absolute velocity at the runner inlet can be defined by the vector sum of the two components:

$$v_i = \sqrt{v_{im}^2 + v_{iu}^2} \quad (2.14)$$

The transportation velocity is calculated with Eq (2.15):

$$u = \frac{\pi D n}{60} \quad (2.15)$$

To determine the w_1 velocity component, geometrical formulations and velocity triangles are used together (Figure 3). At the turbine outlet, Eq (2.14) and Eq (2.10) is valid. With the assumption of $\beta_{2\text{flow}} = \beta_{2\text{blade}}$, w component will be calculated as it is given in Eq (2.16).

$$w_2 = \frac{v_{2m}}{\sin \delta_2} \quad (2.16)$$

2.2.5 Turbine Energy Equation

The torque on the shaft is equal to the change in the angular momentum of the water flow. Eq. (2.17) is obtained by using the angular momentum equation for the inlet to the outlet of the runner. The sum of the moments of external forces about the axis of rotation is as follows:

$$\rho Q (v_2 \cos \alpha_2 r_2 - v_1 \cos \alpha_1 r_1) = \sum M_0 \quad (2.17)$$

Figure 2.4 presents the velocities at the leading and trailing edges of the runner blades. Torque is only generated when runner blades generate circulation in the runner. The generated power can be calculated using the moment equation and angular velocity of the runner:

$$P = M\omega = \rho g H Q \eta \quad (2.18)$$

Where H is the head of the turbine, and η is the hydraulic efficiency. The main energy equation of turbines (Euler equation) is obtained substituting for M in Eq. (2.18):

$$H\eta = \frac{1}{g} (u_1 v_1 \cos \alpha_1 - u_2 v_2 \cos \alpha_2) \quad (2.19)$$

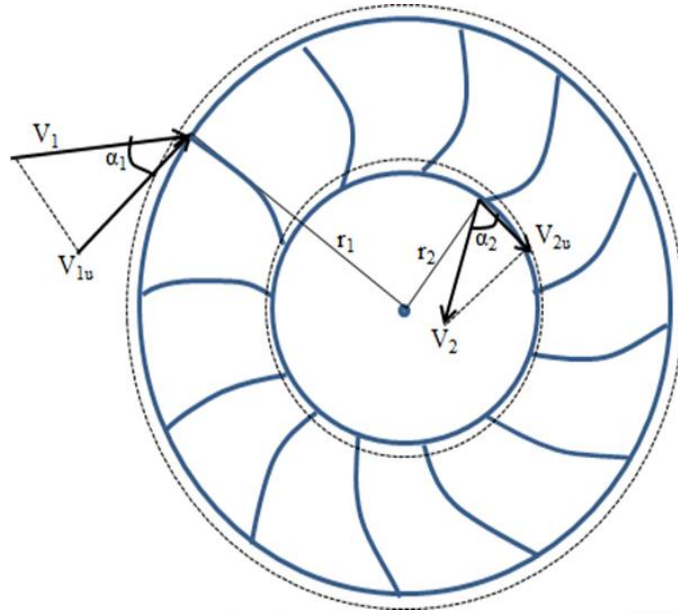


Figure 2.4: Velocities at the Edge of the Runner Blade [adopted from 20]

Eq. (2.20) can be written as follows using the expressions for circulation:

$$H\eta = \frac{\omega}{2\pi g} (\Gamma_1 - \Gamma_2) \quad (2.20)$$

Hydraulic energy is related to the mechanical energy which is absorbed by the runner as shown in Eq. (2.21). The angles at which water enters and exits the runner are also important parameters that affect hydraulic performance. The position of the guide vane determines the angle of the water inlet of the runner; therefore, the guide vane angle is a major parameter as well. Changing the guide vane angle changes the efficiency.

2.2.6 Pressure Recovery Factor

Draft tube transforms kinetic energy of the water at the runner outlet into pressure. Pressure recovery factor is a measurement of achievement of the draft tube [18]. It is calculated by equation 2. 22.

$$C_p = \frac{P_{out} - P_{in}}{\frac{1}{2}\rho V_{in}^2} \quad (2.22)$$

Where,

P_{out} = Static pressure at the draft tube outlet

P_{in} = Static Pressure at the draft tube inlet

V_{in} = Velocity magnitude at the draft tube inlet

CHAPTER 3

METHODOLOGY

3.1 REVERSE ENGINEERING METHODOLOGY

Francis type turbines have five main components, which are the spiral case, stay vane, guide vane, runner, and draft tube. For Gezende HPP, spiral case, and draft tube assembly drawings are provided by the manufacturer company. On the other hand, for stay vane, runner, and guide vane reverse engineering procedure is needed. The most important part of reverse engineering (RE) process for turbine blades is obtaining analyzable blade geometry from the solid model and determining the blade design parameters. The basic RE process is shown in Figure 3.1. Laser scanning technology, which has superior abilities like capturing sweeping curves and lofted surfaces are used firstly to obtain point cloud, and the CAD model is created with using the point cloud. After obtaining to CAD model for gaining the flow zone of the blades and make CAD model analyzable with CFD tools, meridional profile, blade angles, and blade thickness are determined. Those vital design parameters are transferred to the ANSYS Blade-Gen module from SolidWorks software. In the last part, the scanned part is validated with the existing part. In the IEC 60193 standard, permissible deviations in the geometrical similarity between model and prototype turbine are described [31]. In this study, the given similarity deviations for model and prototype is applied for the existing and scanned turbine. By this way, it is ensured that the scanned turbine runner is in the range of the similarity tolerances. In addition to this, scanned and reverse engineered blades are simulated to be ensure that they are similar.

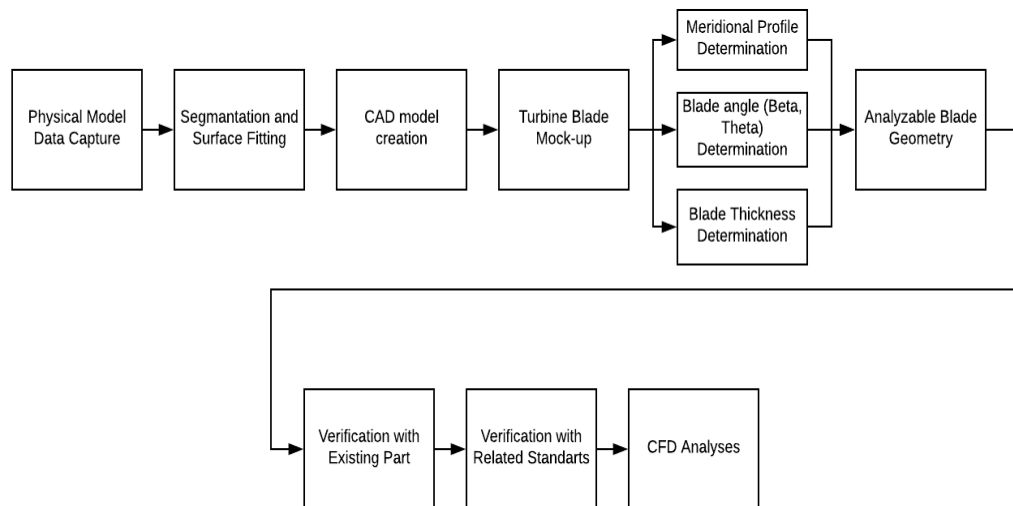


Figure 3.1: Flow chart of the Reverse Engineering Process

3.1.1 3D Digitalization

3D laser scanning technology is ideal for 3-dimensional modeling and visualization with rapid data collection ability. To determine the locations of the points in space, this technique uses the Delaunay Triangulation method [61]. A Portable Laser Scanner Romer Absolute Arm [62] is used for scanning work. This step is one of the key step in the RE process as it directly effects the quality of the model construction. GeoMagic design X Software is utilized in order to process data which comes from the scanning arm. The position of the scanner is adjusted to allow the device to reach all wetted surfaces. If this is not possible, point clouds from different scanner locations are merged by using reference blocks located in selected positions, as shown in Figure 3. 2. In Figure 3.3, the scanning process is shown. For runner scanning laser scanner is located in three different locations for guide vane and stay vane one location point is used to obtain the model.



Figure 3.2 :Reference Blocks



Figure 3.3 : Scanning of the turbine runner

3.1.2 CAD Model Creation

Using the point cloud that comes from digitalization, CAD models of the turbine runner, guide vane, and spiral case are generated. Scanning is performed only one blade model; therefore, solid model of the one blade is obtained from cloud data. The blade profile is reflected to form the CAD model of the whole blades. For guide vane, digitalization, and CAD model creation steps are shown in Figure 3.4.

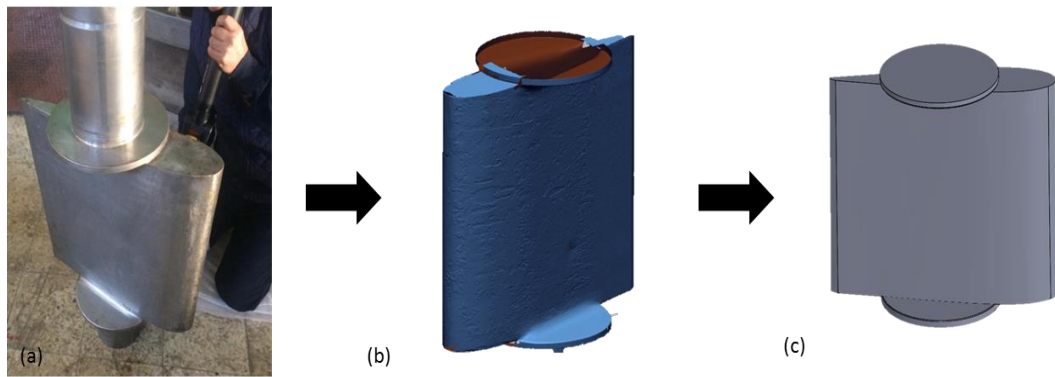


Figure 3.4: (a) Scanning (b) Point cloud (c) Solid model of the guide vane

3.1.3 Determination of Blade Design Parameters

Firstly, the meridional profile of the blade geometry is obtained by getting a projection of the runner blade profile to the radial plane. The meridional profile comprises the leading edge, trailing edge, hub, and shroud curves which are necessary to generate fluid flow zone in Bladegen module. In the Bladegen module, span curves are defined between the hub and shroud, which will help to define blade angles through leading edge to trailing edge. The span curves are reflected the runner geometry to define the sections which will determine the blade angles. In Figure 3.5, the meridional profile of the runner blade is shown with the defined span curves.

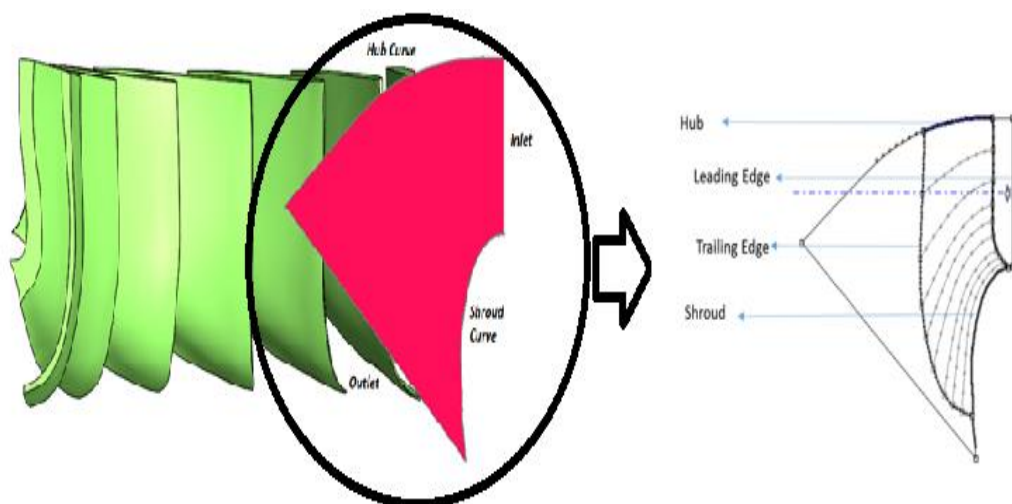


Figure 3.5: Meridional profile of the runner blade

After obtaining the meridional profile, two important angles which define the runner geometry should be obtained for the hub, shroud, and all span curves through the

leading edge to the trailing edge of the blade. The metal angle, known as the beta angle (β), is the angle between the camber of the blade and the tangent of the circle that is drawn from the center of the runner [63]. The wrap angle, known as the theta angle (θ), is the position angle in the cylindrical coordinate system. In Figure 3.6, the camber line of the blade and beta, theta angles are shown.

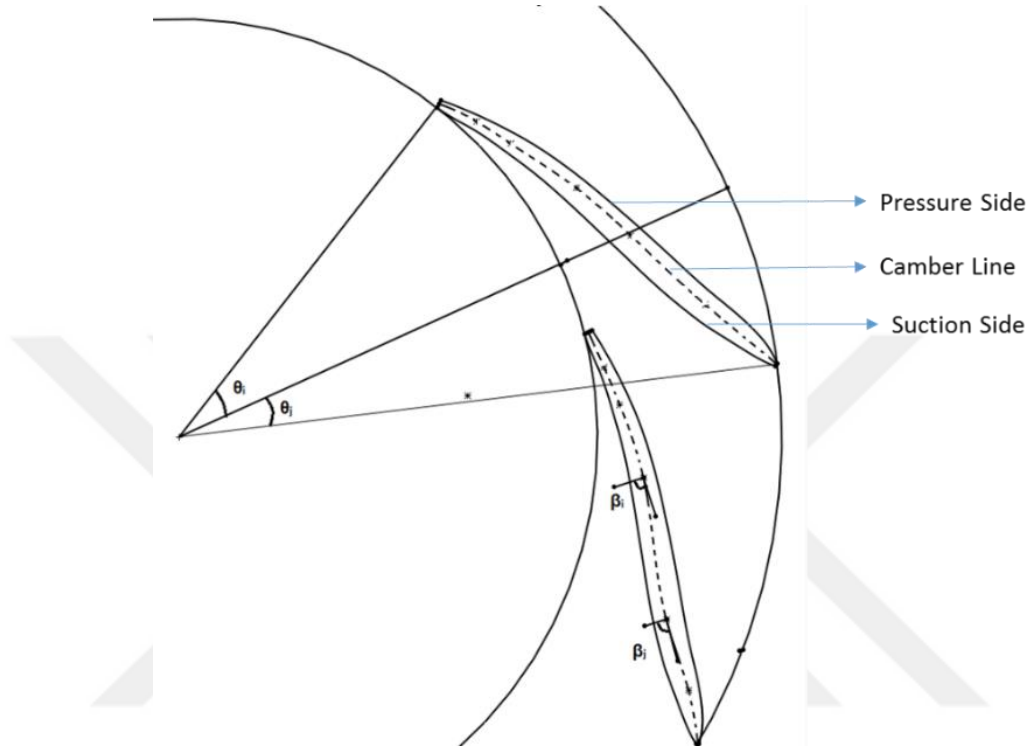


Figure 3.6: View of the flow angles in the camber line

To determine the blade angles, firstly length of the camber line should be calculated. The positions of the points on the camber line are determined with averaging the corresponding points located at pressure and suction sides of the blade using the equations (3.1) -(3.5).

$$x_i^{cc} = \frac{x_i^{ps} - x_i^{ss}}{2} \quad (3.1)$$

$$y_i^{cc} = \frac{y_i^{ps} - y_i^{ss}}{2} \quad (3.2)$$

$$z_i^{cc} = \frac{z_i^{ps} - z_i^{ss}}{2} \quad (3.3)$$

$$CC_i = \sqrt{(x_i^{cc})^2 + (y_i^{cc})^2 + (z_i^{cc})^2} \quad (3.4)$$

$$R_i^{cc} = \sqrt{(x_i^{cc})^2 + (y_i^{cc})^2} \quad (3.5)$$

Where PS, SS, CC, R denotes pressure side, suction side, camber line and radius of the camber line in point i, respectively. Theta angles are calculated using the Eq (3.6).

$$\theta_i = \tan^{-1} \left(\frac{y_i}{x_i} \right) \quad (3.6)$$

To calculate beta angles, conformal mapping triangle is used [49]. In this method form of the blade is drawn in the perpendicular plane, which is a transformation link between two planes, as shown in Figure 7. For all of the span curves, leading edge (A_0) defines the absolute zero point. To calculate the distance between the points on the camber curve, Eq (3.7) is used, which is a function of theta angle.

$$\Delta A_i = \Delta \theta_i \times \left(\frac{R_i + R_{i+1}}{2} \right) \quad (3.7)$$

Inlet and outlet beta angles are shown on the conformal mapping triangle. To calculate the beta angle at any point, geometrical derivations are used (Eq 3.8-3.10). Inlet beta angle is calculated at absolute zero points, and outlet beta angle is calculated at meridional length.

$$\tan \beta_1 = \frac{dA(x)}{dx} \quad (3.8)$$

$$\tan \beta_2 = \frac{dA(x)}{dx} \quad (3.9)$$

$$\tan \beta_i = \frac{dx_i}{dA_i} \quad (3.10)$$

To calculate the blade thickness, the distance between the pressure side and suction side is calculated for each point of the blade. Blade thickness calculation equation is given below.

$$\Delta T = \sqrt{((x_i)^2 + (y_i)^2 + (z_i)^2)_{ps}} - \sqrt{((x_i)^2 + (y_i)^2 + (z_i)^2)_{ss}} \quad (3.11)$$

3.2 NUMERICAL METHODOLOGY

In this study, a comprehensive investigation regarding the hydraulic performance of the power plant with Computational Fluid Dynamics (CFD) is utilized. Ansys CFX

Turbo-mode is used in the analysis. The computational domain consists of the Spiral casing with stay vanes, the guide vane cascade, the runner, and the draft tube. For constructing the geometry for the spiral case and draft tube SolidWorks software is used. For a runner, stay vane and guide vane geometries, Blade-Gen software also used. The finite element method (FVM) is used to reduce the governing partial differential equations to a set of algebraic equations that solves the incompressible pressure-based Reynolds Averaged Navier-Stokes (RANS) equations is employed.

High order upwind and second-order centered schemes are used for the convection and diffusion terms, respectively. Euler scheme is selected for the time dependent term in the governing equations. k- ϵ is used as a turbulence model to solve Reynolds Averaged Navier-Stokes (RANS) equations. It resolves flow separations accurately near the walls. The convergence level is set to 1×10^{-5} .

To model, the interaction of the parts with each other Multi-frame reference model (MFR) is used [79] Between the interface of runner/ guide vane and runner/draft tube, frozen rotor interface is selected. For runner and guide vane as an inlet condition pressure inlet and as an outlet condition mass flow outlet is used. In the full turbine analysis mass flow inlet in the spiral case inlet and in the draft tube outlet pressure outlet is applied. The other remaining parts are assumed as no-slip wall condition.

Figure 3.7 shows the total machine configuration, which is ready for CFD analysis and mesh structures for all the components. Flow diagram for the CFD study given in Figure 3.8.

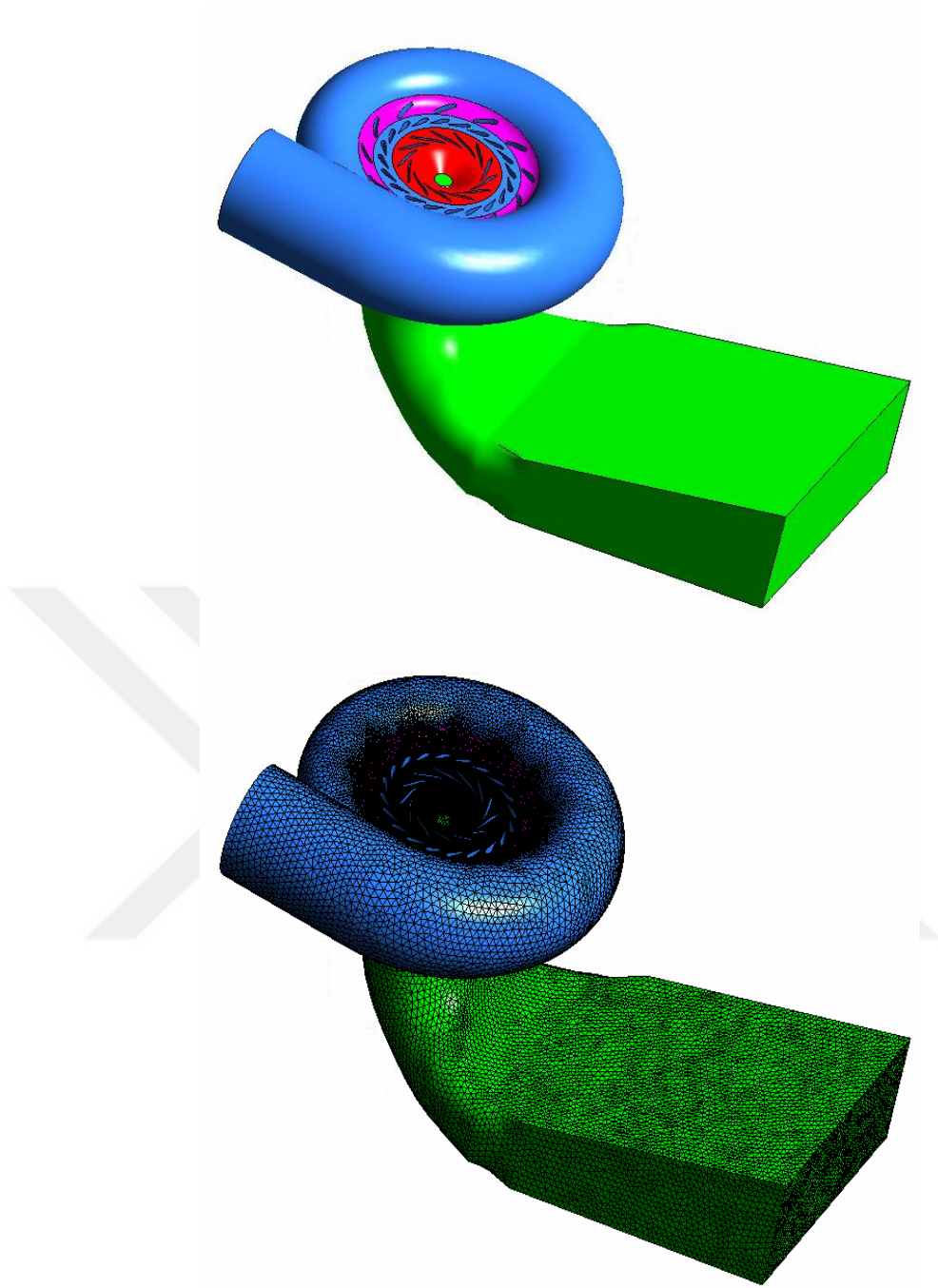


Figure 3.7: (a) Machine Gezende (b) Mesh Structure

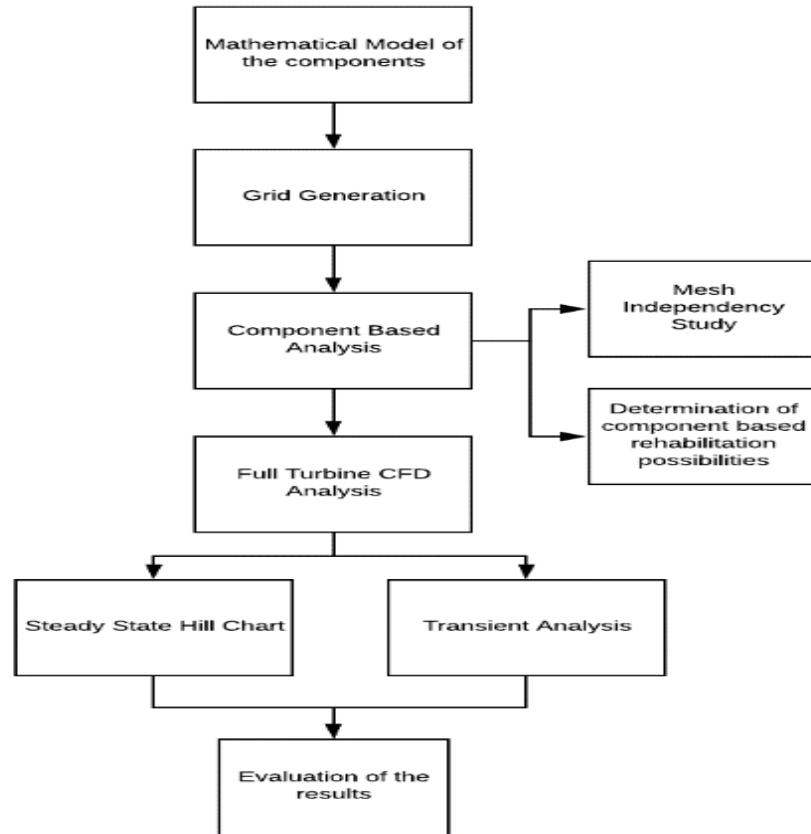


Figure 3.8: CFD Methodology

3.2.1 Governing Equations

Continuity and momentum equation are given below for laminar, Incompressible, 3D, single phase, immiscible and viscous flow.

$$\frac{\partial \rho}{\partial t} + \frac{\partial(\rho u_i)}{\partial x_i} = 0 \quad (3.12)$$

$$\frac{D(u_i)}{Dt} = \frac{\partial u_i}{\partial t} + u_j \frac{\partial u_i}{\partial x_j} = -\frac{1}{\rho} \frac{\partial P}{\partial x_i} + \mu \frac{\partial^2 u_i}{\partial x_j^2} + F_i \quad (3.13)$$

There are 4 equations for 4 different unknowns which are u, v, w and p term. However, these equations cannot be solved analytically due to non-linear and second order differential terms in the momentum equation.

Besides, laminar assumption is not realistic approach for turbine flow applications. Flow is turbulent which means that there are time dependent changes in characteristics of all components such as velocity, pressure, stresses, and temperature etc. Due to the extremely complex nature of turbulence and its incomplete understanding there is not a single accepted definition of turbulence.

Leonardo da Vinci was so intrigued by turbulence that he depicted it in one of his sketches given in Figure 3.3. While observing the flow of water, he gave one of the very first definitions of turbulence 500 years ago and he said “.the smallest eddies are almost numberless and large things are rotated only by large eddies and not by small ones and small things are turned by small eddies and large” [66].



Figure 3.9: DaVinci Turbulent flow sketch

After him, many researchers and engineers put forward different definitions to depict and understand turbulent flow [67-71]

Due to its complexity, a definition does not work properly for turbulence, instead of it, it is better to explain its characteristics. Characteristics of turbulence are,

- Irregularity
- Diffusivity
- Dissipation
- Large Reynolds numbers
- 3-D vorticity fluctuations
- Feature of a flow, not fluid

There are two different approach to express velocity with fluctuation component. Reynolds Averaged Navier Stokes approaches decompose velocity into 2 parts

which are fluctuations and averaged velocity. According to this approach the velocity terms are replaced in the governing equations by given expression.

$$u_i = \bar{u}_i + u_i' \quad (3.14)$$

Therefore, RANS equations are obtained.

$$\frac{\partial \rho}{\partial t} + \frac{\partial \bar{u}_i}{\partial x_i} = 0 \quad (3.15)$$

$$\frac{\partial \bar{u}_i}{\partial t} + \bar{u}_j \frac{\partial \bar{u}_i}{\partial x_j} = f_i - \frac{1}{\rho} \frac{\partial P}{\partial x_i} + \frac{\partial}{\partial x_j} \left[\mu \left(\frac{\partial \bar{u}_i}{\partial x_j} \right) - \overline{(u_i' u_j')} \right] \quad (3.16)$$

$\overline{(u_i' u_j')}$ This term in the equation 3.16 is called Reynolds-Stress and it increases number of unknowns to 10 with the addition 2 unknowns for each axis. Reynolds Stress is resolved by Bossinesq hypothesis that exhibits a relation between Reynolds Stress and velocity gradients. Therefore, governing equations becomes,

$$\frac{\partial \rho}{\partial t} + \frac{\partial \bar{u}_i}{\partial x_i} = 0 \quad (3.17)$$

$$\frac{\partial}{\partial t} (\bar{u}_i) + \bar{u}_j \frac{\partial \bar{u}_i}{\partial x_j} = -\frac{1}{\rho} \frac{\partial P}{\partial x_i} + \frac{\partial}{\partial x_j} \left[\mu' \left(\frac{\partial \bar{u}_i}{\partial x_j} + \frac{\partial \bar{u}_j}{\partial x_i} - \frac{2}{3} \delta_{ij} \frac{\partial u_k}{\partial x_k} \right) \right] \quad (3.18)$$

$$\mu' = \mu + \mu_t \quad (3.19)$$

Bossinesq hypothesis provides velocity fluctuations can be expressed by utilizing additional viscosity term which is called turbulent viscosity. Therefore, turbulent fluctuations in the velocity components modelled this additional term. For the sake of the express turbulent viscosity term different turbulence models are developed by scientists. There is no universal turbulence model so every single problem requires different model considering its limitations and capabilities. In this study, k-ε model is selected which has 2 different equations. It solves convection terms for k (turbulent kinetic energy) and ε (kinetic energy dissipation).

$$\rho \frac{\partial k}{\partial t} + \rho \frac{\partial k u_i}{\partial x_i} = \frac{\partial}{\partial x_j} \left(\frac{\mu_t}{\sigma_k} \frac{\partial k}{\partial x_j} \right) + 2\mu_t E_{ij} E_{ij} - \rho \varepsilon \quad (3.20)$$

$$\rho \frac{\partial \varepsilon}{\partial t} + \rho \frac{\partial \varepsilon u_i}{\partial x_i} = \frac{\partial}{\partial x_j} \left(\frac{\mu_t}{\sigma_\varepsilon} \frac{\partial \varepsilon}{\partial x_j} \right) + C_{1\varepsilon} \frac{\varepsilon}{k} 2\mu_t E_{ij} E_{ij} - C_{2\varepsilon} \rho \frac{\varepsilon^2}{k} \quad (3.21)$$

where S_{ij} is deformation term, δ_{ij} is Kronecker and ζ is secondary vorticity term which can be written as $\zeta = -\frac{2}{3}\mu$. By solving continuity and momentum together, velocity, pressure and density values in the flow field are calculated. The fluid mechanics problems which have initial and boundary conditions are solved with CFD techniques as they cannot be solved analytically.

3.2.2 Advection Schemes

Finite volume method is used for the discretization of the flow region. The flow region is subdivided into small control volumes in which the mass and momentum are conserved. In order to reach solution of the given domain, governing equations are realized hence numerical solution is provided for every grid point at the volume. As a result of discretization, algebraic equations are obtained for entire domain.

Upwind and high resolution are different available approaches using while interpolating velocity flux from grid points to the face center of each cell. High resolution scheme benefits from the Taylor expansion and so it provides more accurate results. On the other hand, upwind scheme takes much less computational time. In this study, upwind scheme is used in pre-design process. For final solution, high resolution scheme is utilized.

Different advection scheme options are used throughout the simulations namely upwind, high order upwind and high resolution. Faster simulations for the determination of the overall geometry of components are performed using coarser mesh. For the runner, to reduce the design time span, initial simulations are performed with a coarse mesh and Upwind scheme in the k- ϵ turbulence model. A high-resolution advection scheme is selected for fine mesh cases.

3.2.3 Boundary Conditions

In the CFD problems, choosing the appropriate boundary conditions is one of the most important subjects to obtain accurate results. In the component-based analysis, for the runner, guide vane, stay vane, and draft tube pressure inlet & mass flow outlet is utilized as inlet and outlet boundary condition, respectively. For spiral cases, mass flow inlet and pressure outlet are used as inlet and outlet boundary conditions, respectively. The other walls are considered as the no-slip boundary condition for all the components. For the full turbine analysis pressure, inlet boundary condition in the spiral case inlet and the draft tube outlet mass flow outlet is utilized. For hill chart analysis for both inlet and outlet pressure are used in this way, the flow rate is calculated in different guide vane openings.

3.2.3.1 Mass Flow Rate Boundary Condition

The mass flow rate provides a uniform flow rate when it is given perpendicular to the flow area. If the flow direction is given in cylindrical or spherical coordinates with the given angle flow is uniformly distributed through the area. The mass flow rate is measured as it is given in Eq (3.22).

$$\rho U = \frac{\dot{m}}{\int dA} \quad (3.22)$$

dA denotes control volumes and this term is related to the generated mesh. In the blade geometries for the determined water inlet angle flow rate is given to the software by this wat flow inlet angle is controlled.

3.2.4 Static Pressure Boundary Condition

Using Equation 3.23, static pressure is calculated at the outlet of the draft tube.

$$P = \rho g H_{tail} + P_{atm} \quad (3.23)$$

H_{tail} represents depth of the tail water.

3.2.4.1 Total Pressure Boundary Condition

Using Equation 3.24 the total pressure is calculated for each component. Regarding the losses for each component, the head is calculated, and inlet total pressure is calculated for all of the components.

$$P = \rho g H + P_{atm} \quad (3.24)$$

3.2.4.2 Wall Boundary Condition

For all components, except inlet and outlet wall boundary condition is utilized. The fluid has zero velocity relative to the boundary. The fluid velocity at all fluid–solid boundaries is equal to that of the solid boundary.

3.3 SIMULATION STRATEGY

For the original turbine configuration of Gezende HPP with using the mathematical models, which are obtained with reverse engineering, firstly all components are analyzed separately, and then full turbine analysis are conducted. Analyses are carried out at different flow rate and head values to observe the behavior of the

turbine at various operating conditions. Analyses at off-design points help to examine the performance of the turbine for instance at the partial load conditions.

In this study, CFD simulations was conducted for both steady and transient cases. All the simulations executed via a super-computer cluster in TOBB ETU – HYDRO. While steady state simulations took time almost 5 hours, transient case takes 5 days for each.

Steady state simulation carried on different operation conditions which are 134m, 144 m, 154 m, 164 and 174m. For all single head, analyses have been repeated for distinct guide vane openings at which 19°, 21°, 23°, 25°, 27°, 29°, 31°,33°. After these simulations, with the calculation of efficiency, hill chart was drawn.

Results of the steady state simulation verified, by efficiency values which are taken from the power plant and manufacturer of the turbine. Transient simulations have been conducted only 5 different operation point due to the required computational time.

3.4 Post Process Methods and Tools

Geomagic Design X, SolidWorks and ANSYS Blade Gen software has been utilized in the reverse engineering part of the thesis. ANSYS CFX modules has been used for the numerical study. For unsteady solution of turbine, all of the pressure signals have been processed via Matlab codes that specially written during this study.

3.4.1 Cavitation, Cavitation Types and Thoma Number

Cavitation is a physical phenomenon that defines bubbles in a fluid flow. According to the Bernoulli principle, when the velocity of the fluid increases, the reduction of pressure occurs. And the lower pressure means lower boiling point. In other words, the reduction of the pressure decreases the boiling point of the fluid till to the ambient temperature. In this situation, cold boiling occurs which contains vapor or gas and vapor filled bubbles. This case is known as cavitation

In other words, regions of the high flow velocity, the local pressure decreases below the vapor pressure, and vapor bubbles start to occur in the flow. According to Knapp et al. [70]'s definition when a body is heated under constant pressure known as

boiling, given in Figure 3.10, or when it's pressure is decreased under constant temperature known as cavitation, a new state occurs which contains vapor or gas and vapor filled bubbles [70].

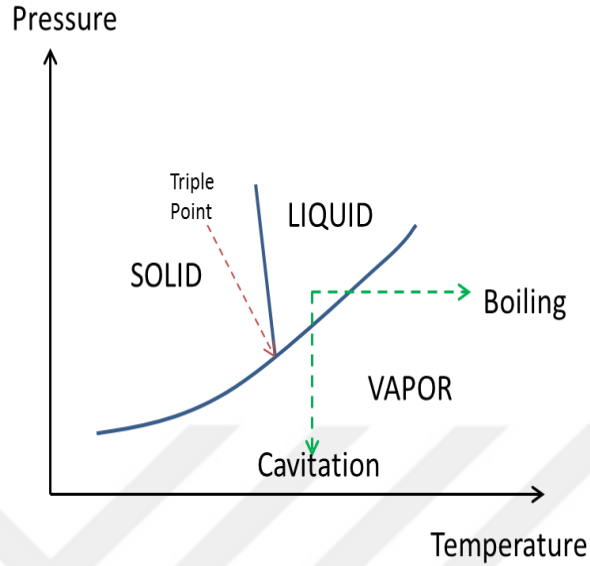


Figure 3.10: Phase Diagram for a Simple Substance

In the turbine runner, the most important component that exposed to cavitation is the runner, which has a dominant effect on power and efficiency. Therefore, cavitation phenomena are investigated in the turbine runner. Using the pressure distribution through the runner blades Thoma number distribution is obtained for the turbine runner. Thoma number is the dimensionless cavitation number which is defined as it is given in Eq (3.25).

$$\left(\frac{p_i - p_v}{\rho g}\right) \times \left(\frac{1}{H_n}\right) = \sigma_p - \sigma_i \quad (3.25)$$

Allowable Thoma number for the HPP (σ_p) is calculated as it is given below

$$\sigma_p = \frac{\frac{(P_{amb} - P_v)}{\rho g} - Z_s}{H} \quad (3.26)$$

In the Eq (3.25) and (3.26)

p_i → Pressure distribution at point i

p_v → vapour pressure

H_n → Net head

σ_p → Sigma plant

Z_s → Tailwater level

σ_i → Sigma number at point i

Cavitation occurs when local pressure value is equal to the vapor pressure. This situation is defined with Thoma number as it is given in Eq (3.27).

$$\sigma_i = \sigma_p \quad (3.27)$$

Once the local sigma value exceeds the sigma plant value, cavitation bubbles begin to form and grow. Cavitation in Francis turbines is briefly described in the Li [32].

According to Li [32], the main types of cavitation which can occur in the Francis type turbines are leading edge, travelling bubble, draft tube swirl, Inter-blade vortex and trailing edge cavitation as given in Figure 3.11.

Trailing-Edge Cavitation: Operating range 3.11a symbolizes the trailing edge cavitation. In this type of cavitation, if the cavitation occurs only in the trailing edge of the blade cavities collapse in the draft tube, and no severe damage has occurred. If the cavitation region reaches the upstream of the blade, it can be dangerous.

Draft Tube Swirl Cavitation: Draft Tube swirl cavitation is the most common phenomenon of the Francis turbine. This type of cavitation occurs in the outlet of the runner and the inlet of the draft tube (operating range 3). Draft Tube swirl is a cavitation vortex-flow that is formed just below the runner cone in the center of the draft tube. While draft tube vortex mostly appears in the part-load condition, it is the main source of the vibration problem of the Francis turbine for the whole operation range. If natural frequency (or eigenfrequencies) of the turbine components match with that vibration frequency, hydro-acoustic resonance occurs, and it can cause very hazardous results that cannot be compensated. Cracks and fractures can appear on the runner, bearings or any other the components of the turbine and even the powerhouse. Cavitation can also develop in the low-pressure zone of the vortex core associated with the Thoma level. This type of cavitation produces pressure pulsations and power fluctuations. To prevent this type of cavitation two solution methods are recommended in Li [32]. The first one is, air admission to the upper section, and the second one is using fins in the draft tube wall. With those methods, the pressure is increased, so cavities are collapsed and disappear. Also, the vortex intensity will be reduced.

Leading Edge Cavitation: In the high head operation condition, cavitation is occurring on the suction side of the blade near the inlet edge, as is seen in Figure 3.11 (a). As it occurs in the inlet of the runner, it damages heavily, causes vibration, and provokes pressure fluctuations.

Inter-Blade Vortex Cavitation: In the operating range 4, due to the flow separation, secondary vortices are formed between the blades as it is seen in Figure 3.11 (d). If these vortices touch the blade edges, then this type of cavitation can be harmful except this situation inter-blade vortex does not cause any vibration or damage. In the high head operating range, as the vortices become unstable, it will be a harmful cavitation type.

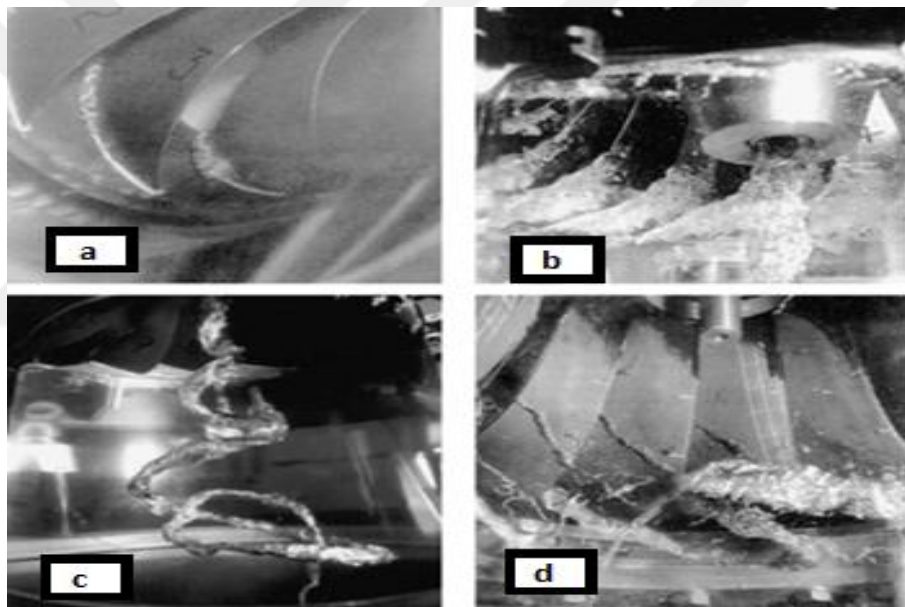


Figure 3.11: Cavitation in Francis Turbines (a)leading-edge cavitation (b) traveling edge cavitation (c) draft tube swirl cavitation (d) Inter-blade vortex cavitation [adapted from 32]

3.4.2 Fast Fourier Transform

The complicated data signal which generated by experimental or numerical study, can be decomposed to its periodic components with its frequency and magnitude by utilizing Discrete Fourier Transform. Discrete Fourier transform converts a signal from its original domain to the frequency domain. The discrete data from the original signal is calculated by eq. 3.30.

$$\Phi_k = \sum_{n=0}^{N-1} \widehat{\Phi}_n \frac{e^{2\pi i k n}}{N} \quad k=0,1,2,\dots,(N-1) \quad (3.28)$$

Where Φ_n , represents discrete coefficients it calculated by eq. 3.31.

$$\Phi_n = \frac{1}{N} \sum_{k=0}^{N-1} \widehat{\Phi}_k \frac{e^{-2\pi i k n}}{N} \quad n=0,1,2,\dots,(N-1) \quad (3.29)$$

Fast Fourier transform is an algorithm and it is faster than DFT but results are the same [80].

In this study, time dependent pressure data is decomposed by FFT algorithm. The observed frequencies after the signal processing, indicates that a geometric or physical feature in flow field. With the evaluation of the frequencies of the pressure data, cavitation or vortices can be detected in the turbine, due to its nature and fluctuated nature.

CHAPTER 4

REVERSE ENGINEERING METHODOLOGY

4.1 UTILIZATION OF REVERSE ENGINEERING APPROACH FOR TURBINE PARTS

4.1.1 Runner

Creating the mathematical model of the turbine runner requires a reverse engineering process for the runner blade as given in Figure 4.1. Three-dimensional geometry from the point clouds is created in SolidWorks using scanned data. The 3D blades are generated and used to create a meridional profile of the blade. This meridional profile is then imported to Bladegen software in order to generate the mathematical model. A 3-dimensional line following the blade boundaries and corresponding meridional profile in two dimensions are shown in Figure 4.2. Sectional drawing from manufacturer is shown in Figure 4.3.

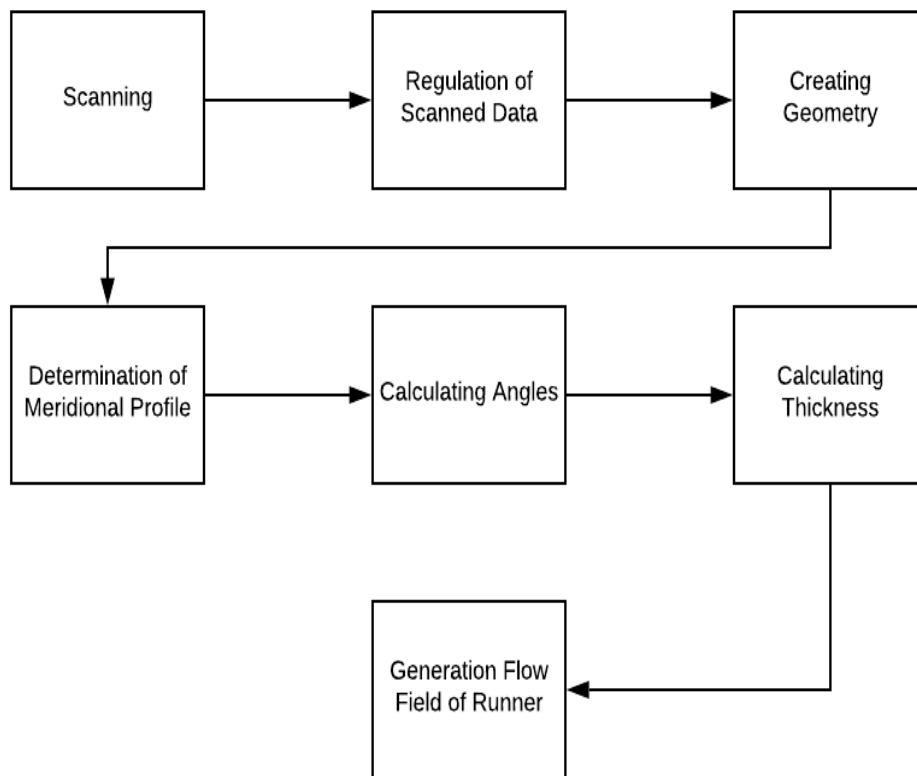


Figure 4.1: Runner reverse engineering procedure

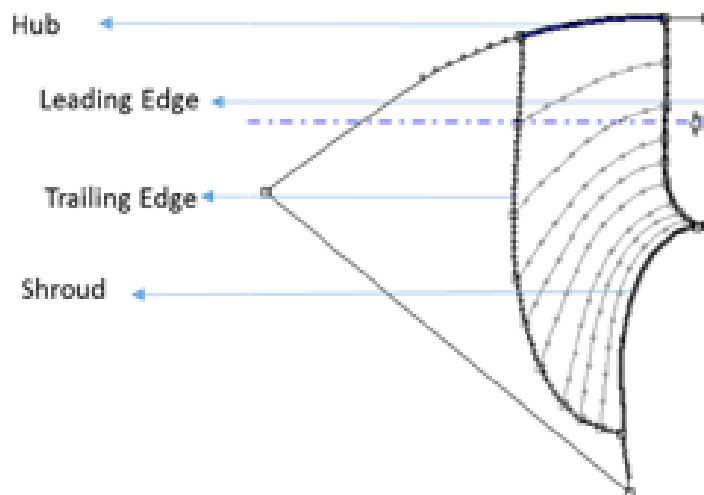


Figure 4.2: View of the meridional profile

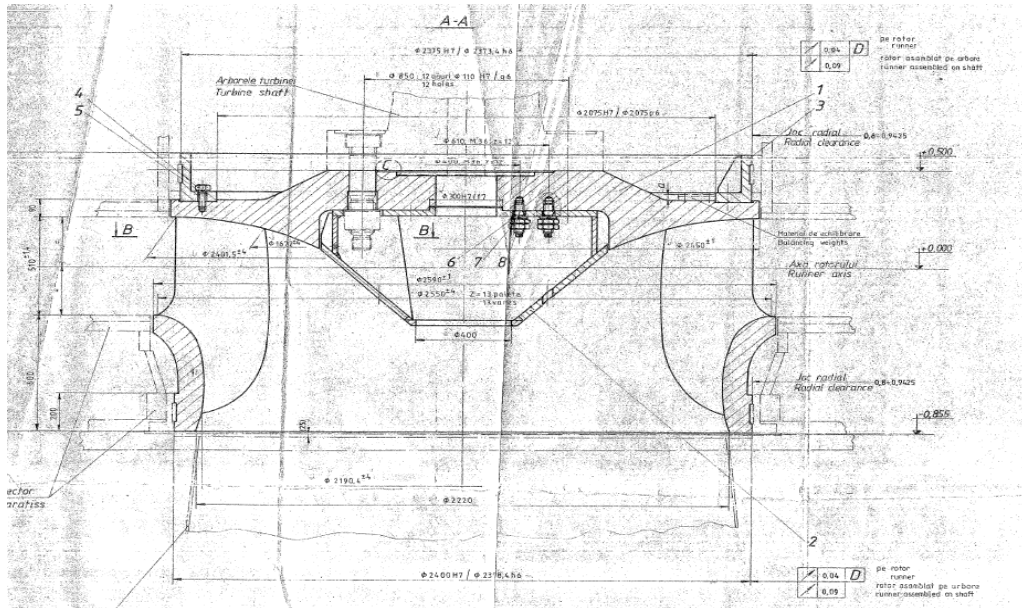


Figure 4.3: Sectional Drawing of the Francis Runner

The three-dimensional curves defining the trailing edge, leading-edge, hub and shroud are revolved on the rotation axis of the runner. A section on the midplane of the solid geometry is obtained by cutting the revolved body in half. The intersection curves are extracted, and meridional profile is obtained as shown in Figure 4.4.

To transfer the meridional profile to the BladeGen from Solidworks, 300 points with r and z coordinates are taken from the Solidworks and 2D coordinates are used in the BladeGen to obtain the model. The meridional profile of blade is splitted to meridional curves from hub to shroud as shown in Figure 4.4. These curves are defined by solving laplace equation on the meridional 2D domain. These curves are then exported back to solid model to slice the solid model in three dimensions at different locations from hub to shroud.

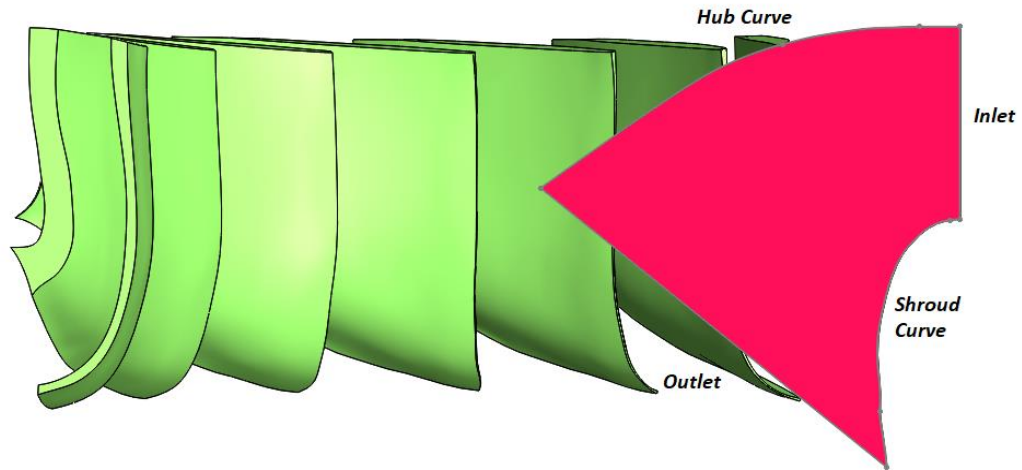


Figure 4.4 : Meridional section of the scanned runner

The intersection of these meridional curves and 3D blade geometry is defined as 3D-curves (called spans), as seen in Figure 4.5.

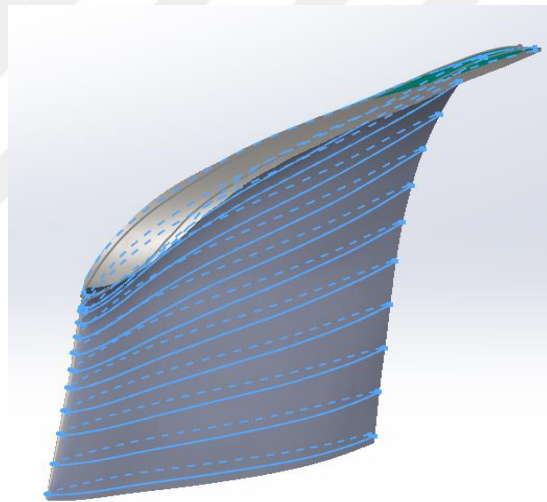


Figure 4.5: Defined spans on the blade

Once these spans are determined, beta and theta angles are calculated from the points on the blade surface. The metal angle of the blade (beta angle) is one of the parameters that are important to define the runner blade geometry. The direction of the runner blades at a given point is determined by the blade beta angle, which is the angle between the chamber of the blade and the tangent of the circle that is drawn from the center of the runner [57]. Theta angle is the angular position of that point in the cylindrical coordinates

The geometry of the blade is divided into the 11 spans from hub to shroud. For each span, 200 points are defined. The points on the span are transferred to Microsoft Excel. The chamber line is calculated by finding the midpoints between the curves on the pressure and suction side, as seen in Figure 4.6(b). These curves are then used to calculate the theta and beta angles of that span of the runner blade. The calculations are performed by using Eq (3.6) – Eq (3.10). By using as many points as possible in the span, reliable and accurate runner geometry, like the original runner, can be obtained.

The next step is to define thickness using the distance between the points that are taken from pressure and suction side as it is given in Figure 4.6 (a) by blue points.

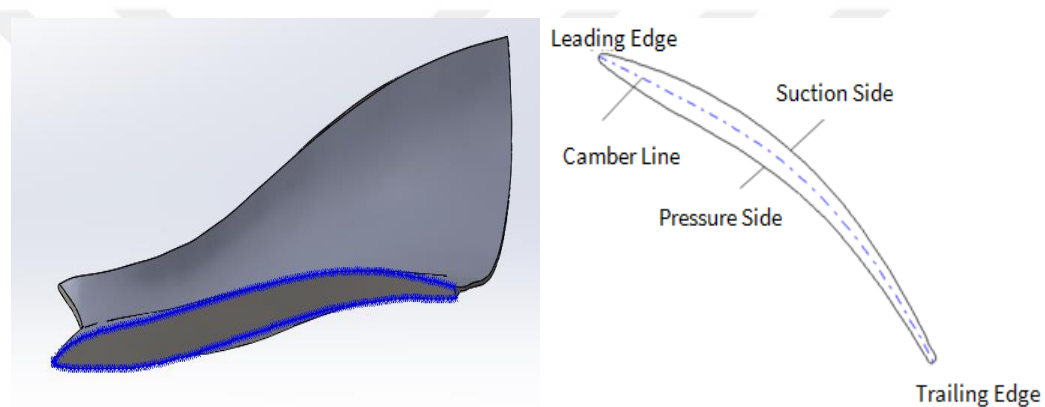


Figure 4.6 : (a) Thickness definition (b) Camber Line definition

For each of the span in meridional profile, angle, and thickness distribution of the blade profile are extracted from the Blade-Gen geometry in order to visualize the results. Plots of the resulting runner for a beta, theta, and blade thickness distribution are given in Figure 4.7.

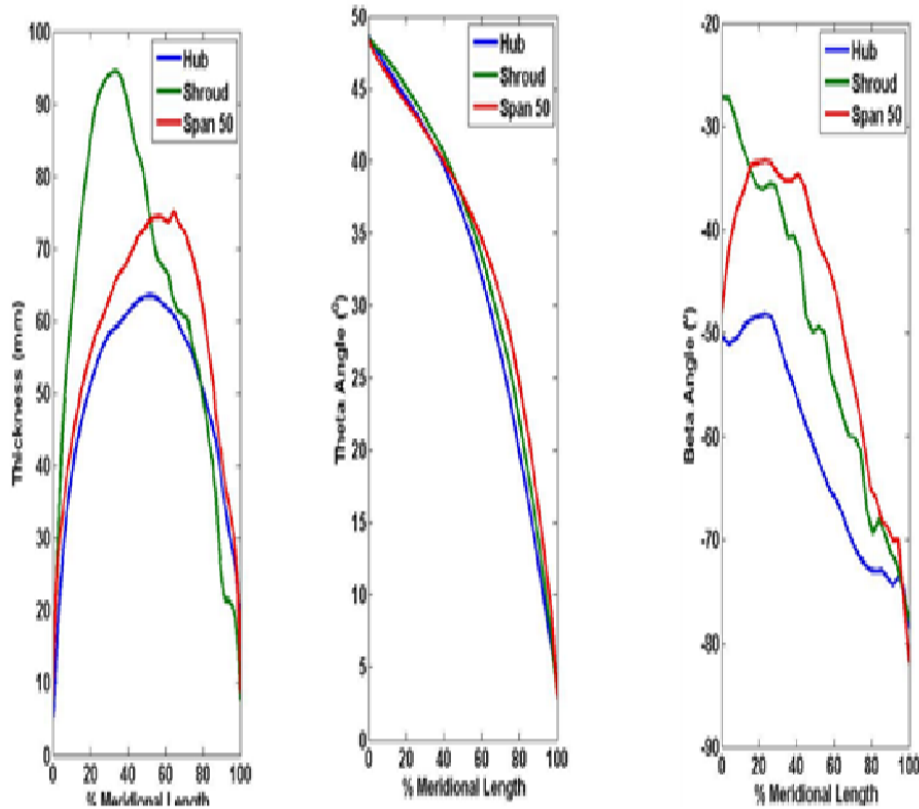


Figure 4.7: Thickness, Wrap Angle, Metal Angle distribution of Gezende HPP runner

4.1.2 Guide Vanes and Stay Vanes

The CAD modeling procedure of guide vanes and stay vanes are similar to runner procedure. As the guide vane and stay vane have the same profile in the Z direction, there is no need to define theta and beta distribution along the z-axis as a runner. The resulting solid model of the guide vane is shown in Figure 4.8. The geometry of these components is obtained using the same methodology, so the details are not repeated here.

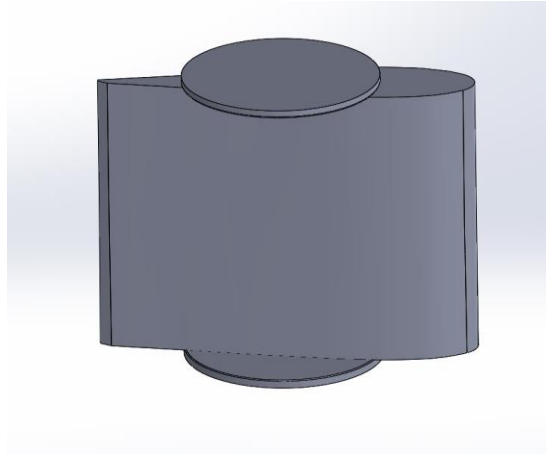


Figure 4.8 : Solid model of the Guide vane

The flow field of the guide vane's inlet edge and stay vane's outlet edge are set according to the runner inlet and spiral case outlet, respectively. Flow field and solid model of the guide vane is shown in Figure 4.9.

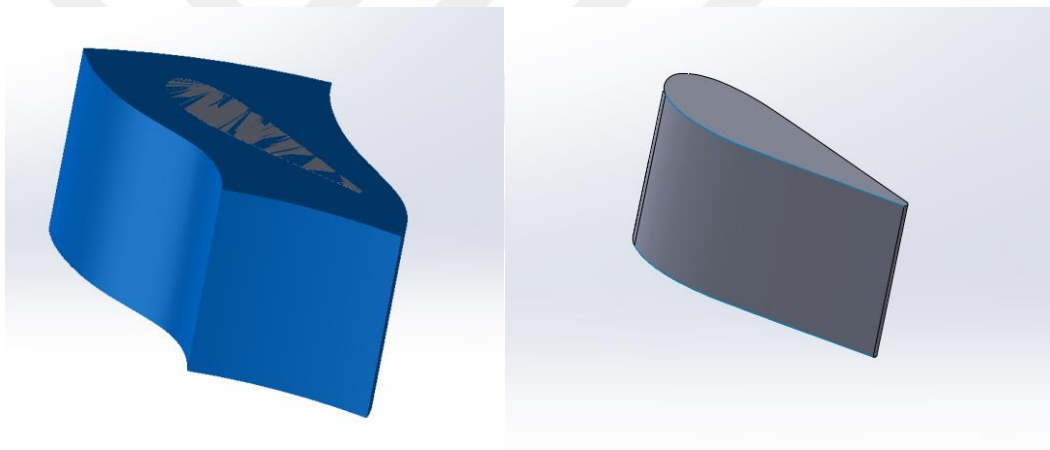


Figure 4.9: (a) The Flow Field of The Guide Vane (b) Solid Model of The Guide vane

4.1.3 Verification with IEC Standards and Model Runner

In the above procedure, the raw data is processed to obtain the mathematical model of the runner, i.e., reversed engineered runner. In order to use this mathematical model as a representative model of the real runner, the reverse-engineered runner and scanned runner need to be compared.

After all, data is imported to the Blade-Gen, reverse engineering blade, and scanned blade are compared with each other to observe the accuracy of the generated runner model. In Figure 4.10, a scanned blade and reverse engineered blade is superposed.

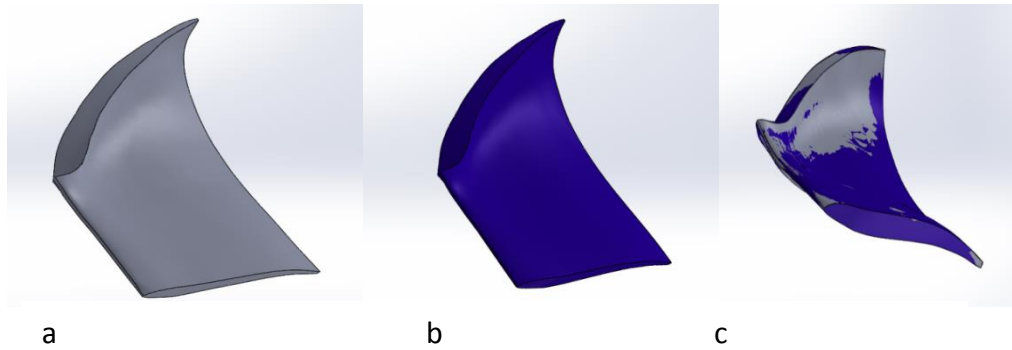


Figure 4.10 : (a) Scanned Blade (b) Reverse Engineered Blade (c) Superposed Blades

In IEC 60193 [31], permissible deviations in the geometrical similarity between model and prototype turbine are described. This similarity tolerance ranges are applied for the reverse-engineered and scanned turbine runner. As it is given in Table 4.1 and 4.2, the described geometrical parameters, uniformity tolerances and comparison between designed and scanned turbine runner is shown. In Table 4.1, inlet and outlet edges, remaining part of the surface, pitch, outlet opening (a) are compared with each other. Results show that all of the parameters are within range of the given permissible tolerances.

Table 4-1: Comparison between reverse engineering blade and scanned blade

	Location	Difference between RE and scanned Blade	Permissible Tolerance (mm)
	Pitch (P_i) (mm)	0.4041	5.2
	Surface (mm)	2.41	5.2
Surface	Shroud Edge Difference (mm)	4.18	5.2
	Hub Edge Difference (mm)	0.93	5.2
Inlet Edge	Inlet Hub Side (mm)	0.61	2.6
	Inlet Shroud Side (mm)	2.44	2.6
Outlet Edge	Outlet Shroud Side (mm)	2.45	2.6
	Outlet Hub Side (mm)	1.48	2.6

The geometrical similarity is the first condition to represent the two models that are similar. The second step is to see whether the kinematic conditions in both runners are identical or not. For this purpose, CFD analysis is performed to compare the efficiency, power values, and pressure distributions through both scanned and reverse engineered runners. In Table 4.2, performance comparison for CFD results is given. The maximum error is calculated as 0.41% in the efficiency value. Calculated error rates are small and probably arises due to mesh quality differences between reverse engineering blade and scanned blade.

Table 4-2: Performance Comparison between reverse engineering blade and scanned

	Scanned Runner	Reverse Engineering Runner	Error (%)
Power [MW]	52.44	52.22	0.40
Efficiency	96.63	96.24	0.41

In conclusion, both geometric and kinematic similarity between these two runners is obtained. Reversed engineered runner can be used to further analyze the turbine. Therefore, all simulations will be performed using the reverse engineered turbine runner with better mesh and high order solution algorithms.

4.1.4 Drawings for Draft Tube And Spiral Case

Manufacturer's drawings are used to obtain the geometry of the draft tube and spiral case. Draft tube and spiral case are created in sections. The flow area in the spiral case decreases linearly through the flow direction in the draft tube flow area increases towards the exit.

4.1.4.1 Spiral Case

The sectional area of the spiral case decreases through the flow direction. The diameter of each section is known from the drawings. Thus, the spiral case is modeled in CAD software using these drawings. The spiral case is modeled together with stay vanes as a single part for ease of meshing between the converging section between the spiral case and stay vane. The spiral case is modeled in 23 different sections. The diameter of each section was taken from manufacturer's drawings. Sections and diameter of each section are shown in Table 4.3.

Table 4-3: Measurements of the Spiral Case of Gezende HPP

Center		Section Diameter	
3355		2600	
3328	27	2550	50
3301	27	2500	50
3268	33	2430	70
3241	27	2390	40
3213	28	2340	50
3186	27	2290	50
3153	33	2230	60
3125	28	2180	50
3097	28	2130	50
3063	34	2070	60
3034	29	2020	50
3006	28	1970	50
2977	29	1920	50
2942	35	1860	60
2912	30	1810	50
2882	30	1760	50
2852	30	1710	50
2815	37	1650	60
2784	31	1600	50
2752	32	1550	50
2721	31	1500	50
2689	32	1450	50
2658	31	1390	60
2626	32	1340	50

Spiral case geometry is modelled on the SolidWorks Software. Sections, base plane, and solid model of the spiral case are given in Figure 4.11-4.12.

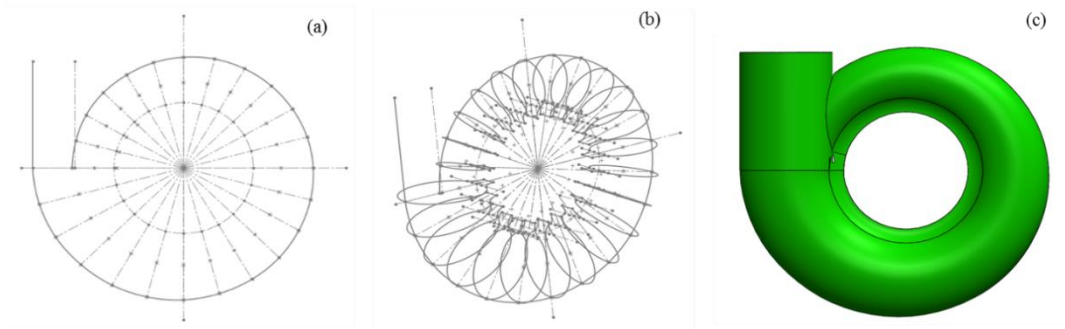


Figure 4.11 : Geometry Generation Process for Spiral Case

The last section of the spiral case where the buffer vane divides the last section and penstock is shown in Figure 4.12. Baffle vane photos taken from HPP during scanning field study are shown in Figure 4.13.



Figure 4.12: Buffer vane of the spiral Case



Figure 4.13 : Solid model of the Spiral Case

4.1.4.2 Draft Tube

Draft tube of the Gezende HPP consists 3 different parts which are elbow, cone, and diffusor. The technical drawing with dimensions were available at site and is shown in Figure 4.14.

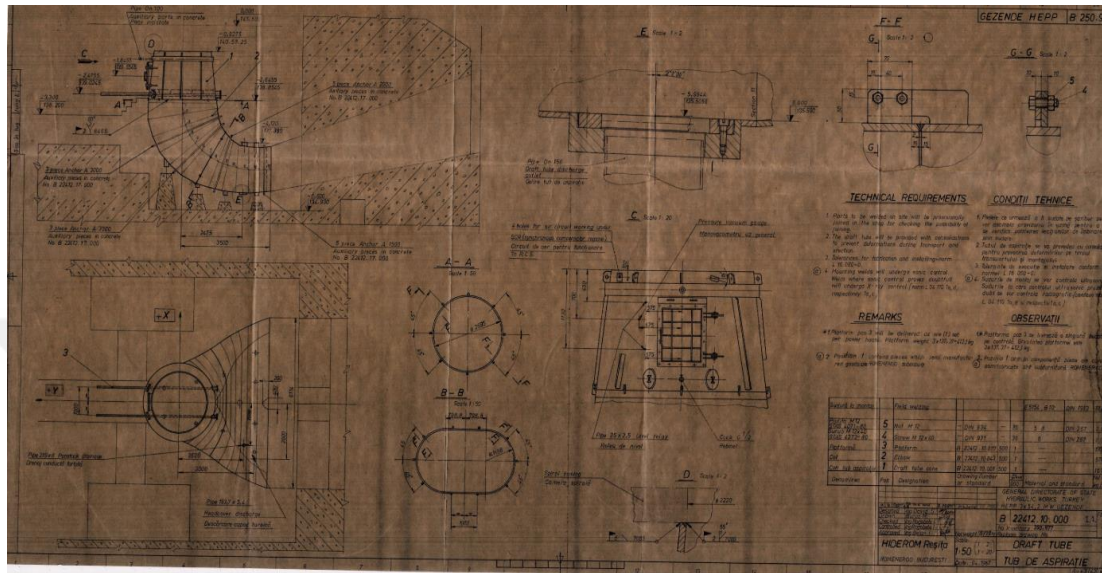


Figure 4.14 : Technical Drawing of Draft tube

All measurements are taken from the manufacturer's drawings given in Figure 4.15. Elbow is drawn in sections at certain intervals. Finally, all sections in Figure 4.16 are merged.

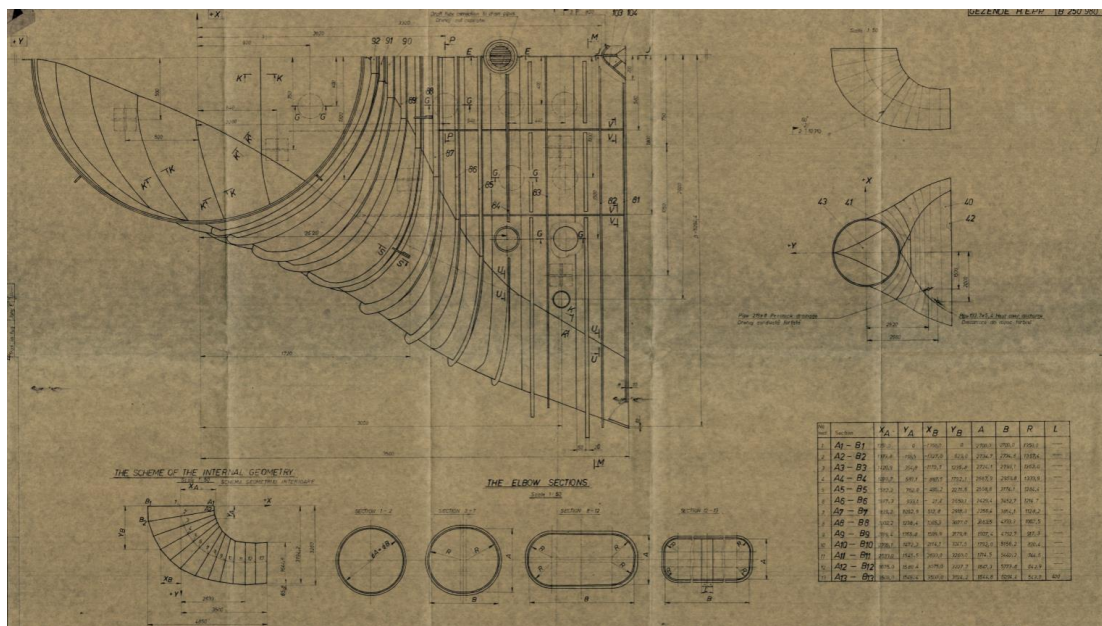


Figure 4.15: Technical Drawing of Elbow

The flow field of the draft tube is created on Solid Works Software with the above-explained methodology directly from manufacturer's drawings (Figure 4.16).

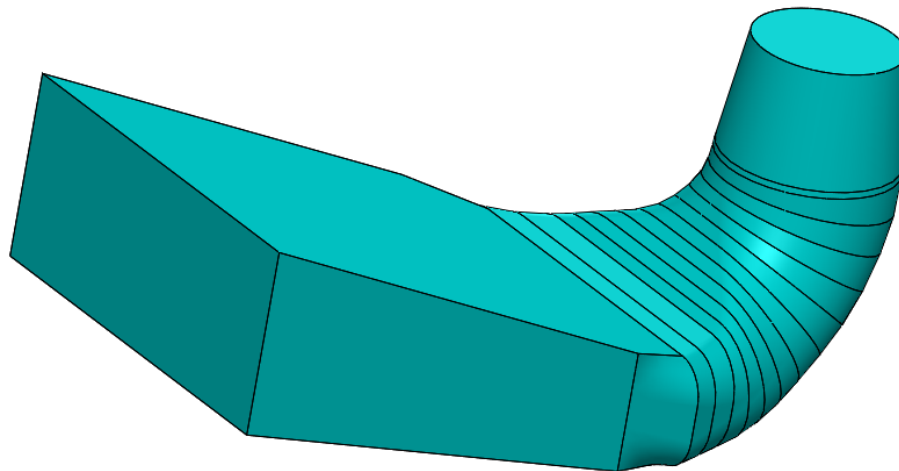


Figure 4.16: The geometry of Draft Tube

The cone is planted to the draft tube inlet to fill the area between the runner outlet and draft tube inlet (Figure 4.17).

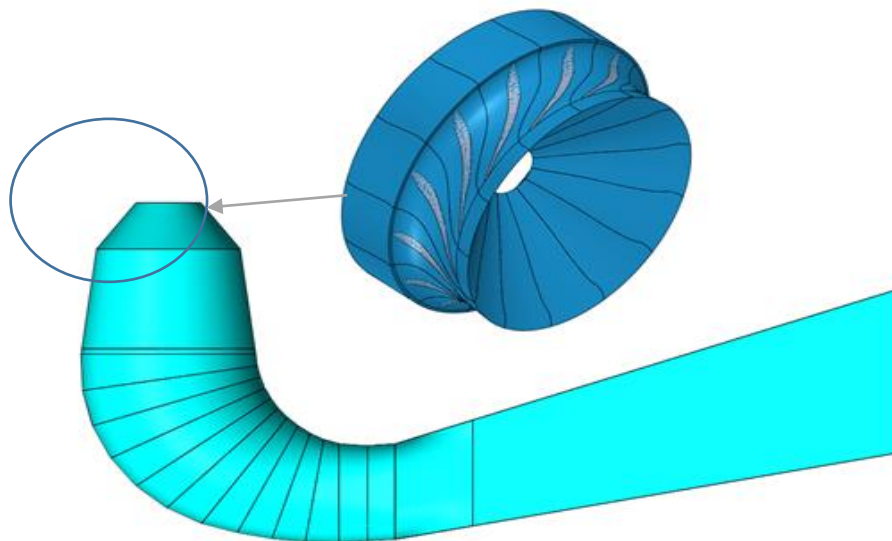


Figure 4.17: Additional Cone for Runner

4.1.5 3D Geometric Model of The Gezende

In conclusion, all components of the turbine, spiral case, stay vanes, guide vanes, runner, and draft tube are obtained in CAD format. The geometries of stationary and rotational blades are created with scanning technology, other parts are created using manufacturers CAD drawings. As the runner is the major components that controls

the power output and efficiency, scanned and reverse engineered blades are tested and compared until a geometric and kinematic match is achieved between them. Manufacturer's drawings are utilized to define origin of the geometry, draft tube and spiral case sections and dimensions. Final flow field of the Gezende HPP is shown in the Figure 4.18.

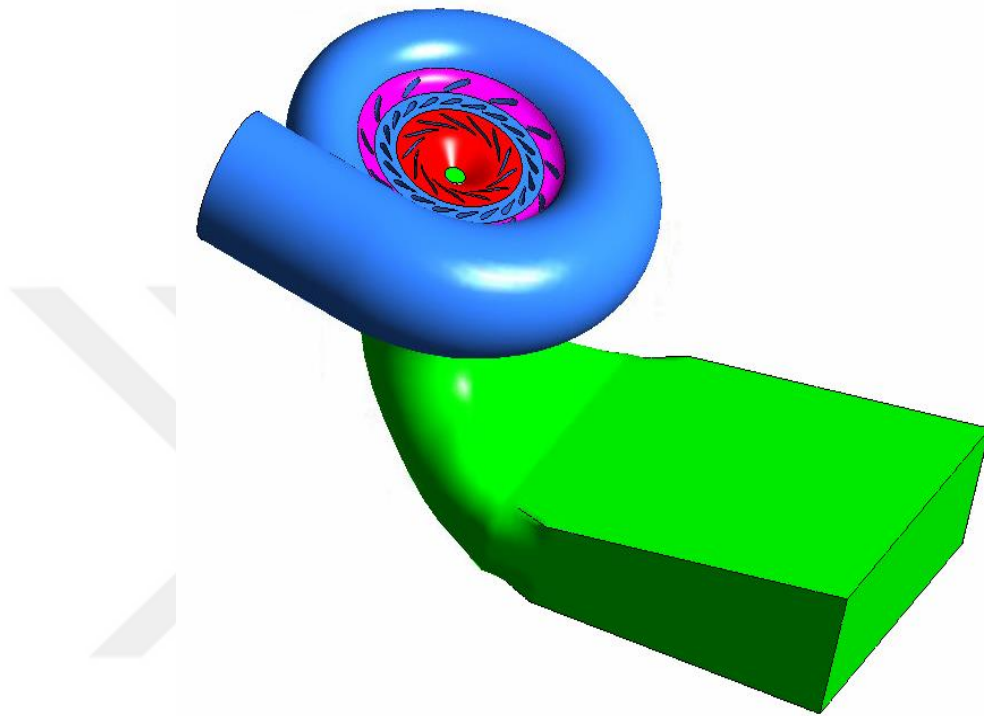


Figure 4.18: Full turbine of the Gezende HPP

CHAPTER 5

COMPUTATIONAL FLUID DYNAMICS ANALYSIS OF GEZENDE HPP

For the original turbine configuration of GEZENDE HPP using the mathematical models, which are obtained with reverse engineering, firstly, all components are analyzed separately, and then full turbine analysis is conducted. The analysis is carried out at different flow rates and head values to observe the behavior of the turbine at various operating conditions. Analyses at off-design points are used to examine the performance of the turbine at partial and overload conditions. Figure 5.1 shows the total machine configuration which is ready for CFD analysis and mesh structures for all of the components.

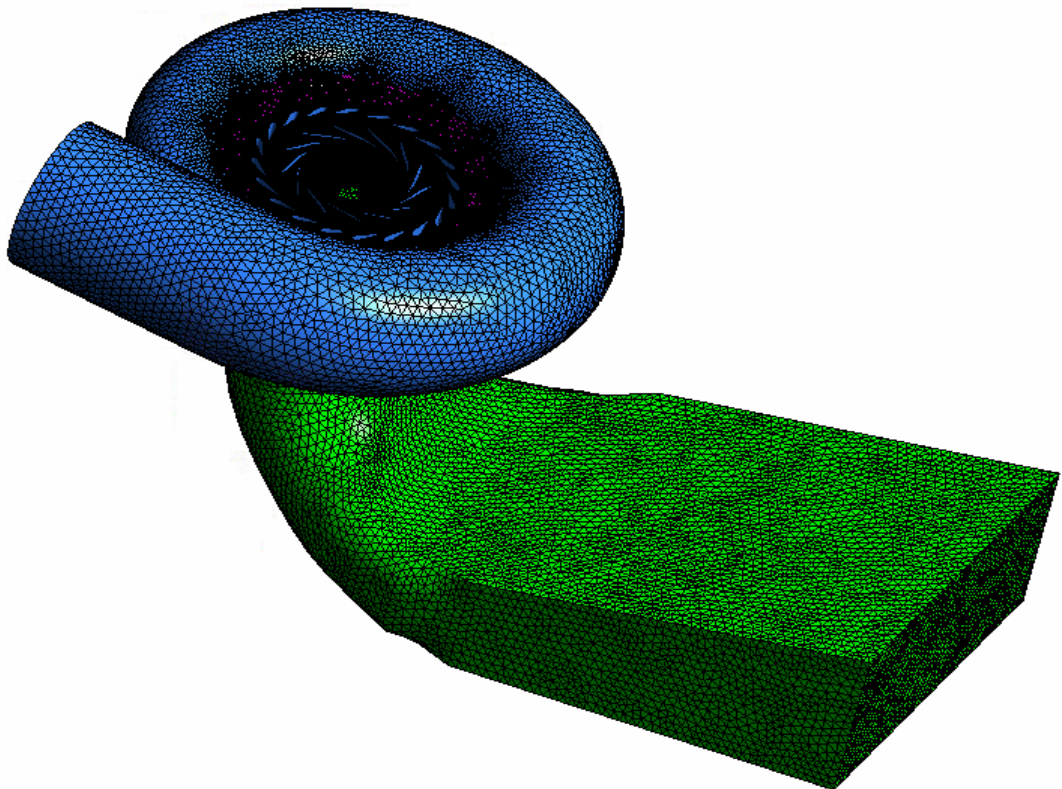


Figure 5.1 : Mesh Structures for components of the Gezende

Different opening percentages and different volumetric flow rates for each opening of guide vanes are necessary to develop a numerical hill chart for constant rotational speed. Analyses are performed for a range of head values. The following CFD methodology is utilized, as shown in Figure 5.2.

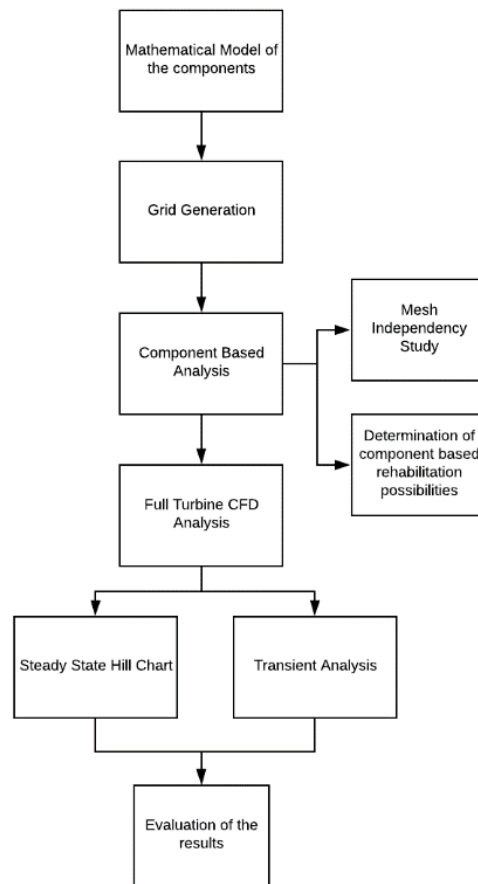


Figure 5.2: CFD Methodology

5.1 COMPONENT-BASED CFD ANALYSIS

CFD studies start by performing mesh independency study for all the components based on the mathematical models that are obtained with the reverse engineering method.

5.1.1 Mesh Independency Study

A converged and mesh independent result is obtained when the chosen parameters do not change significantly with the number of mesh elements. The computational domain is meshed using unstructured grids, which consist of triangular and tetrahedral elements. In order to capture the complex flow structure in the clearance regions, the mesh inside has been well-controlled and refined.

For each of the components, the mesh is tightened in the regions where the flow is the critic and has a dominant effect on the performance. For the spiral case and stay vane, a mesh is finer in the periphery of the stay vanes, for guide vane and runner mesh is finer in the blade periphery and the draft tube, the elbow has more mesh elements. In Figure 5.3, mesh refinement regions are given for spiral case and draft tube.

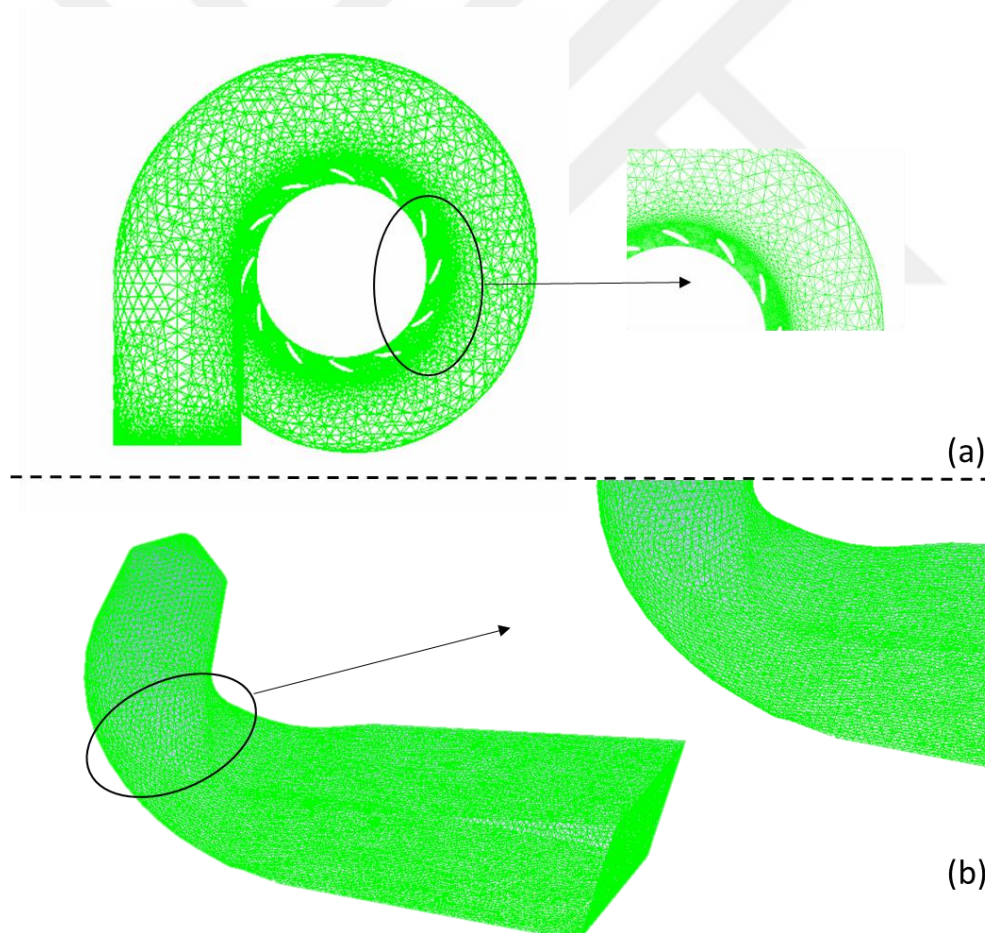


Figure 5.3: Mesh refinement regions for (a) Spiral case (b) Draft tube

In Figure 5.4 and 5.5, Mesh structure are shown for guide vane and runner blade. Especially, runner mesh is much finer compared to the other components in the

entire domain. This is because runner is the most important component in the turbine due to the directly effect on efficiency.

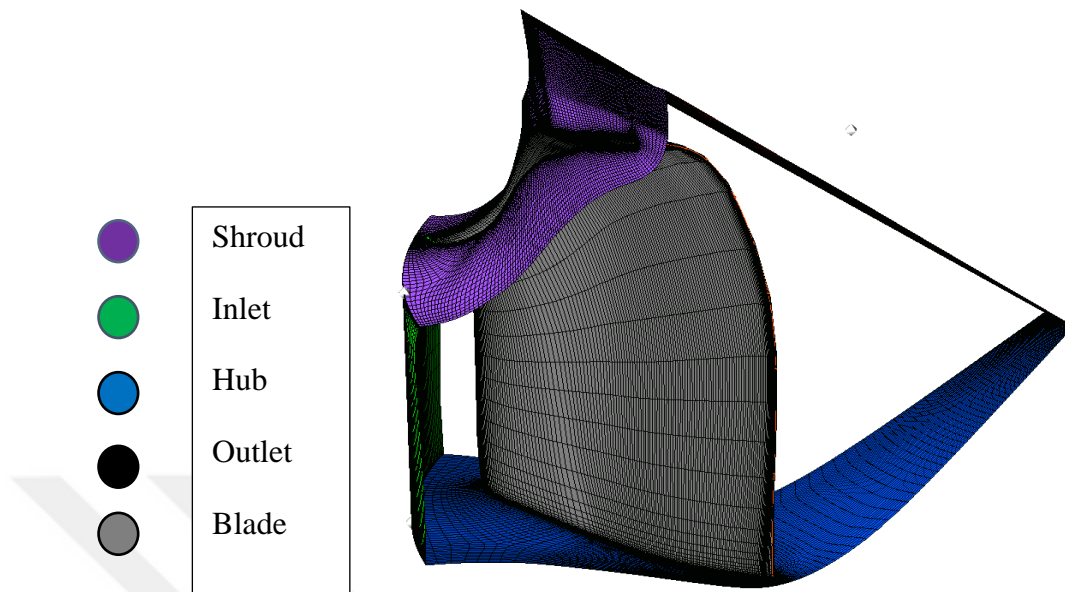


Figure 5.4: Mesh Refinement Regions For Runner Blades

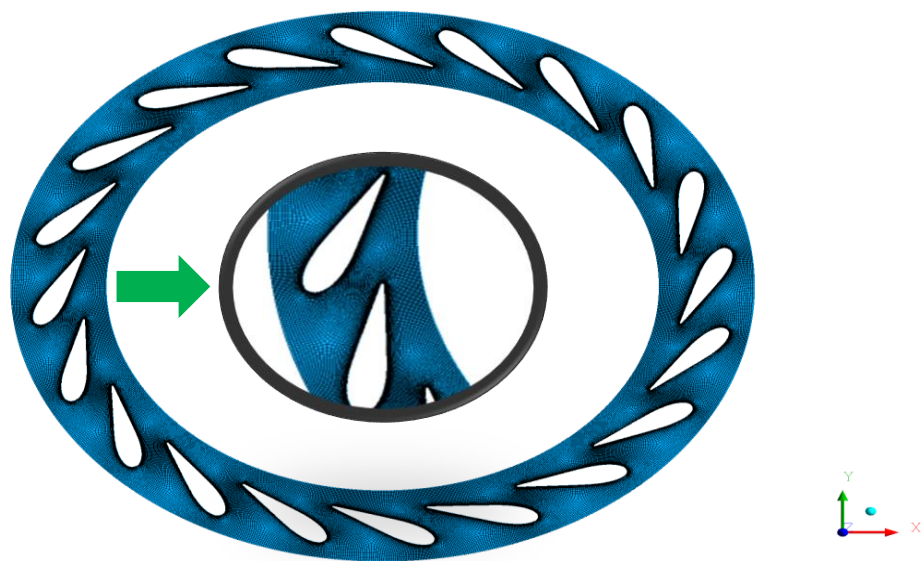


Figure 5.5: Mesh Refinement Regions For Guide Vanes

In Table 5.1, the results of mesh independency study are given for all components. Separate meshes are used for rotating and stationary components due to the complexity of the geometries. Using the same number of elements, cell size and distribution for all simulations is very difficult; therefore, Generalized Grid Interface (GGI) method is used to transfer all flow gradients through non-conformal meshes.

Table 5-1: Mesh independency results for turbine components

Component	Control Parameter	Number of Mesh Element	Relative Error (%)	
Spiral Case & Stay Vane	Efficiency	0.976	354000	
		0.979	431000	0.36
		0.962	536000	1.78
		0.951	795000	1.21
		0.952	1300000	0.11
		0.954	1500000	0.19
Spiral Case & Stay Vane	Flow Angle Outlet	-60.960	354000	
		-59.680	431000	2.14
		-60.680	536000	1.65
		-59.820	795000	1.44
		-59.800	1300000	0.03
		-59.800	1300000	0.03
Guide Vane	Outlet Angle	-75.062	20000	
		-74.645	100000	0.56
		-74.450	250000	0.26
		-74.414	500000	0.05
Runner	Efficiency	93.875	20000	
		95.802	100000	2.01
		96.543	250000	0.77
		96.887	500000	0.35
		97.011	750000	0.13
		97.060	1000000	0.05
Draft Tube	Pressure Recovery Factor (Cp)	0.871	28000	
		0.881	87000	1.10
		0.881	201000	0.06
		0.838	504000	5.06
		0.819	870000	2.41
		0.805	1200000	1.66
		0.796	1700000	1.17
	0.792	2200000	0.44	

5.2 FULL TURBINE STEADY STATE CFD ANALYSIS

In this part of the thesis, after reaching the mesh independent results for each of the components, full turbine analysis is conducted, and head-discharge operating characteristics of the existing turbine are investigated. 40 full turbine simulations for different guide vane openings and head values, with 36 million grid points each, are simulated to obtain a hill chart that demonstrates the behavior of the turbine for a wide range of head and flow rates representing the off-design conditions of turbine operation. In Figure 5.6, operating ranges to obtain a hill chart is shown. In Figure 5.7 hill chart is given. The graph shows the isoclines of efficiency (η). The blue star denotes the operating point of the HPP, while orange denotes the best efficiency point. In the existing design, the design point cannot reach the maximum efficiency of the system. When the turbine is used off limits, keeping the efficiency as high as

possible is an important constraint. Therefore, if the rehabilitation will be made on this HPP, two important parameters that should be considered are widening the operating condition and getting closer to the design point to the best efficiency point. In Figure 5.8, guaranteed efficiency values from manufacturer for different operating conditions are shown on the hill chart and it is depicted that guaranteed and CFD efficiency results are consistent with each other.

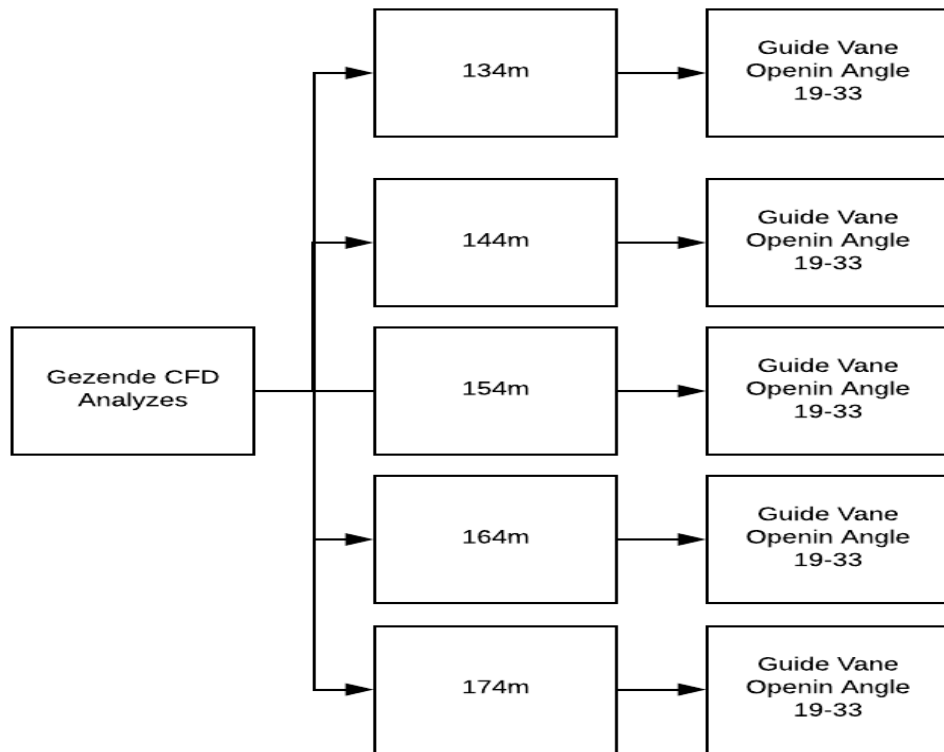


Figure 5.6: Simulation process for Gezende Hill Chart

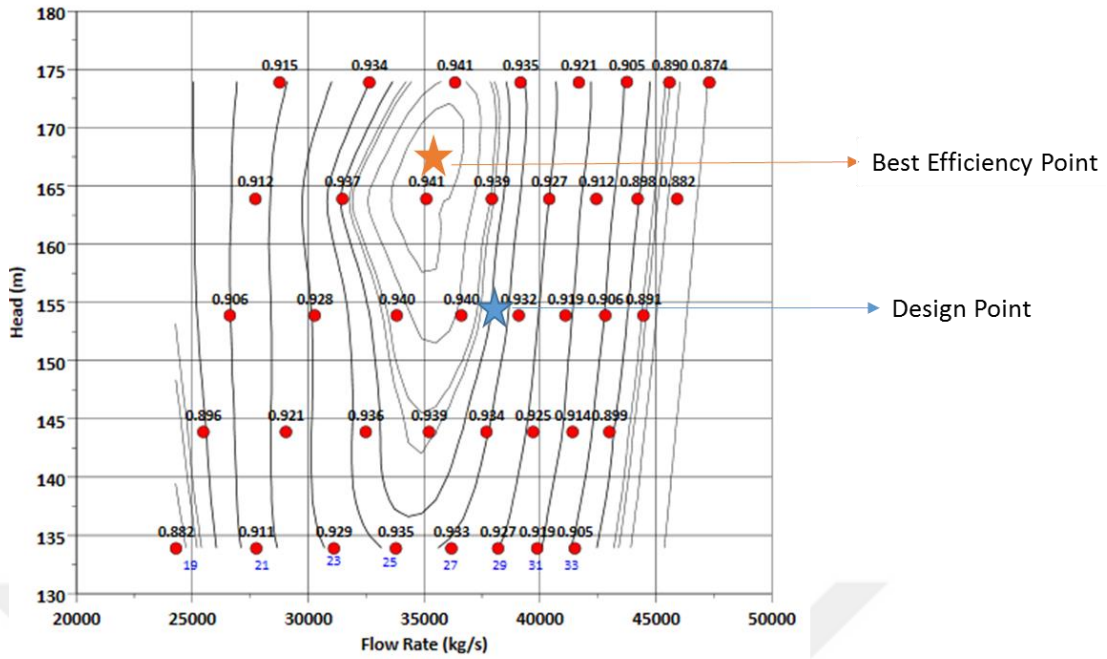


Figure 5.7: CFD operating conditions to obtain Hill Chart

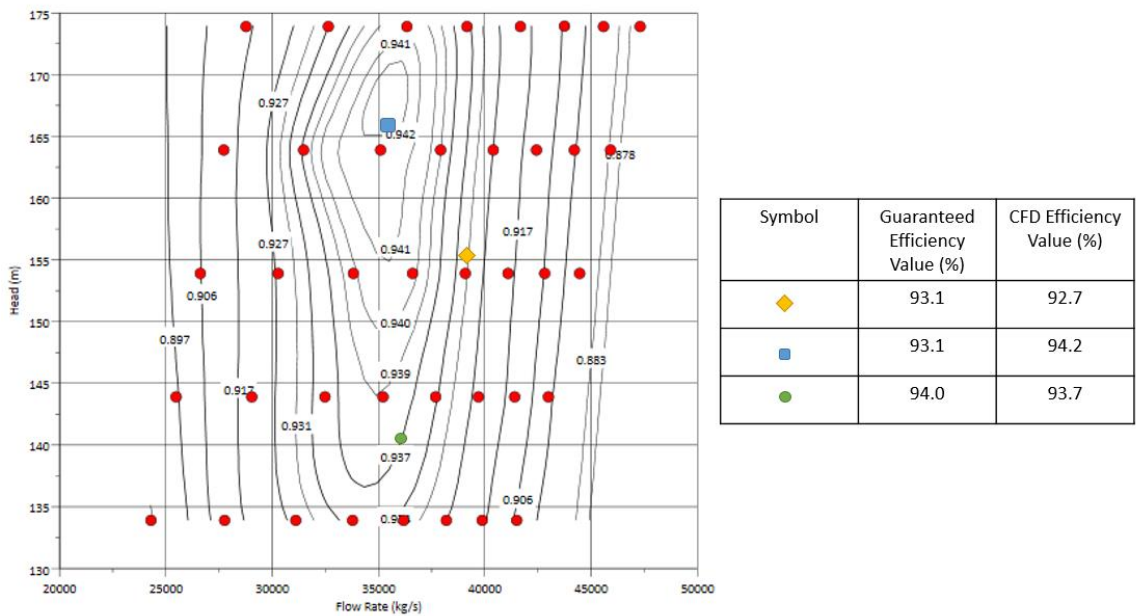


Figure 5.8: Hill Chart for GEZENDE HPP with BEP point

In Figure 5.9, an operating region of Gezende HPP is shown in the hill chart. Although, design point and best efficiency point lines within the operating region, if the refurbishment will be performed for this HPP, the design point should be shifted to the middle of the operating region with higher efficiency.

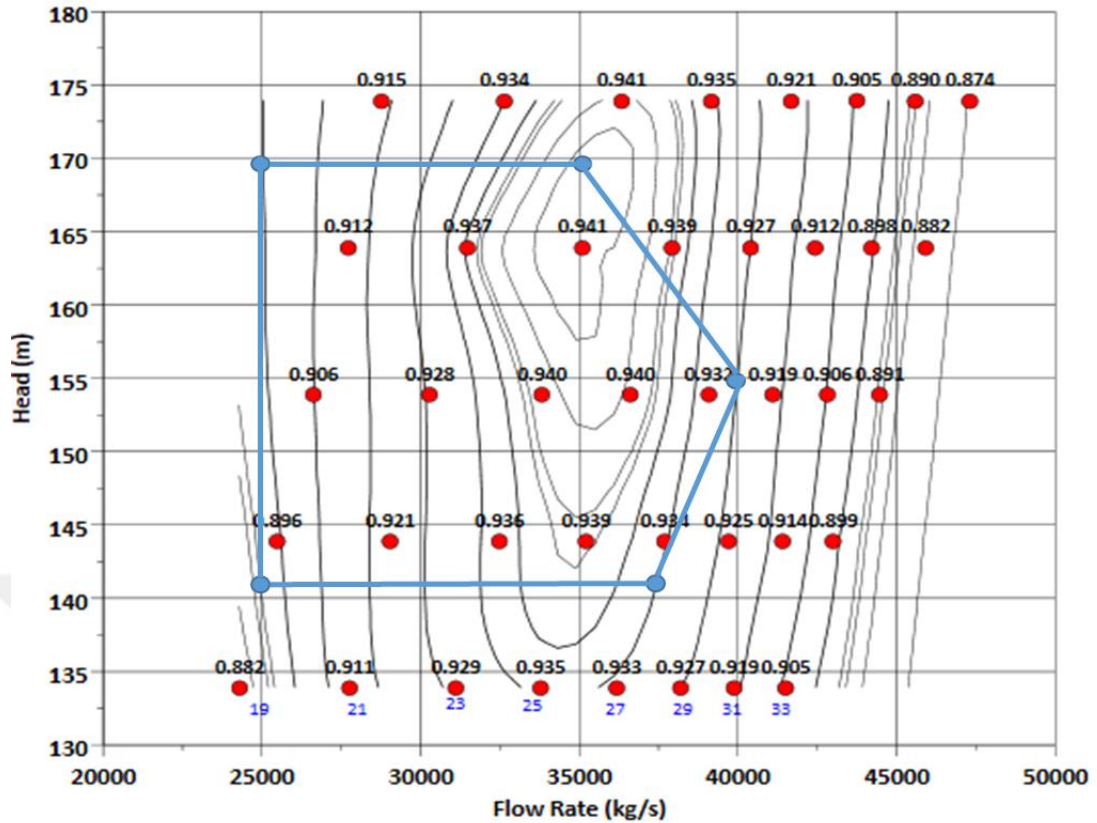


Figure 5.9: Operating region for GEZENDE HPP

Once the local sigma value exceeds the sigma plant value, cavitation bubbles begin to form and grow. Thoma contours were drawn for visualization of cavitation in the turbine runner. In addition, Thoma graphs were drawn, and the areas exposed to cavitation were determined. In Figure 5.10, for different loading conditions, Thoma number distribution is shown, and Sigma Plant is calculated as 0.136 for Gezende HPP.

When Local Thoma number exceeds 0.136, it means that cavitation occurs in the runner. When Figure 5.10 is examined, with increasing the flow rate of the system, cavitation rises. In the 110 % loading situation, the region that experience cavitation reaches to 27 % of the blade suction area. Conventional turbine runners like the one under investigation in this research, are prone to cavitation damage especially on the suction side of the blade. To minimize the cavitation and increase the performance, the X-blade turbine runner design is introduced by Billdal [73]. By changing the blade to x-blade configuration, cavitation is minimized while increasing the efficiency and performance [20]. The most hazardous cavitation types which are

leading edge and inter-blade vortex types, are not observed in this blade it is the one of the reasons that this turbines performance is high.

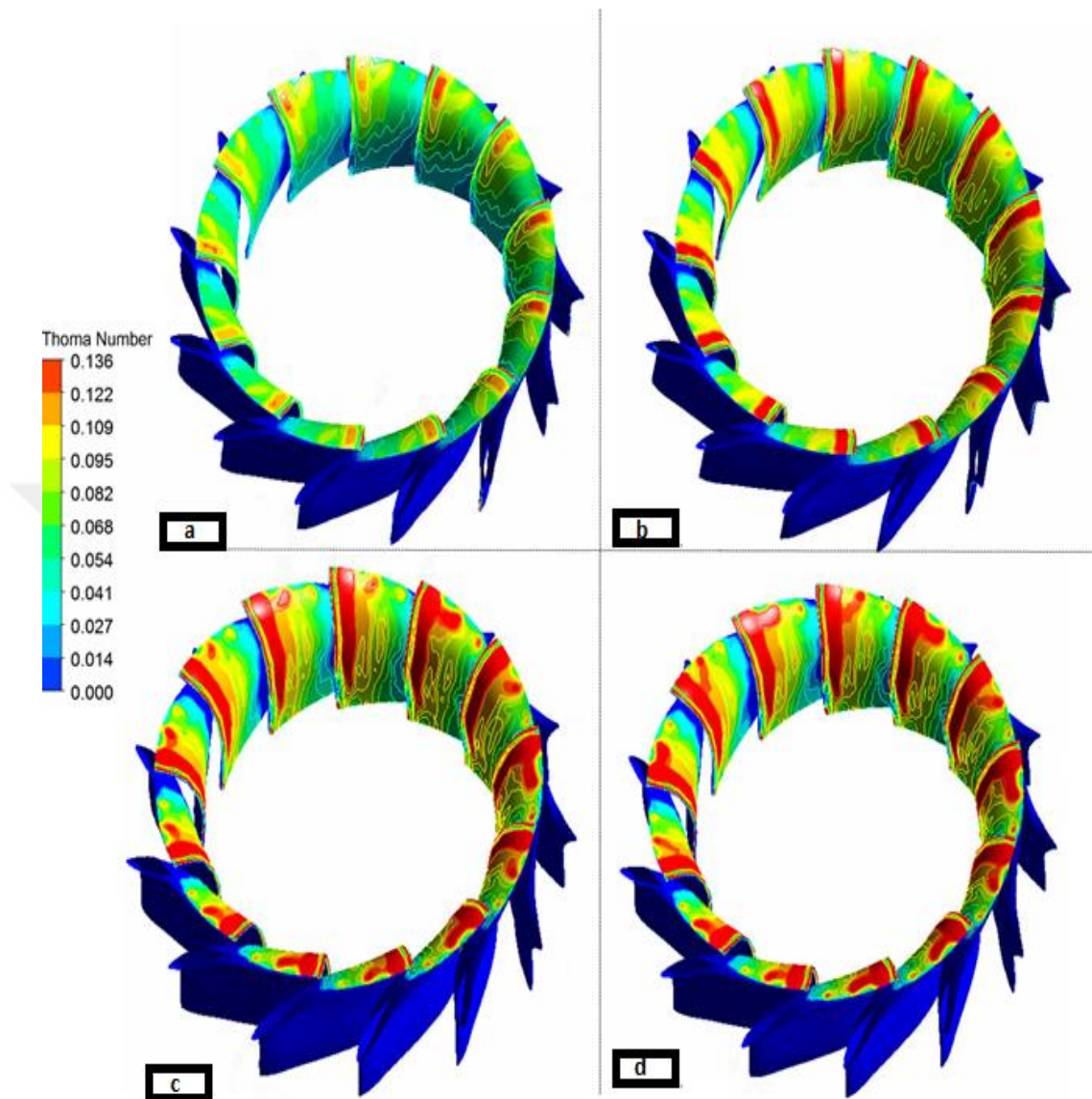


Figure 5.10: For different loadings Thoma number distribution through the runner (a) 68% loading (b) 87 % loading (c) 101 % loading (d) 110 % loading

In Figure 5.11a, the turbine runner of Gezende HPP is shown. Thoma number distribution (5.11b) has a similar trend with the real turbine runner. Other than small undulations on the surface of the runner blades, the profile was not showing characteristics of any cavitation. This may be due to the natural air admission through the shaft. Although the effect of air admission extends the lifetime of the runner, the efficiency will be reduced significantly. The locations subject to low pressure on the runner suction side is visible. Suspended materials usually attach to the low-pressure zones as seen in the runner photo (black debris).

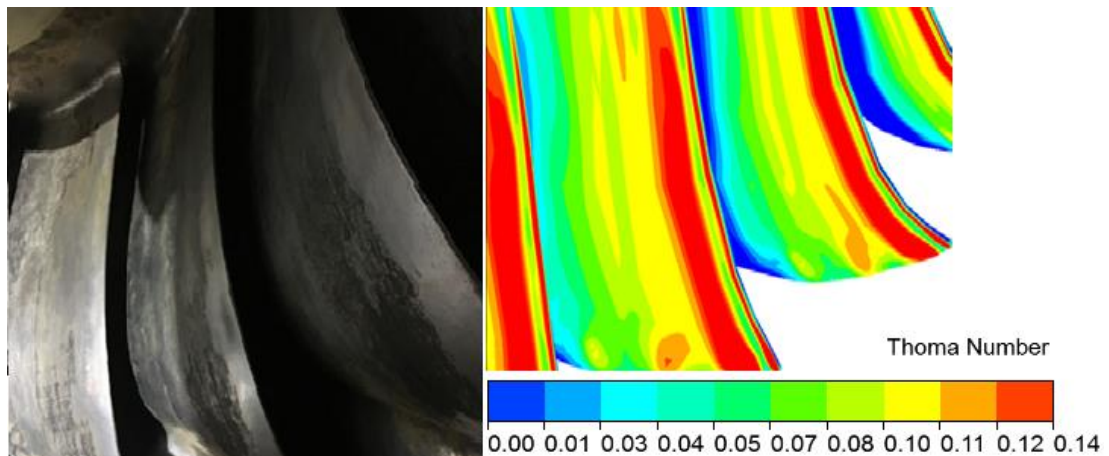


Figure 5.11: a) Runner blades b) Thoma Number distribution

In Figure 5.12, for different spans, Sigma distribution is given from hub to shroud. When the sigma values at any location are higher than the sigma plant it means that this region suffers from cavitation. It is observed that, especially near the shroud, the turbine runner is exposed to the cavitation.

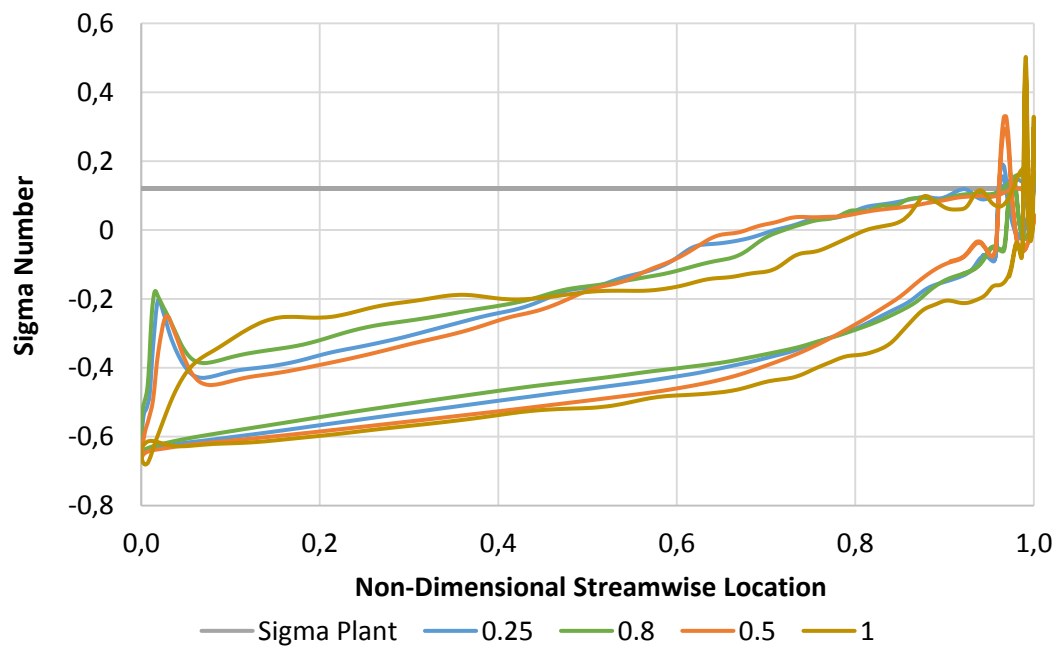


Figure 5.12 : Thoma number distribution for different spans (101% loading)

Static pressure loadings from leading edge to trailing edge for both suction and pressure side gives an idea about the cavitation phenomena and the working principle of the turbine blades (5.13). Hydraulic energy is converted to mechanical energy by decreasing the pressure inside the runner, thus using the hydraulic energy

of the water. As it is seen from Figure 5.13, on both sides (pressure and suction sides) pressure values are decreases from leading edge to trailing edge. As it is said before, when local pressure value is smaller than the vapor pressure, cavitation occurs. For the site conditions in Mersin, where Gezende HPP is located, vapor pressure is determined as 4.5 kPa. As seen in the pressure distribution plot, near the trailing edge, shroud cavitation occurs where pressure values are lower than the vapor pressure. In order to minimize this low-pressure zone, Ayli et al [20] suggested introducing a leaning at the hub in the direction of the rotation. Also from the pressure distribution, it can be noticed there is no leading edge cavitation on the blade.

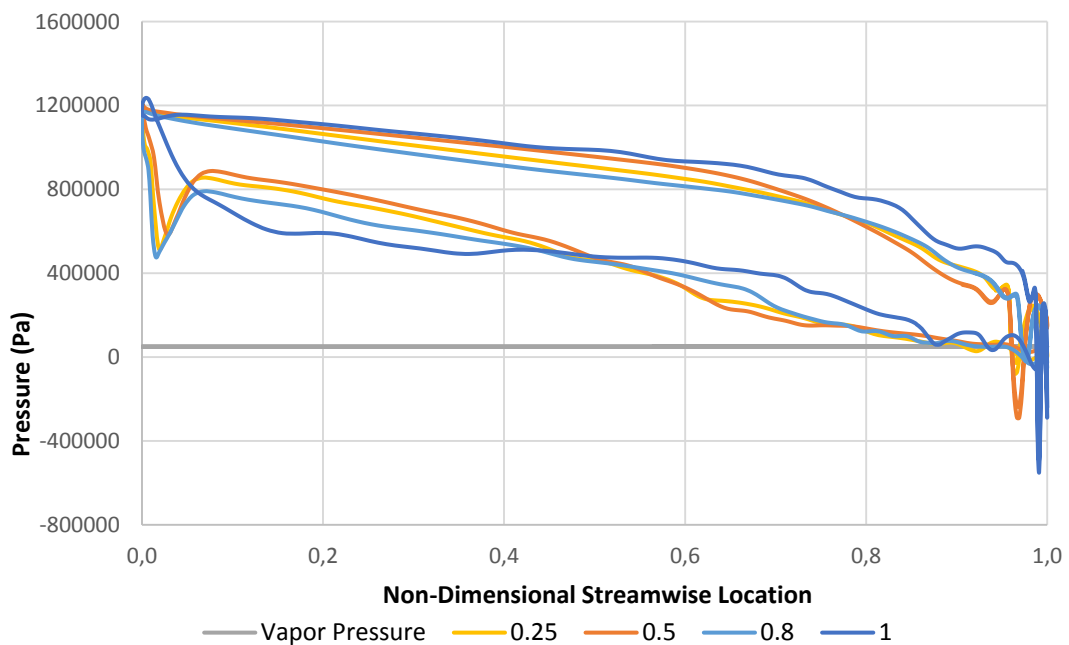


Figure 5.13: Pressure distribution for the runner (H=154 m, Guide Vane Opening= 25°)

In Figure 5.14, for 154 m head and 25° guide vane opening condition, streamlines, and velocity vectors are shown. In this Figure, in the blade pressure side, vertical structures and separations are observed. Those structures decrease the pressure values in the pressure side and cause a performance reduction in the runner.

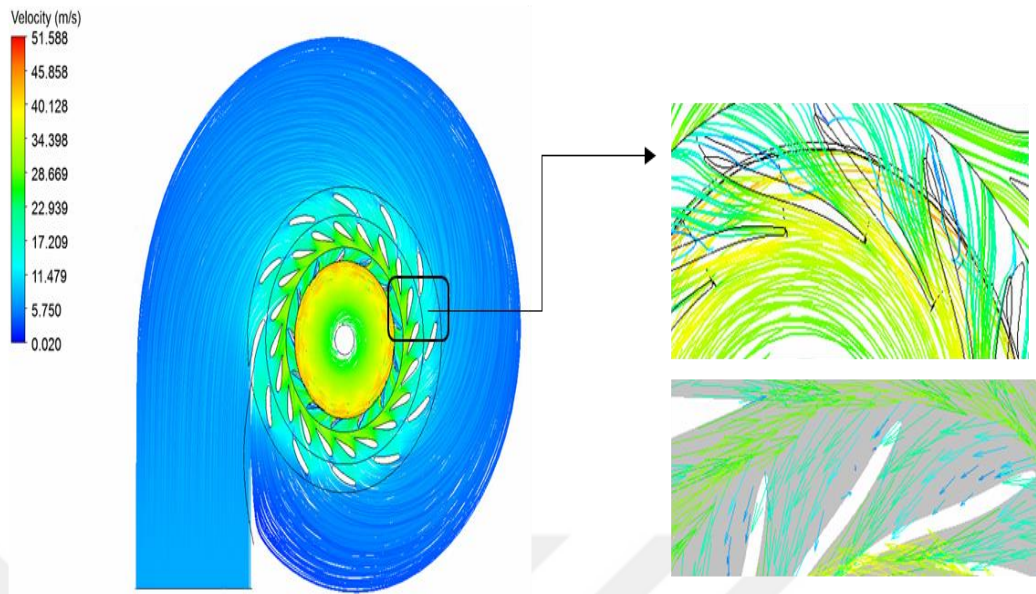


Figure 5.14: For full loading conditions streamlines and velocity vectors ($H=154$ m, guide vane opening= 25°)

In Figure 5.15 and Figure 5.16 from hub to shroud for runner inlet and outlet circumferential and meridional velocity profiles are given. When the theoretical formulation, given in the kinematics of Francis turbines part, is considered; circumferential trailing edge velocity value should be zero to maximize circulation that is generated in the runner. But for this design, it is observed that the hydraulic energy of the water is not used fully, therefore, the power generation potential of the runner is not completely used.

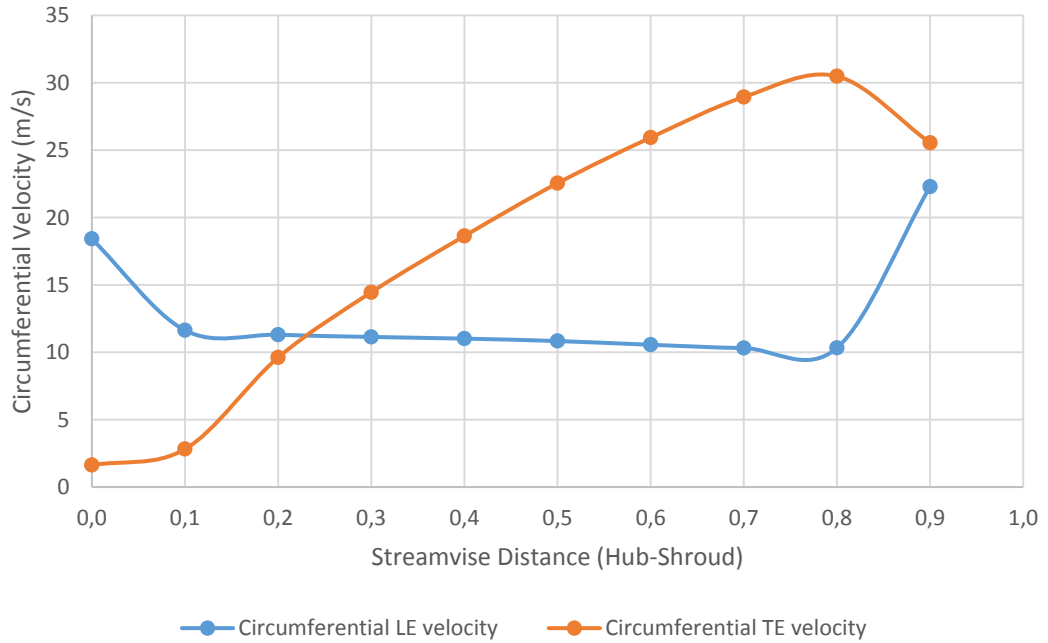


Figure 5.15: Circumferential velocity distribution from hub to shroud for 101% loading

For runner performance, meridional velocity distribution in the leading edge and trailing edge should be parallel to meridional sections; thus, uniform flow rate distribution is obtained.

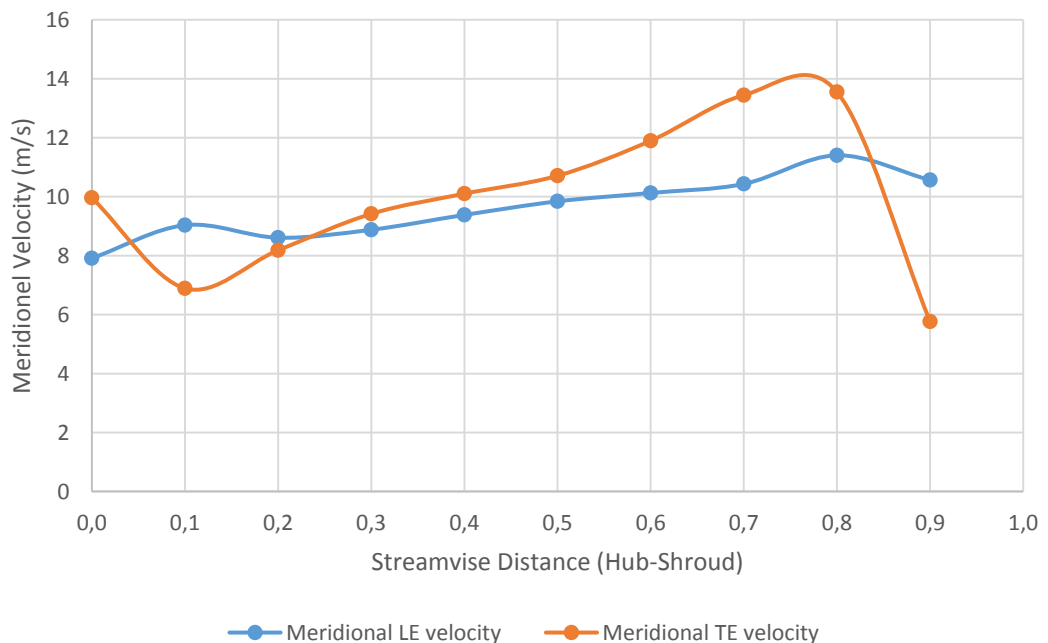


Figure 5.16: Meridional velocity distribution from hub to shroud for 101% loading
 In Figure 5.17, total pressure distribution on the meridional surface for 101 % loading is shown. Runner is the key component of the turbine as power is generated in this

part, also as it dominates the hydraulic losses, runner has a critical role in the total efficiency of the machine.

Figure 5.17 also exhibits almost uniform pressure distribution through the runner. On the other hand, to obtain a better flow field, turning the conventional turbine blade to x-blade can be a solution.

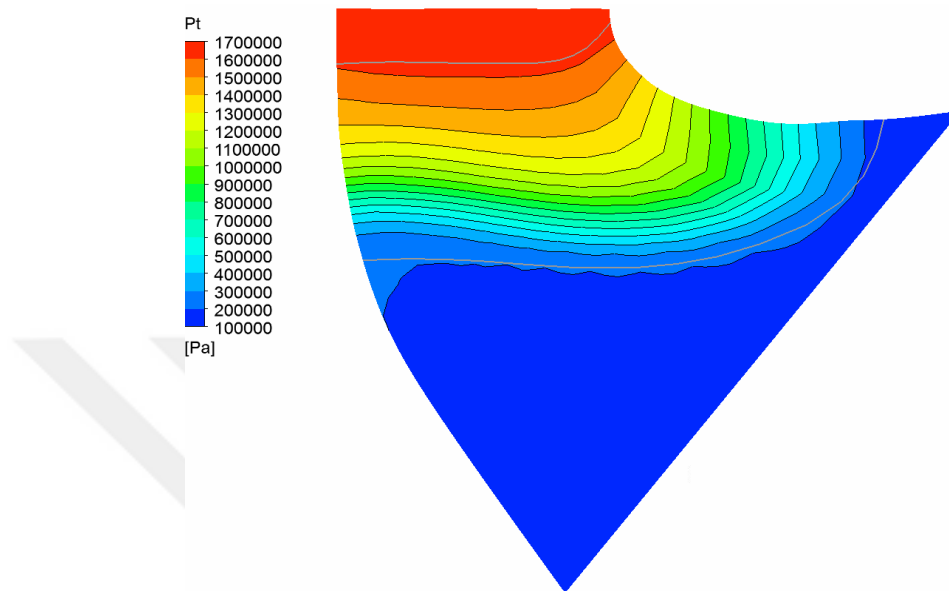


Figure 5.17: Total Pressure distribution on meridional surface for 101 % loading

In Figure 5.18, stagnation points are represented by blue fields which is velocity nearly zero. It is clearly seen from the figure; stagnation points are not on the leading edge of the blade. This can be main reason of the efficiency reduction in runner efficiency. However, there is no flow separation and unexpected vortices seen.

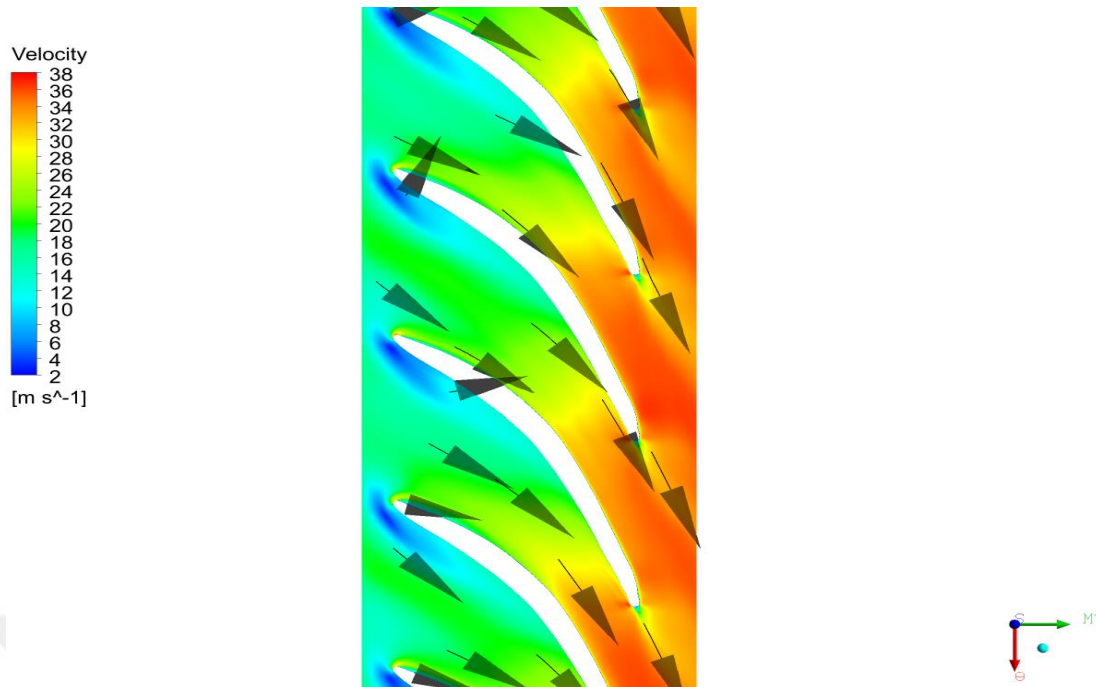


Figure 5.18: Velocity Vectors and Magnitude in the Runner (%50)

In Figure 5.19, the pressure decreases gradually from leading edge to the trailing edge which also means increase in the velocity through LE to TE. This situation indicates that optimum guide vane angle is determined correctly for Gezende HPP. Also, stagnation pressure occurs in the symmetry point of the guide vane, which is the another sign of the correct guide vane angle.

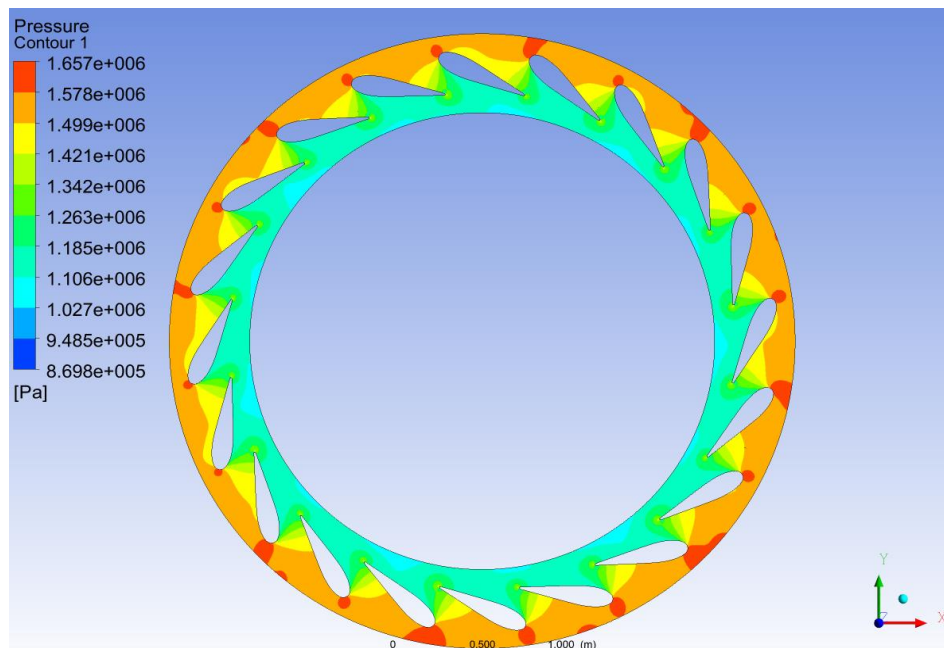


Figure 5.19: Pressure distribution on the Guide Vane (%50 Span)

5.3 DETERMINATION OF OFF-DESIGN PERFORMANCE OF THE TURBINE

40 possible flow rate and head combinations are simulated to determine the off-design performance of the turbine. The flow rate is adjusted by changing the guide vane opening.

In Figure 5.20, a loading-efficiency graphic is given for design head value. After nearly 90% loading efficiency starts to decrease. The location of the best efficiency point at 90% loading is desired as long as the turbines are not operated at overload regions. Operation characteristics and loadings should be investigated to check if this is suitable for the operation history.

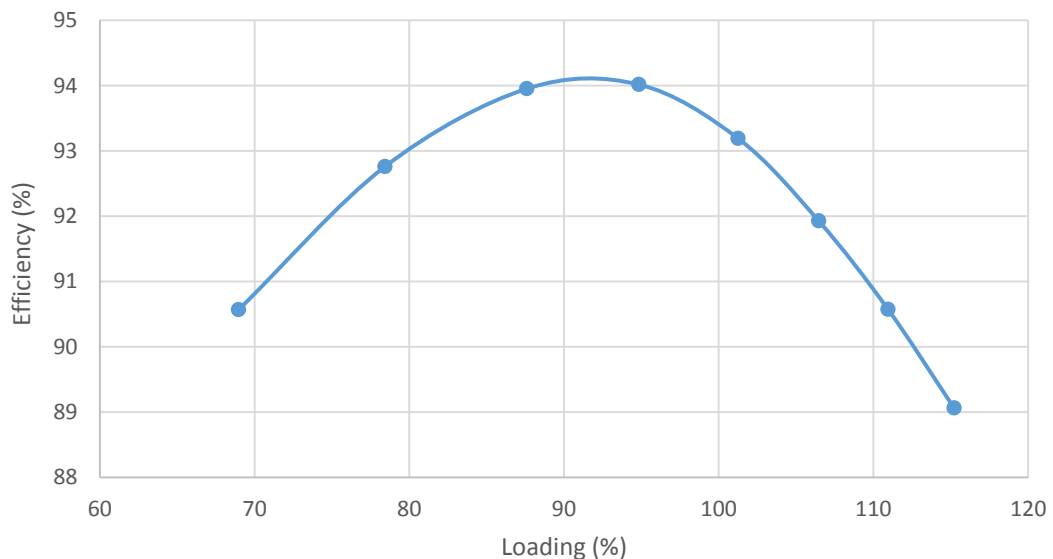


Figure 5.20: Loading- efficiency graphic (For 154 m head)

In Figure 5.21, for different head values, turbine power output versus guide vane efficiency curves are shown. The trend of the power output is same when the head value changes. As it is expected, increasing the head value, increases the turbine power output. Also rising the guide vane opening increasing the generated power as it rises the flow rate. Guide vane efficiency rises with higher guide vane openings and heads as expected.

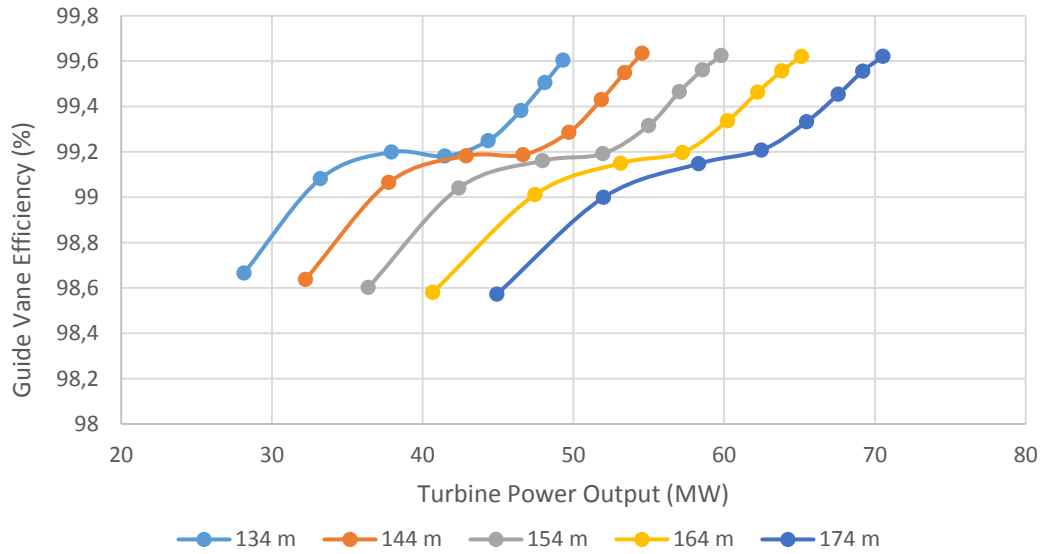


Figure 5.21: Guide vane efficiency versus turbine power output

The power production of the turbine changing with the flow rate is shown in Figure 5.22. The slope of the power curves decrease as the flow rate increases above the design head. Different head values show similar power trends with a changing flow rate.

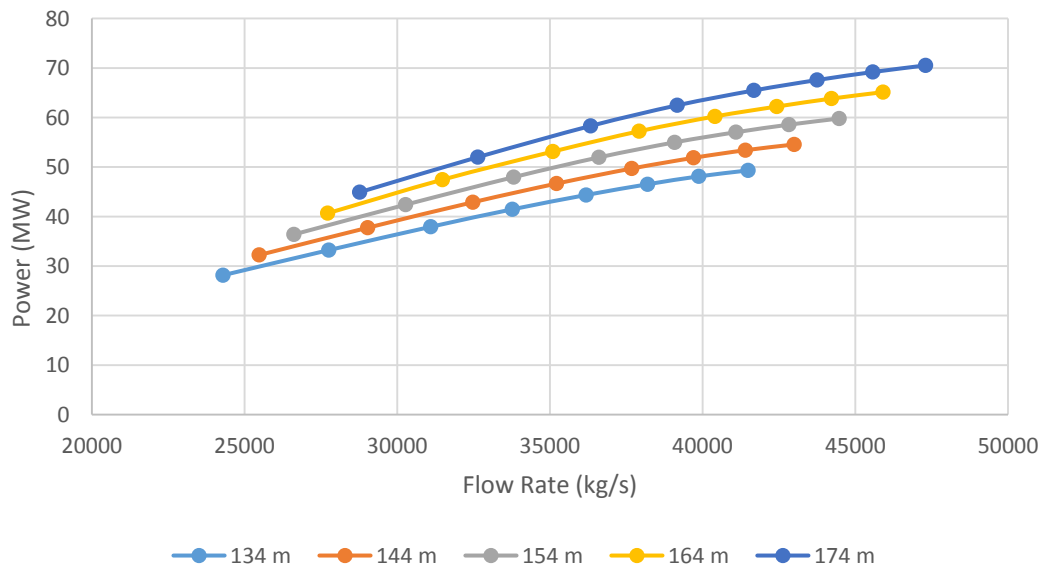


Figure 5.22: Flow rate versus turbine power output

In Figure 5.23, the efficiency curve is shown. Best efficiency point is captured with 35.035 m³/s flow rate with 94.07 % efficiency. At the operating point (or design point) efficiency is 93.27 % and flow rate is 38.6 m³/s. The closer design and best

efficiency point indicate that a good turbine design. In this turbine design point is close enough to the BEP point thus runner performance is good enough.

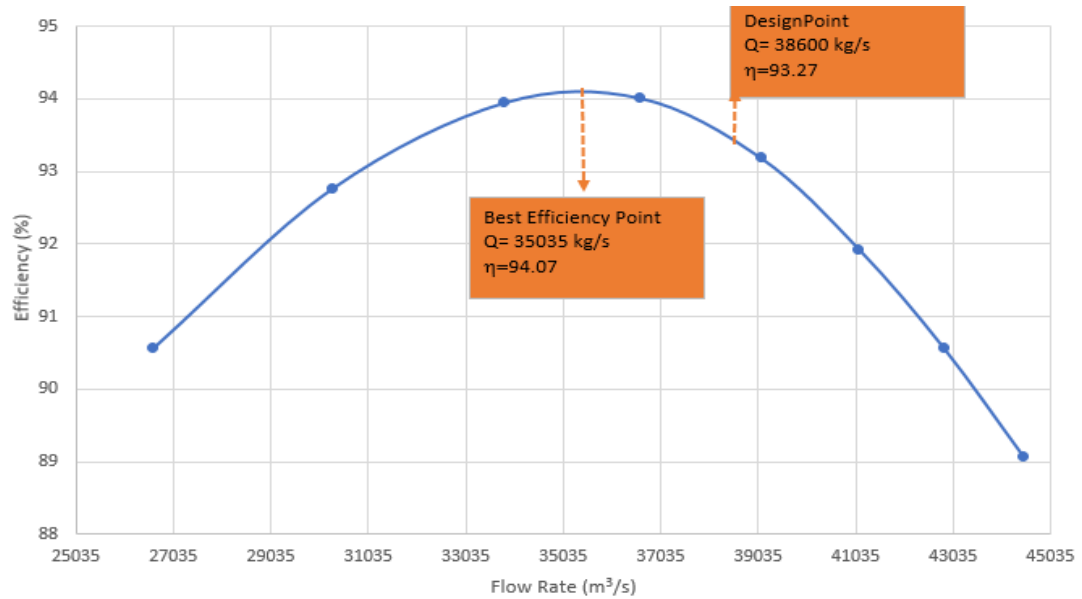


Figure 5.23: Turbine efficiency curve (H= 154 m)

5.4 LOSSES IN THE GEZENDE HPP AND COMPARISON OF THE CFD RESULTS WITH REAL DATA

Three types of loss of energy are observed in a turbine: hydraulic, mechanical and volumetric. The hydraulic losses are due to the flow of water through the turbine. Hydraulic losses comprise losses caused by friction and vorticity losses. Volumetric losses are the result of the leakage flow about the rotating turbine and due to the clearances. Mechanical losses are caused by friction with the rotation of the turbine, shaft, and runner. According to the Krivchenko [19], volumetric losses due to leakage flow and mechanical losses caused by the friction can assume as %1 to %2. Celic and Ondracka [74] revealed that labyrinth losses and disc friction losses has effect especially on part load operation with the maximum amount of 0.44 %. Feng [75] et al. used computational fluid dynamics technique to examine the disk friction loss and leakage. For different operating conditions they assumed leakage loss approximately 0.17 % of the total flow rate. Osterwalder et al, has also studied comprehensive experimental study to forecast leakage for each component of the turbine [76]. According to this study, leakage loss could be assumed as totally %2 all the turbine.

Each loss may be represented in terms of loss head. If h_v is the volumetric head loss due to leakage it can be calculated as it is given below:

$$h_v = \frac{q \times H}{Q} \quad (5.2)$$

Where q represents volumetric loss. Nominal flow rate of the Gezende HPP is 38.6 m³/s. With assuming 1% leakage, leakage volume flow rate can be assumed as

$$q = 0.386 \frac{\text{m}^3}{\text{s}} \quad (5.3)$$

Using the leakage flow rate, leakage power can be calculated as:

$$P_{\text{leakage}} = qgh_v \quad (5.4)$$

In Table 5.2, for 1-2% leakage flow assumption power of the Gezende HPP is calculated and compared with the field measurements made during commissioning of the plant. According to these when losses are neglected maximum relative error is observed as 2.133 %. With 2% leakage assumption relative errors are higher when it is compared with the 1% assumption. 1% leakage assumption is an agreeable assumption with 0.452 %, 0.107 %, and 1.948 % power, efficiency, and loss relative error, respectively. Also, from these results, it is seen that CFD results are consistent with field measurements.

Table 5-2: Performance comparison for CFD and field measurements

	Measurement	Leakage Free CFD results	Relative error (%)	%1 leakage assumption	Relative error (%)	%2 leakage assumption	Relative error (%)
Power (MW)	51.43	51.56	0.55	51.07	0.71	50.52	1.78
Efficiency (%)	0.94	0.94	0.86	0.93	1.17	0.92	2.23
Loss(m)	8.74	8.37	0.04	9.77	0.11	11.32	0.23

CHAPTER 6

ANALYSIS OF TRANSIENT HYDRAULIC FEATURES OF THE GEZENDE HPP

6.1 INTRODUCTION

In this part of the study, transient simulations have been conducted for the Gezende HPP to investigate the dynamic behavior of the flow. The simulations have been carried out at 5 different operating conditions, which are marked at by blue point on the hill chart.

It is important to understand the unsteady hydraulic features and pressure pulsations on the turbine for providing technical support for the rehabilitation process. Brief information about the stability and the coupled vibration of the hydropower house is obtained. The influence of rotor-stator interaction is investigated. The unsteady simulation results are also compared with the steady flow results.

Utilizing Fast Fourier Transform (FFT), pressure signals which are taken from the observation points on different locations in the turbine, spectral analysis is conducted. The obtained frequencies and magnitudes graphs shown that partial load operation condition has largest magnitude frequency in the draft tube. Insight of this information, flow inside the draft tube has been investigated in detail. Notably, it has been seen that flow behavior inside the cone has dramatically influenced the C_p and the full turbine efficiency.

6.2 THE METHODOLOGY OF THE TRANSIENT ANALYSIS

In this part of the study, transient simulations of the Gezende HPP have been carried out. By performing steady-state simulations; turbine performance, efficiency, pressure distribution, cavitation, hydraulic losses inside the components are measured. On the other hand; as the flow field inside the turbine is unsteady, transient phenomena inside the turbine-like von Karman vortices, draft tube swirl, cavitation regions can be investigated further with unsteady approach. According to the Custer et al. [65],

unsteady results are more consistent with experimental results when it is compared to the steady-state results. In the previous section, the hill chart of the Gezende is obtained for the steady-state conditions. Operation limits that are drawn with the blue line in the hill chart are obtained from the in-site measurements. Due to the complex flow, unsteady analysis is time-consuming, therefore simulating unsteady analysis for the whole operating range is not possible. For this purpose, unsteady analysis is conducted in five range-limit points, which are also shown in Figure 6.1.

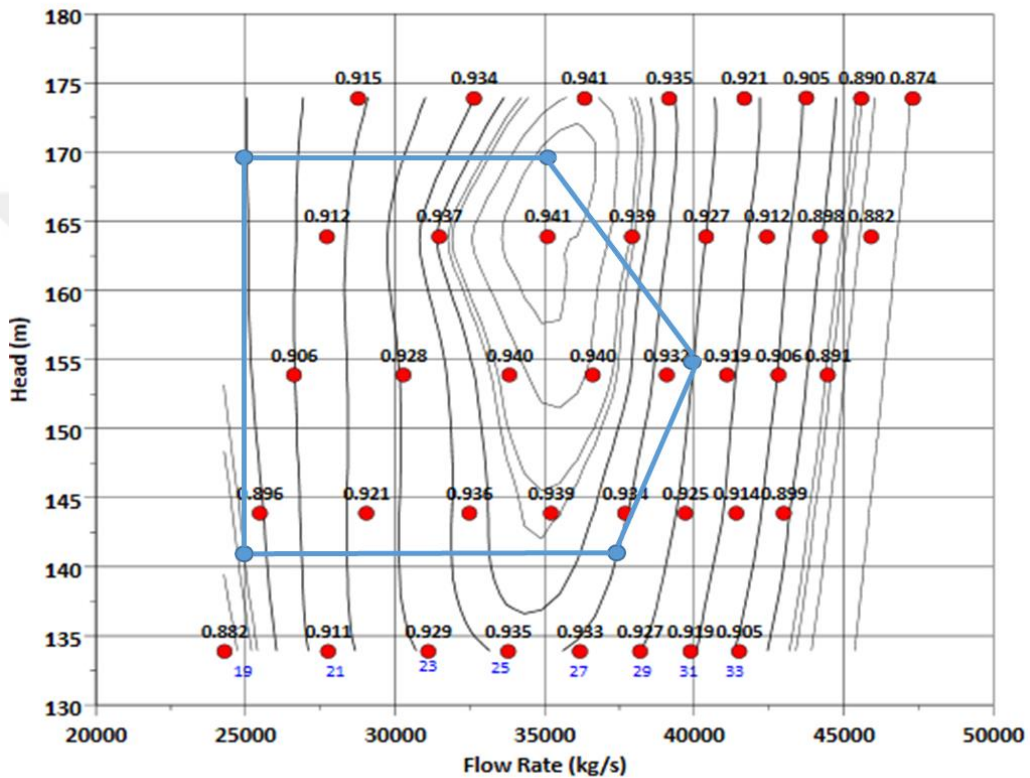


Figure 6.1: Operation range and selected simulation points (corners)

For the transient simulations, the time step has been defined as 0.001 s, which corresponds to the 2-degree rotation of the runner. A second-order backward Euler is used as a transient scheme with a high-resolution advection scheme. The maximum loop coefficient is taken as 3 as a turbulence model, k-epsilon is utilized. The time parameters of the transient simulations are given in Table 6.1.

Table 6-1: Time Variables

	Runner Rotation	
Time Step	0.001 s	2 degrees
Total Time	3.06 s	17 full rotations

As it is given in detail in cavitation section, Francis type turbines are exposed to five different cavitation types which are leading edge, traveling bubbles, draft tube, and inter blade vortex cavitation (Von-Karman vortices). Each type of cavitation can cause damages, noises, vibrations and even cracks. They can also cause a reduction in turbine efficiency and power output. For several HPPs, cavitation related problems and the offered solutions in the rehabilitation process are shown in Table 6.2.

Table 6-2: Problems identified in powerhouses together with specific reason
[Adopted from Ref 64]

Stations	Country	Problems	Locations	Reasons	Researcher	Year
Little Long	Canada	Crack	Stay vane	Karman Vortices	Wang	1956
Sayano Shushenskaya	Russia	Crack	Blade	Karman Vortices	Brekke	1983
Tamla	Pakistan	Crack	Draft Tube	Vortex Rope	Grein and Goede	1994
Xiaolangdi	China	Resonance fatigue	Runner	Karman Vortices	Fisher	2001
Dachshund	China	Crack	Blade	Karman Vortices	Yin and Shi	2001
G.M. Shrum	Canada	Crack	Runner	Inter-blade Vortices	Finnegan	2002
Gongzui	China	Noise	Channels	Inter-blade Vortices	Shi	2004
Three Gorges	China	Damage	Casing and Wicket Gates	Cavitation	Li Chen	2006

As several examples are given in Table 6-2, cavitation causes vibrations, noises, a reduction in efficiency and instability on all of flow path in turbine. Excessive vibration is the most common result of the cavitation for hydroelectric power plants. Engineers who works in Gezende Powerhouse, states that turbine is exposed to excessive vibration. With unsteady analysis, the reason for this vibration may be investigated.

6.3 EVALUATION OF TRANSIENT HYDRAULIC FEATURES IN FLUID DOMAIN

To analyze the time and frequency features of the pressure fluctuations 21 measuring points are located to several positions. 7-points located in the spiral case, stay vanes and guide vanes to observe von-Karman vortices. 4-point pairs are located to runner blade to examine the inter-blade vortices, traveling bubbles and leading-edge cavitation. Last 6 points are at the inside of the draft tube to observe draft tube swirl. Each observation points are shown in the Figure 6.2 to 6.4.

Where.

Sc: Spiral Case

Gv: Guide Vane

Ps: Pressure Side of the runner blade

Ss: Suction Side of the runner blade

Dt: Draft Tube

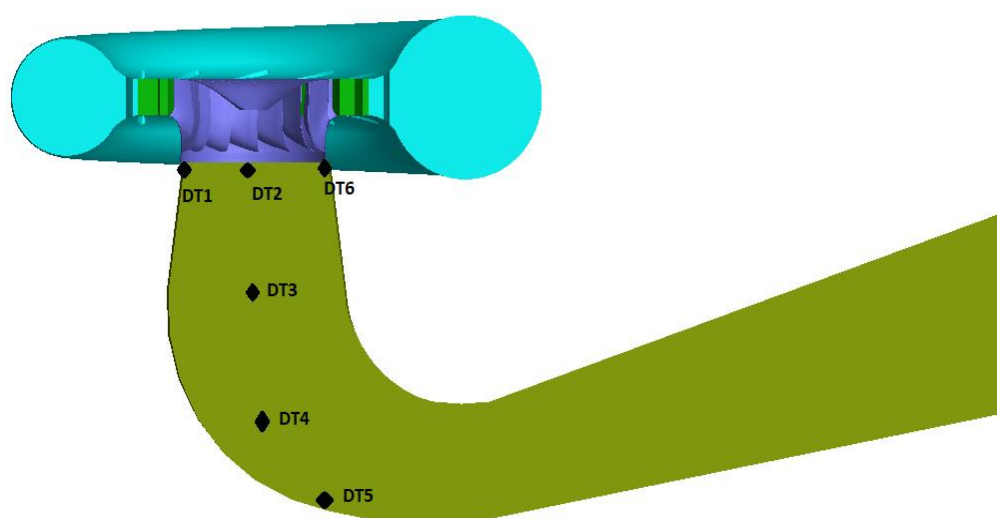


Figure 6.2: Observation points in the Draft tube

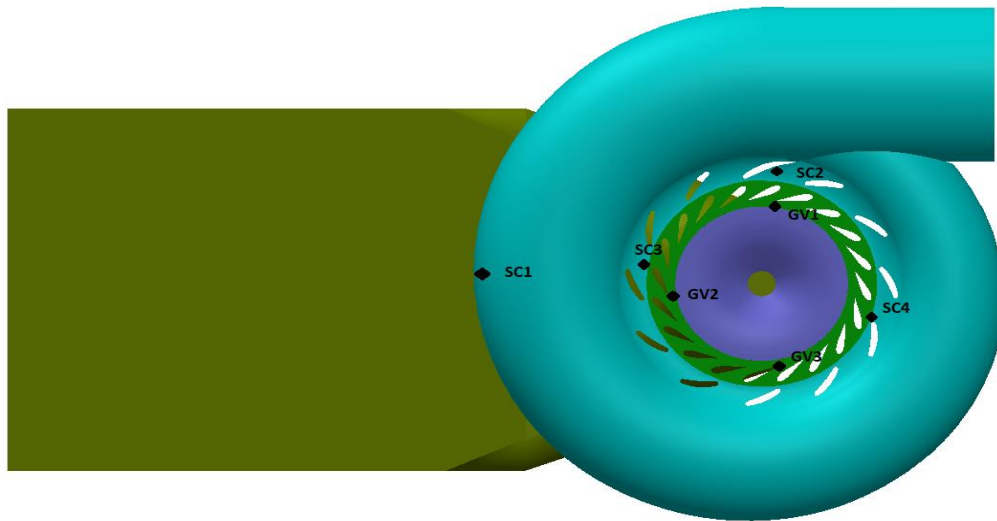


Figure 6.3: Observation points in the Spiral Case

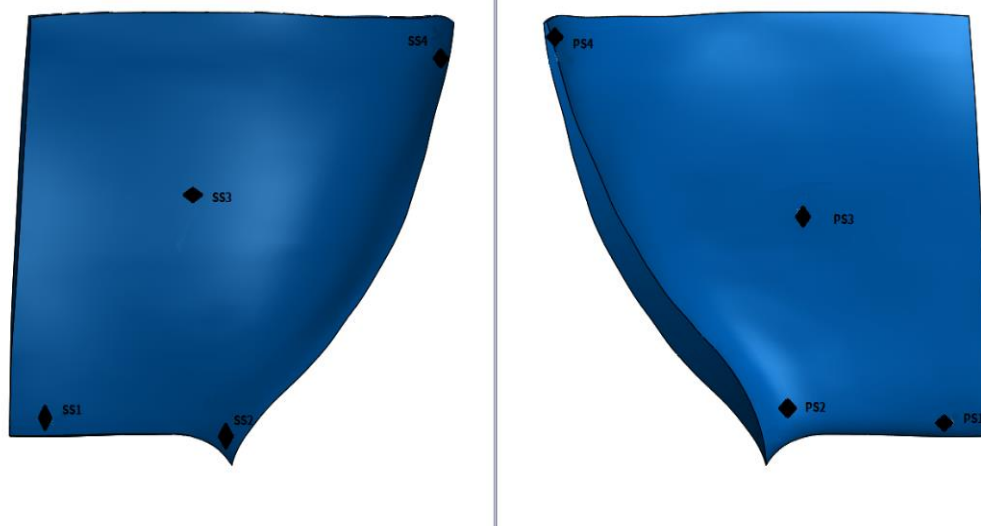


Figure 6.4: Observation points in the blade, (Left) suction side (Right) Pressure side

As the pressure levels have a significant impact on the cavitation for each time step and at each location pressure signals are recorded. If the pressure fluctuations are observed in the flow field, it means that the fluctuation point exposes to the cavitation.

Efficiency and torque fluctuations are shown in Figure 6.5 for the nominal conditions of the Gezende HPP (154 m and 25-degree opening). Due to the obtained results, after 1-second periodic fluctuations are observed in the efficiency and torque value. Therefore, while evaluating the unsteady state analysis results first one second is cropped.

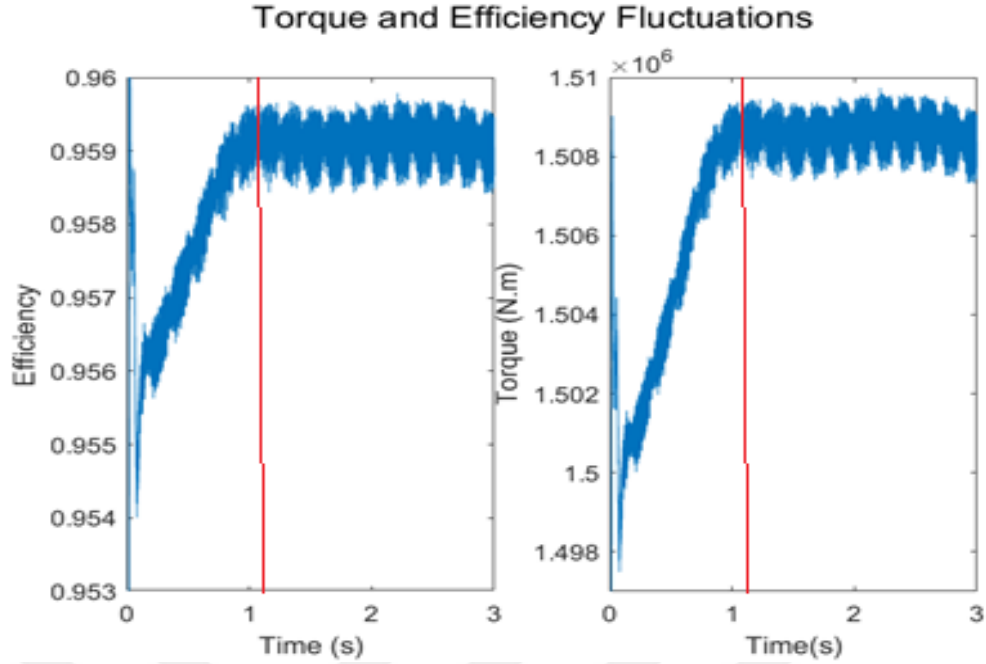


Figure 6.5: Torque and Efficiency fluctuations with respect to time.

By using the In-house MATLAB codes, pressure signals are non-dimensionalized according to the IEC 60193 Equation 6.1. By using non-dimensionalized pressure values, pressure fluctuations on the time domain of the observation points are transformed into the frequency domain with the Fast Fourier Transform. In the FFT graphics, y and x-axis represents the magnitude of the f_n and X_{rms} , respectively.

$$PE = \frac{p-p_{aver}}{\rho g H} \quad (6.1)$$

$$fn = \frac{f}{n} \quad (6.2)$$

$$X_{rms} = \sqrt{\frac{\sum_1^N X_n^2}{N}} \quad (6.3)$$

With FFT to pressure signals, the modes are detected. All of the mode's signals to flow disorders or instabilities inside the component where the point is located. Those phenomena can be a vortex structure inside the channels or between the runner blades, cavitation swirl in the draft tube, or a simple rotation effect of the runner.

In Table 6-3, the passing frequencies of the blades are shown. These frequencies or multiples (harmonic frequencies) are expected to be seen after the analyzes as dominant frequencies. Where n is the rotational frequency of the runner.

Table 6-3: Passing Frequencies

Passing Frequency	Passing Frequency	Passing Frequency
Stay Vane	Guide Vane	Runner
12xn	20xn	13xn

6.3.1 Transient Hydraulic Features in Fluid Domain

For each of the points that are in the various locations of the turbine, the pressure distribution is obtained, and FFT is performed for each location. With 3D plotting, the frequency and magnitude of the pressure signal are depicted. In the plots, the y-axis denotes the magnitude of the pressure fluctuation, the x-axis represents frequency, and the z-axis represents power as a nondimensionalized parameter with the nominal power of the turbine. Results of the spectral analyses have been combined according to the location of the observation point. Therefore, frequencies and magnitude variation could be observed properly and easily depending on power. The graphs are given in Figure 6-6 to 6-10.

6.3.1.1 Hydraulic Features of The Flow Field In The Spiral Case

For different observation points at the spiral case, FFT graphics are given in Figure 6.6. The amplitude of the frequency is quite small. Dominant frequencies except for SC₁ observation point can be seen at the 13 f/n which means passing frequency of the runner.

The low-frequency component of the signal at the SC₁ observation point can be explained with the draft tube swirl affect. As the spiral case is too far from the draft tube magnitude of the frequency is small and in the range of 10^{-3} and 10^{-4} . Through point SC₂ to SC₄, magnitude of the runner passing frequency increases as the distance between the runner and the data point decreases.

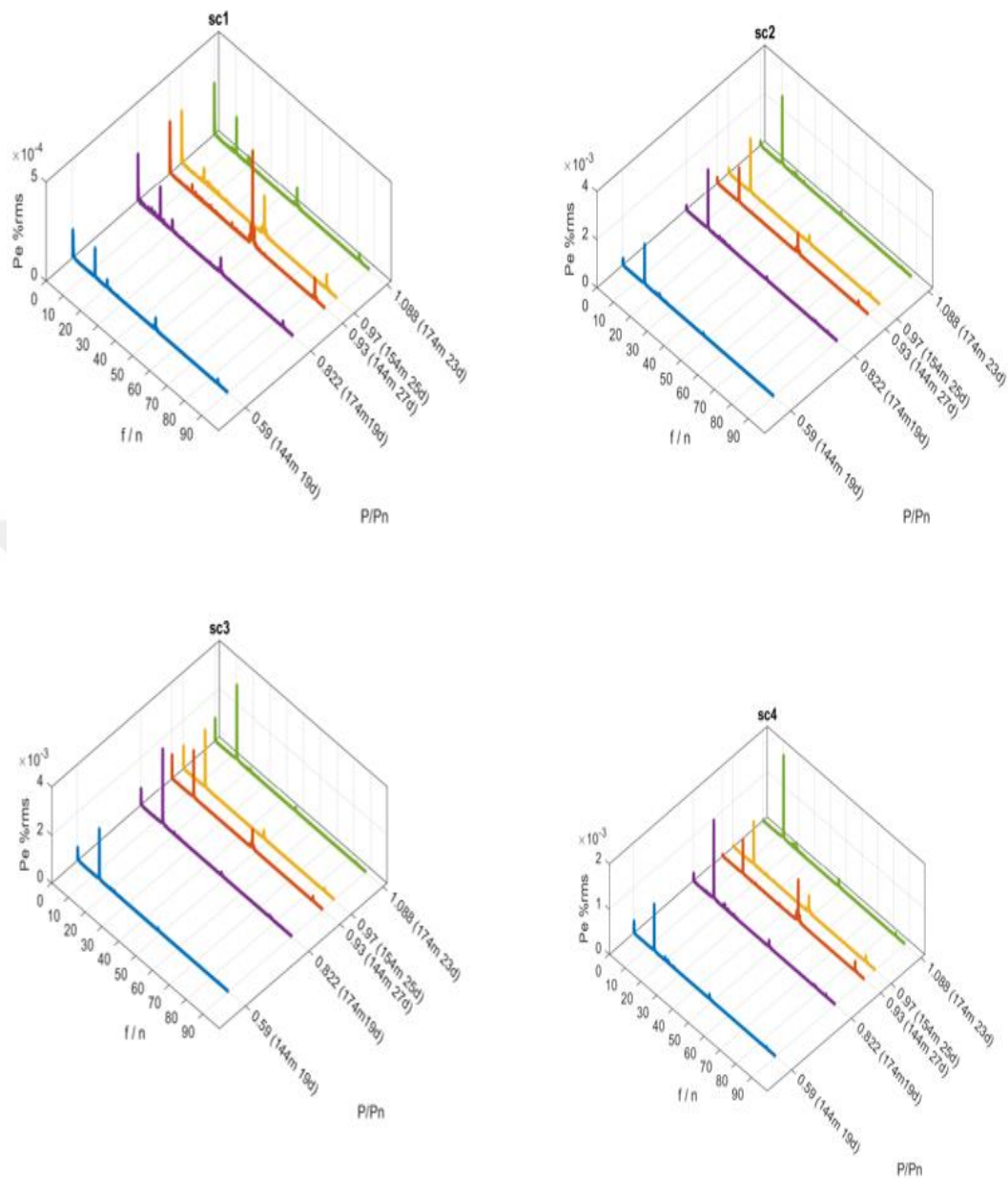


Figure 6.6: FFT analysis for spiral casing (a) SC1 (b) SC2 (c) SC3 (d)SC4

6.3.1.2 Hydraulic Features of The Flow Field in The Guide Vane

FFT graphics of guide vane points are shown in Figure 6.7. The dominant frequencies are equal to 13 f/n which is the runner rotation frequency. The magnitude of the passing frequency of the runner nearly 100 times greater than SC domain in the guide vane. The two greatest amplitudes in the graph, green and

purple plots, can be seen at the 174m head operation conditions. It means pressure fluctuations are increasing with the inlet pressure.

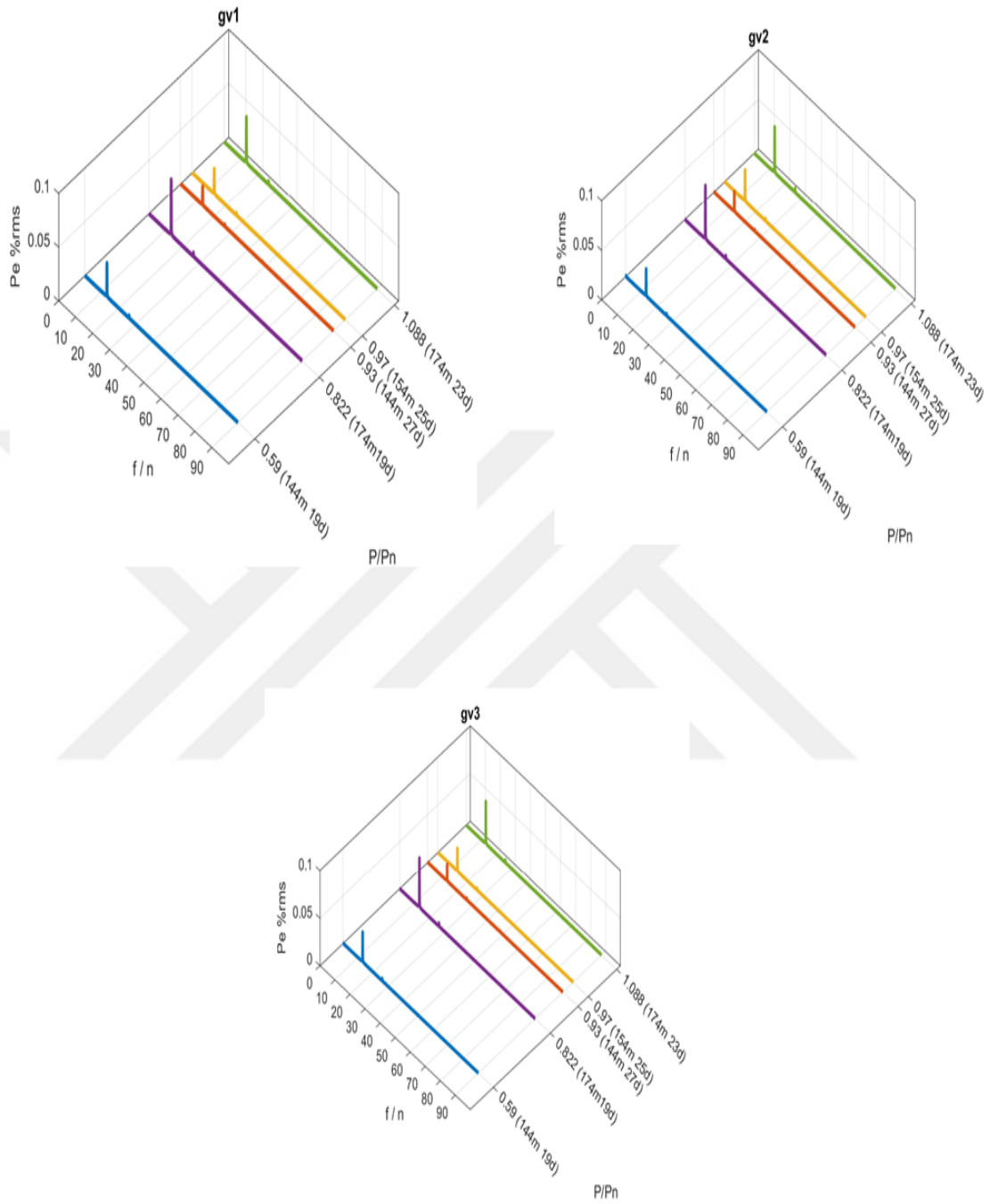


Figure 6.7: FFT analysis for guide vane (a) GV1 (b) GV2 (c) GV3

6.3.1.3 Hydraulic Features of The Flow Field in The Runner

The runner has 2 main frequencies as approximately $1 f/n$ and $20 f/n$ as shown in Figure 6.8. The $20 f/n$ frequency represents guide vane passing frequency. IEC 60193 [31], The low frequency occurs typically between 0.2 to 0.3 times the runner rotational frequency and low frequency indicates to draft tube swirl. For Gezende HPP, runner rotational frequency is 5.55 Hz, and low-frequency values are calculated as 1.11 and 1.66 Hz. into Figure 5.55, low frequency values are consistent with the simulation values. Therefore, it means that there is a formation of draft tube swirl and the effect of this swirl is also observed in the runner.

When SS4 and PS4 are examined, fluctuations are observed in the flow fields which indicates to travelling bubbles in the trailing edge of the runner. Escaler et al. [34] stated that the magnitude of those frequencies is increasing with the rise of the mass flow rate. The same result is also obtained for the Gezende runner.

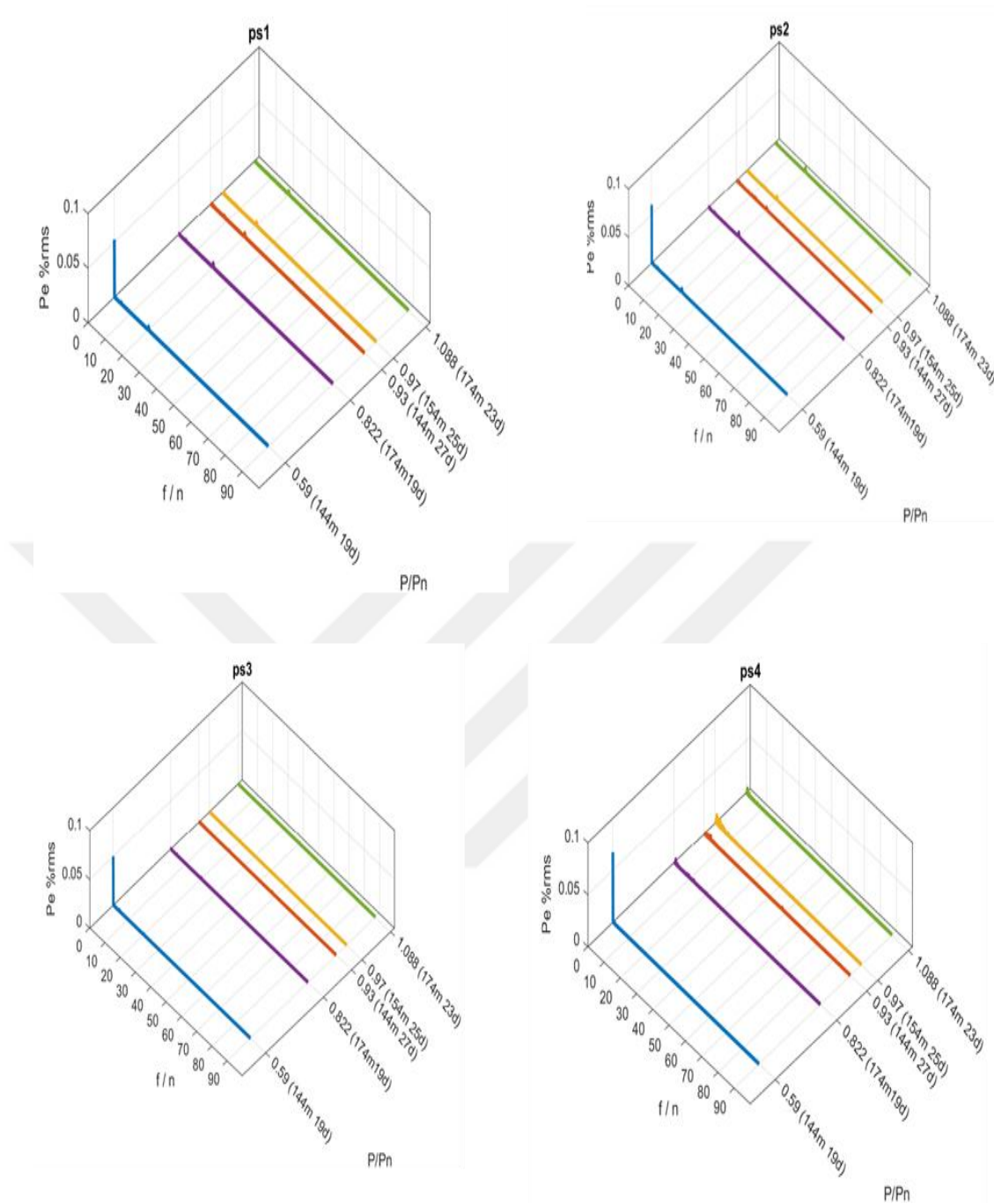


Figure 6.8 : FFT analysis for runner pressure side (a) PS1 (b) PS2 (c) PS3 (d) PS4

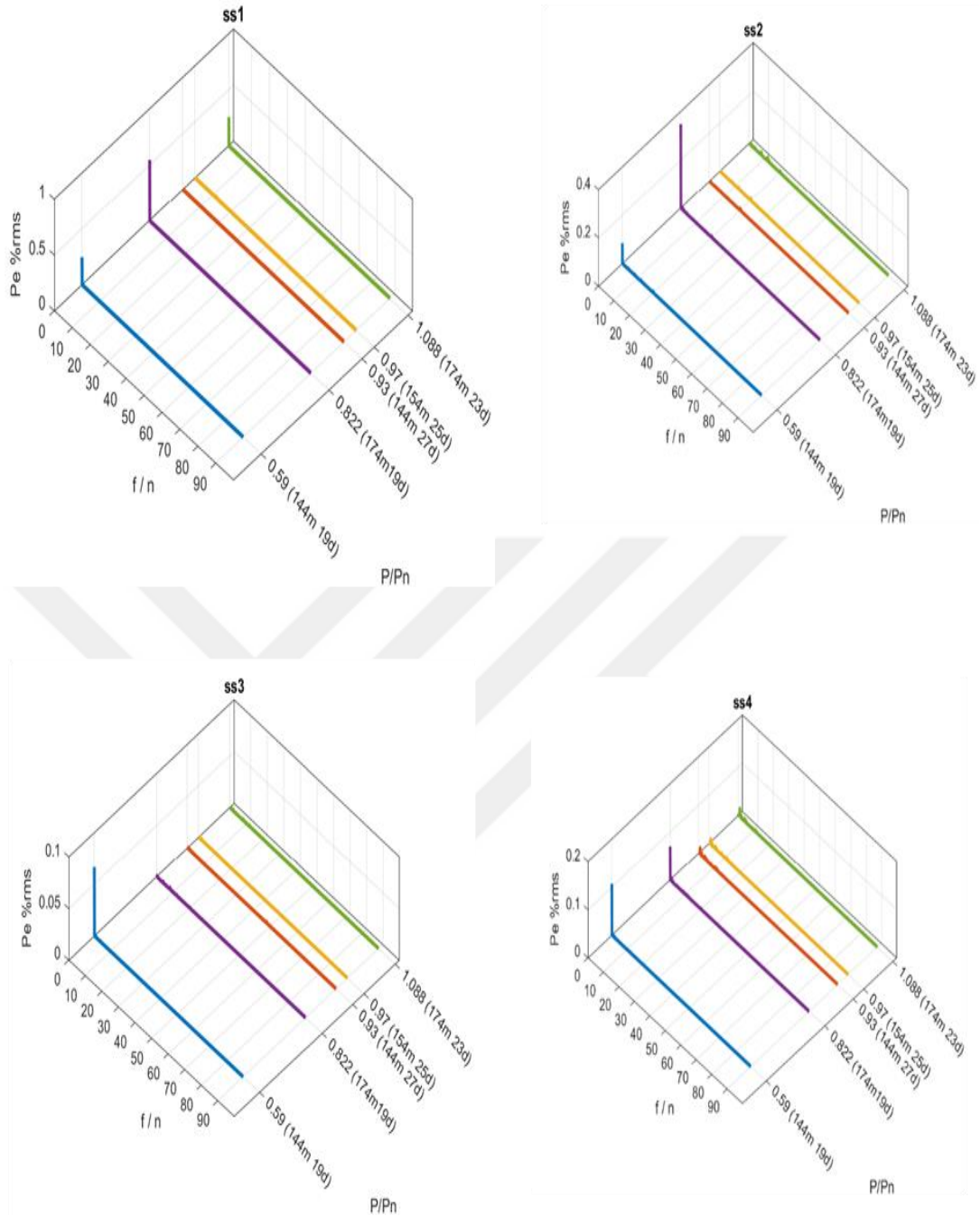
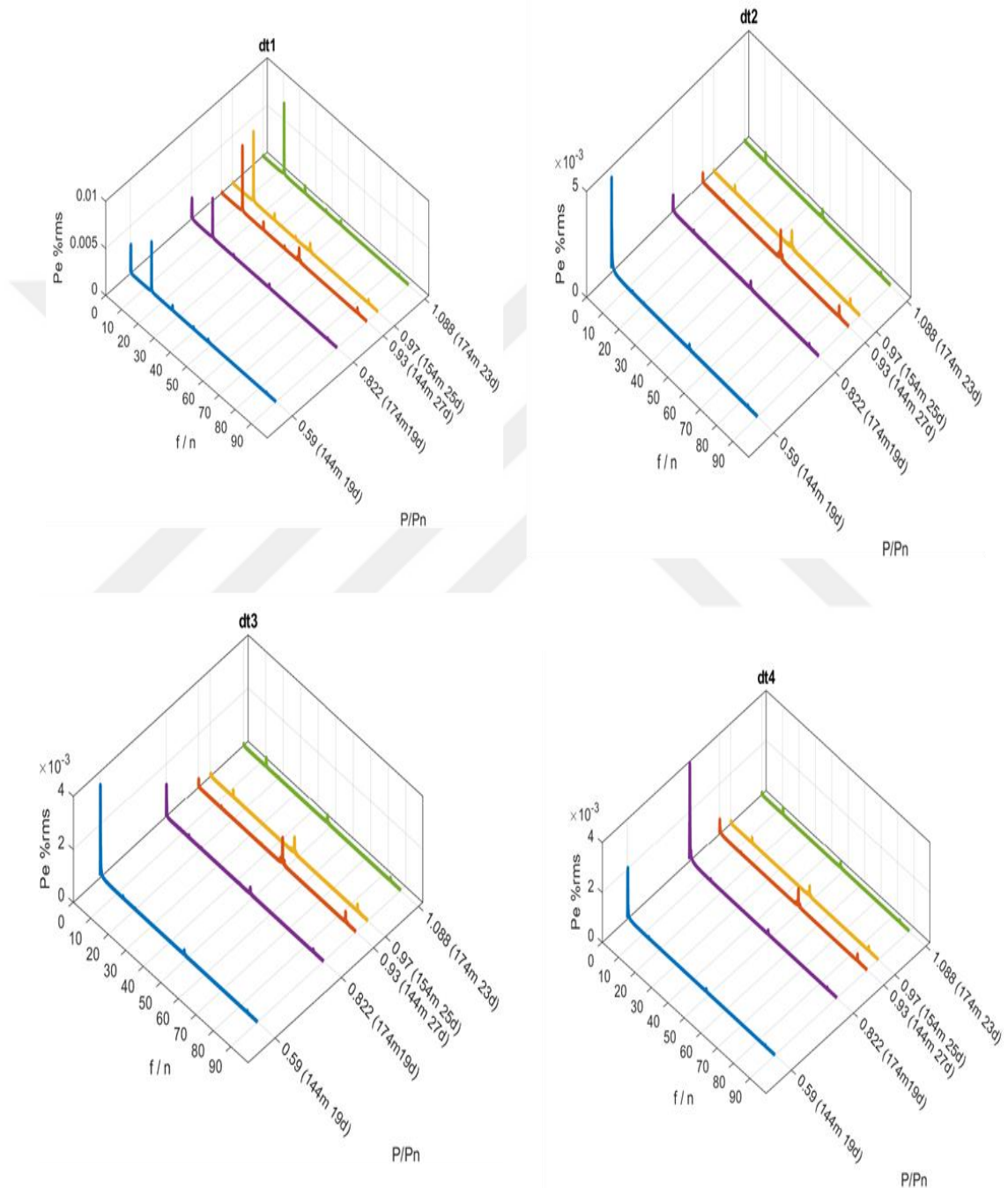


Figure 6.9: FFT analysis for runner suction side (a) SS1 (b) SS2 (c) SS3 (d) SS4

6.3.1.4 Hydraulic Features of The Flow Field in The Draft Tube

Many studies in the literature state that draft tube swirl frequency equals to 0.2-0.3 times of the runner rotational frequency. The vortex rope volume is a function of the Thoma number of the plant and loading condition. In Figure 6.10, the point DT2 which is located below the runner cone, dominant frequency with the highest amplitude is obtained at 144 m head and 19° guide vane opening (partial load). The

observations point at DT1 and DT6 which are located to draft tube walls, runner passing frequency can be seen prominently as dominant frequency. At DT3 and DT4, located inside to the elbow, the draft tube swirl effect is decreasing gradually. This is likely due to the shear layer between the forward and reversed streams in the elbow segment [18].



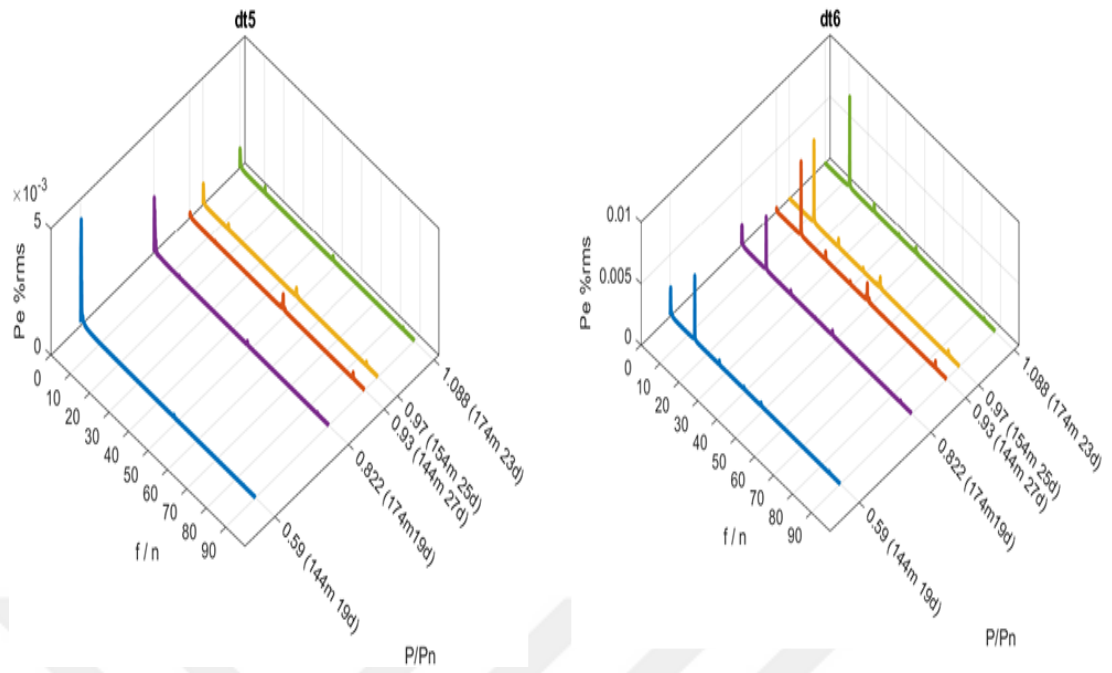


Figure 6.10: FFT analysis for draft tube (a) dt1 (b) dt2 (c) dt3 (d) dt4 (e)dt5 (f) dt6

CHAPTER 7

DETAILED EXAMINATION OF PRESSURE PULSATION AND UNSTEADY FLOW CHARACTERISTICS IN THE DRAFT TUBE

FFT results, that are computed at several locations inside the turbine, indicate that the draft tube vortex structure is formed. Therefore, detailed examination for pressure pulsation and unsteady flow characteristics in the draft tube is investigated in detail in this part of the study.

7.1 PRESSURE DISTRIBUTION AND SWIRL FORMATION IN THE DRAFT TUBE

The flow characteristic inside the draft tube directly affects the efficiency of the turbine. Also, it is the primary source of the vibration issues of the HPP. Due to the residual circumferential velocity of the outlet of the runner [31], draft tube vortex forms at the runner outlet and reaches the elbow of the draft tube. In this section, this phenomenon is investigated using CFD tools.

Draft tube pressure distributions are given for each operation condition in Figure 6.10. The distance between planes is defined as $Z=0.5\text{m}$, $Z=1\text{m}$, $Z=2\text{m}$, $Z=3\text{m}$, and $Z=4\text{m}$.

At different operating conditions, the common behavior of the simulation results is:

- 1- Draft tube swirl is formed
- 2- The lowest pressure is observed nearly at the centerline of the runner.
- 3- For 20 C^0 , cavitation is not observed in the draft tube.

In the Figure 7.1 for 144 m head and 19° guide vane opening pressure contours and vortex visualization is given. To visualize the vortex structure inside the draft tube Q-criteria method is used. For the sake of consistency, the iso-surfaces of the Q-criteria equal to 0.11 were displayed in all cases. When it is compared with other cases,

minimum pressure zone is observed in this case which is approximately 37kPa. This value is higher than vapour pressure at 20°C, so it can be said that there is no cavitation. Also, the biggest vortex volume is detected in this loading situation.

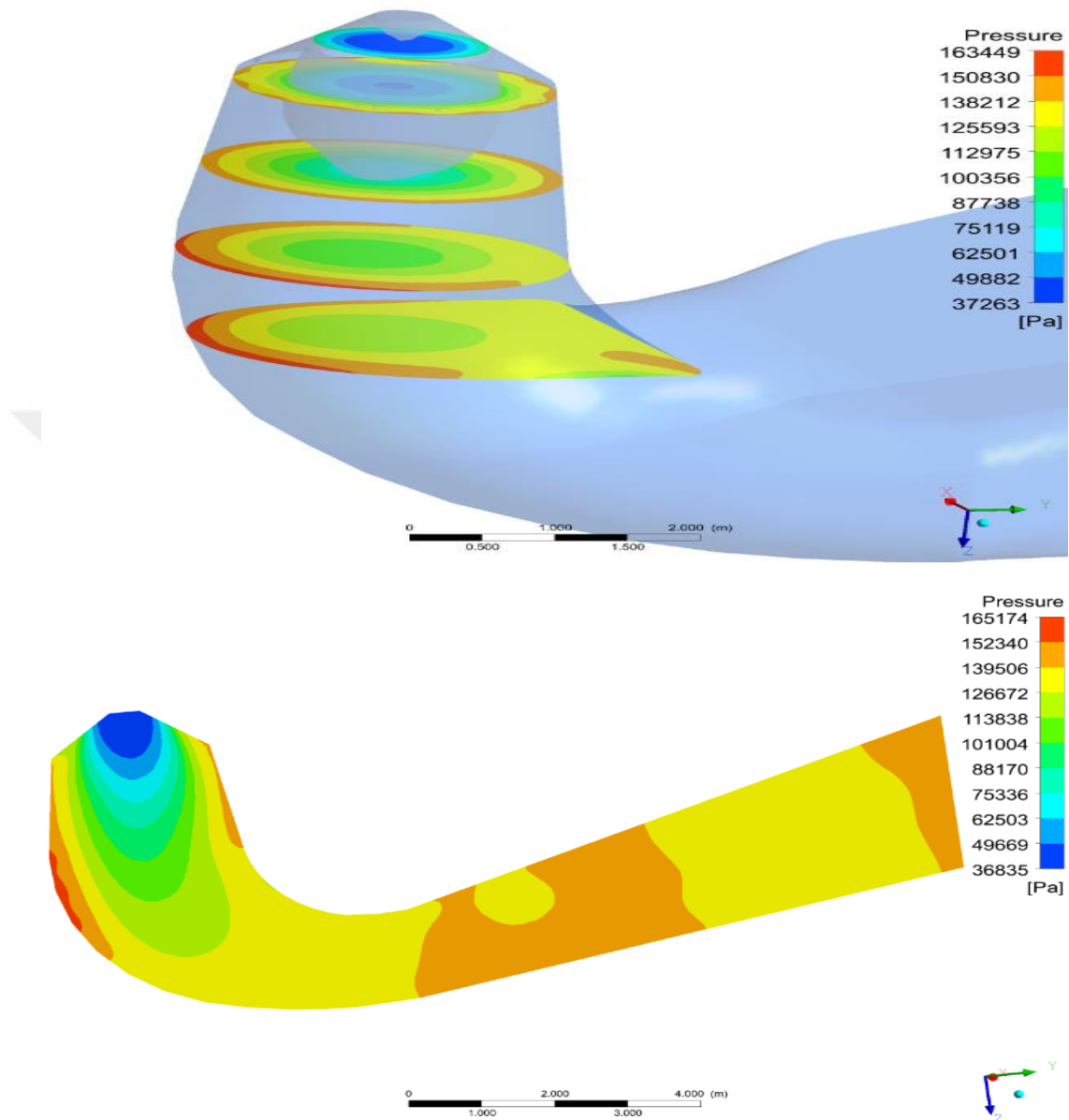


Figure 7.1: Draft tube pressure distribution and vortex structure for 144 m head and 19° guide vane

In Figure 7.2, for the 144-meter head with 27° guide vane opening pressure distribution and vortex structure are given. This figure indicates that there is no cavitation is observed for this loading.

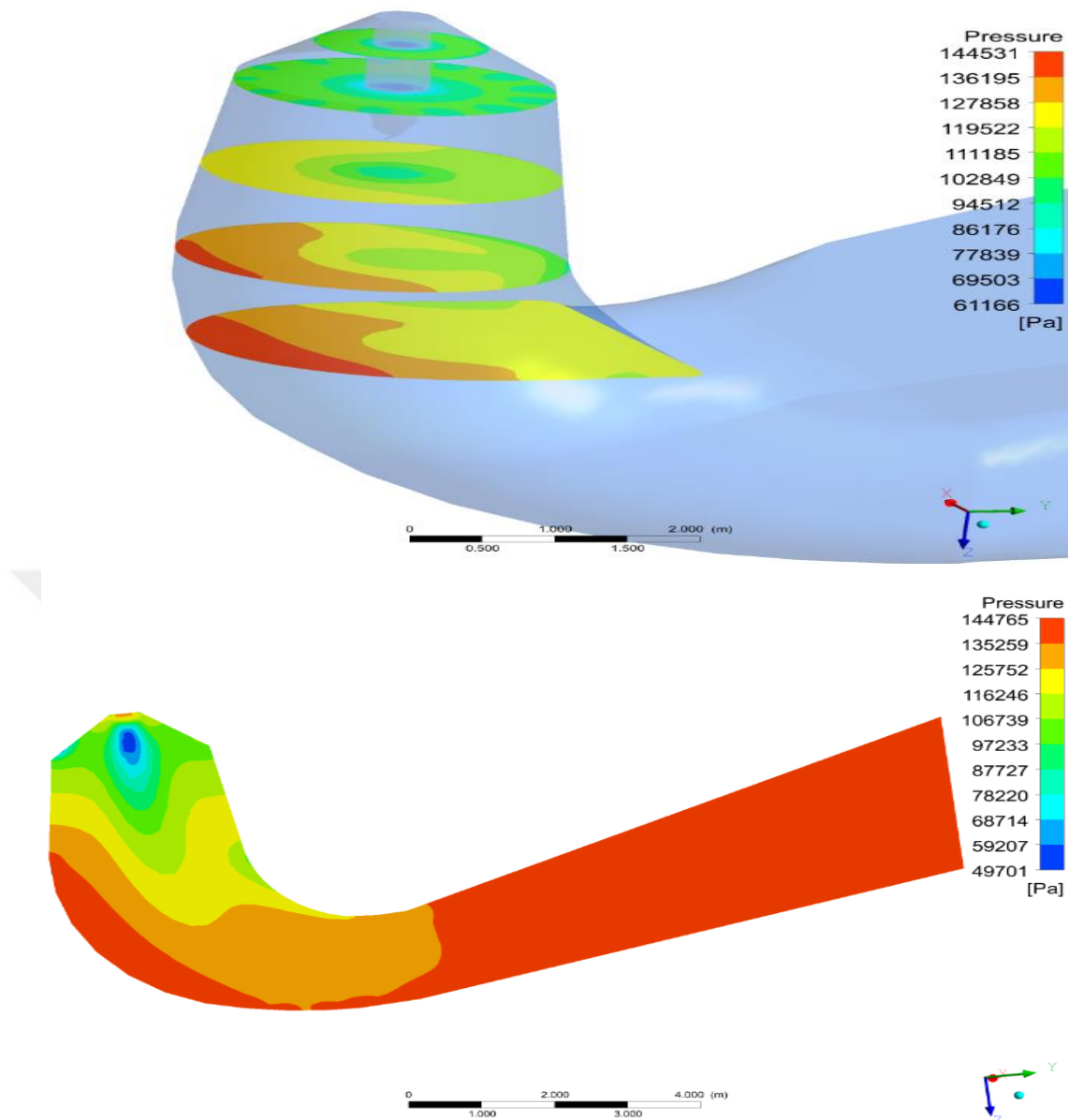


Figure 7.2: Draft tube pressure distribution and vortex structure for 144 m head and 27° guide vane opening

In Figure 7.3, for the 154-meter head with 25° guide vane opening pressure distribution and vortex structure are given. This point is the nominal operating condition for this turbine. The smallest vortex structure is obtained in this loading situation because this loading is the nearest condition to the design flow rate and head value. This is also evidence that in the full loading situation vortex is minimized in the draft tube.

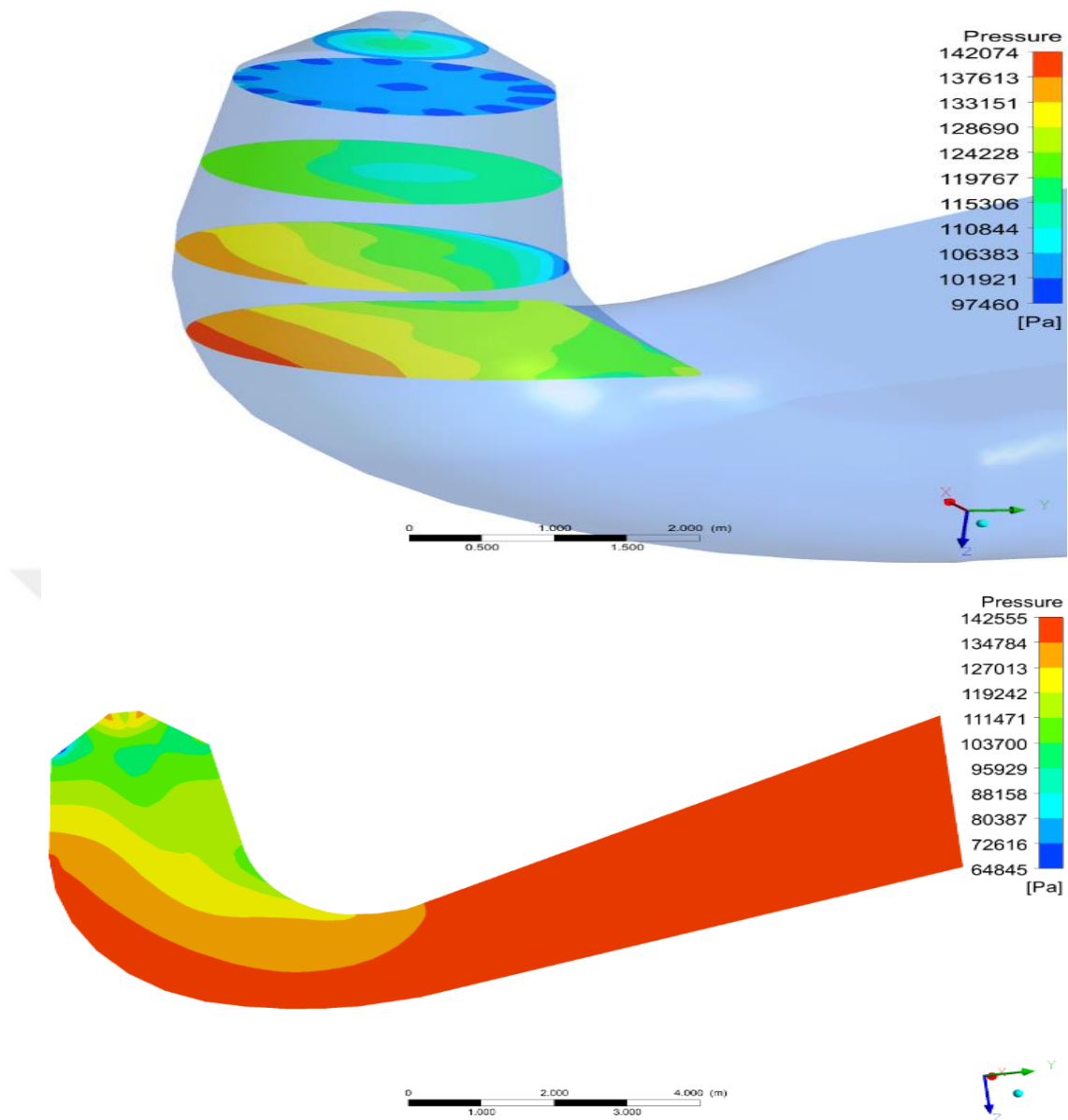


Figure 7.3: Draft tube pressure distribution and vortex structure for 154 m head and 25° guide vane opening

In Figure 7.4, for the 174-meter head with 19° guide vane opening pressure distribution and vortex structure are given. In this scenario, which has the highest head value, efficiency value decreases to 0.916.

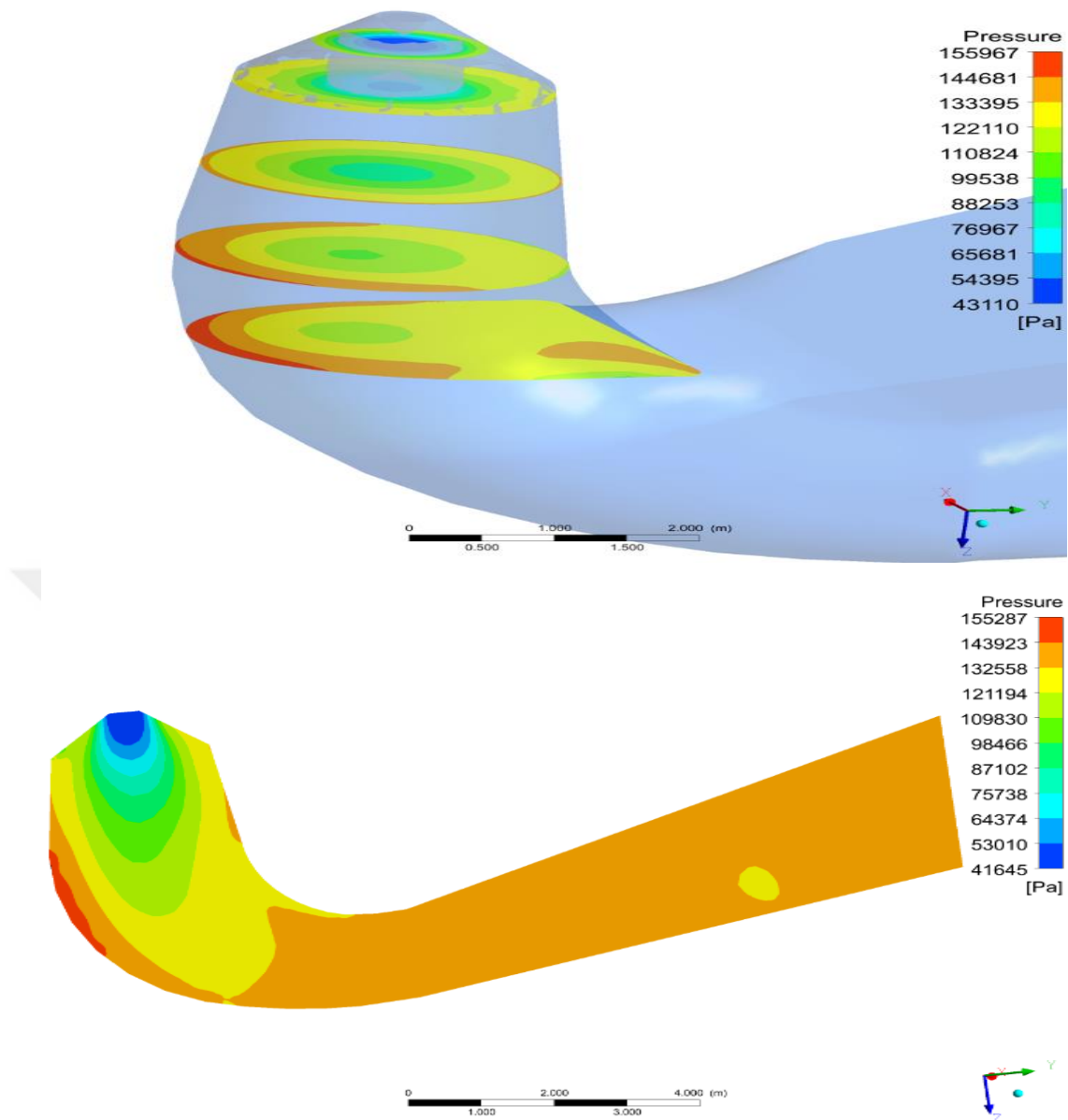


Figure 7.4: Draft tube pressure distribution and vortex structure for 174 m head and 19° guide vane opening

In the Figure 7.5, for 174-meters head with 23° guide vane opening pressure distribution and vortex structure are given.

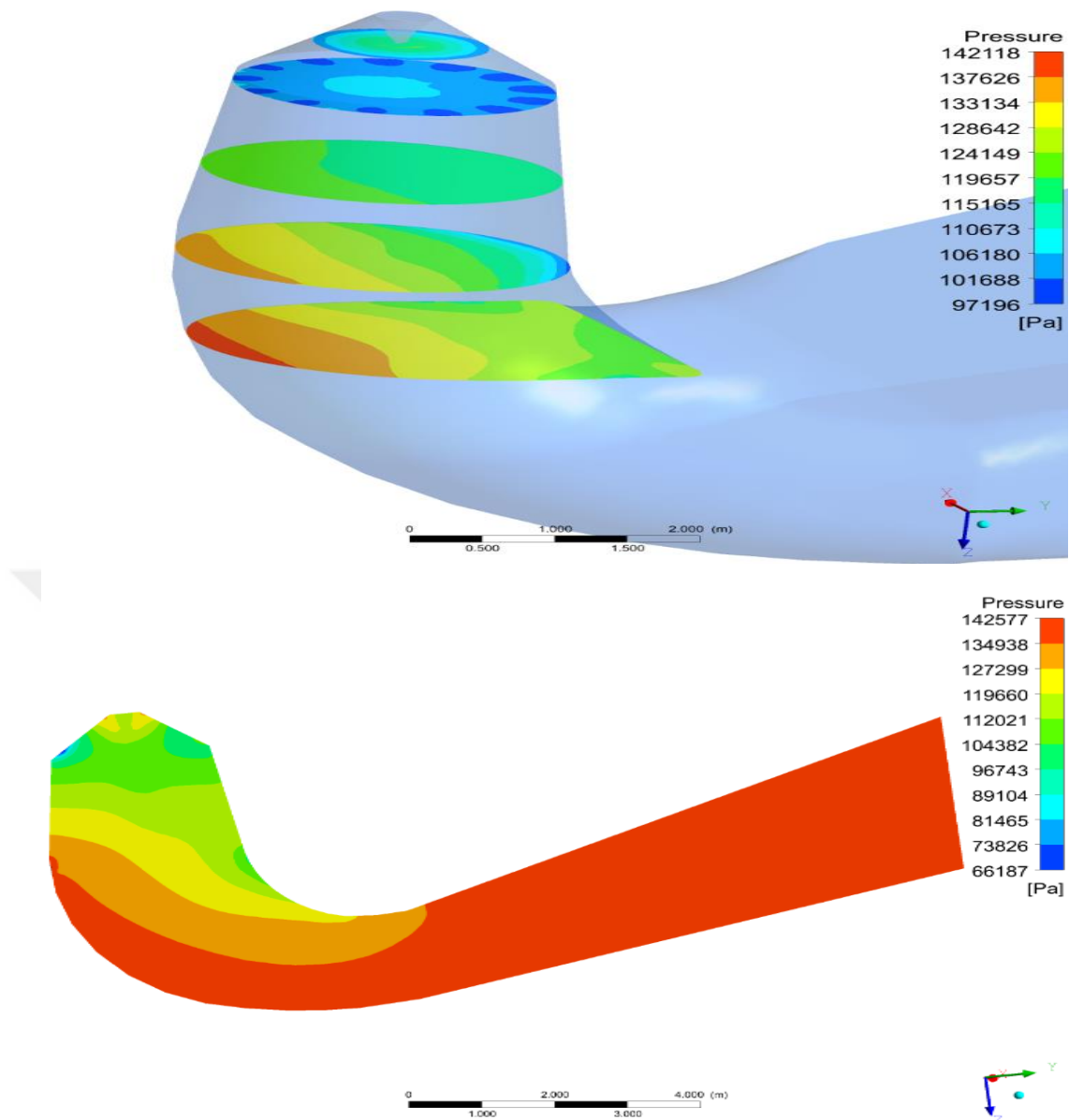


Figure 7.5: Draft tube pressure distribution and vortex structure for 174 m head and 23° guide vane opening

7.2 AXIAL AND CIRCUMFERENTIAL VELOCITY DISTRIBUTION

Axial and circumferential velocity distributions have been investigated to provide a better understanding of the flow physics inside the draft tube. 4 lines are defined in the draft tube cone to calculate the axial and circumferential velocity distribution at different locations, as it is depicted in Figure 7.6.

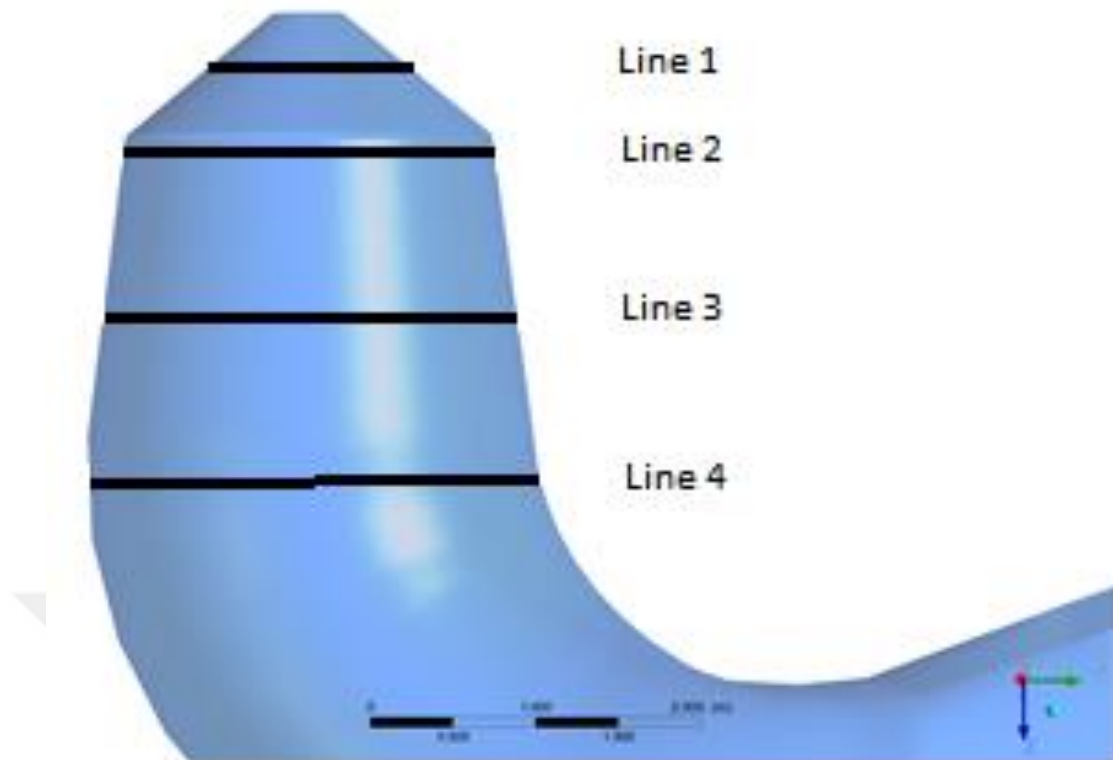


Figure 7.6: Defined lines on the draft tube cone

For all five cases, velocity distribution in the radial direction on each line, are given in Figure 7.7 to 7.10. The axial and circumferential velocity distribution is obtained symmetrically on the rotation axis.

According to Figure 7.7, axial velocities for each case has the lowest velocity at the center of the draft tube cone. While in all operating conditions, axial value is minimized in the rotation axis, 144-meters head, and 27° guide vane opening condition (Red plot) axial velocity reaches its maximum value in the rotation axis. This condition is the nearest scenario that the flow rate is almost the same as the operating flow rate value. For all lines, axial velocities are increasing as getting closer to the wall of the draft tube except 144m27d operation. For the 144m19d and 174m19d partial load operation, which has 25.23 m³/s flow rate and 28.48 m³/s respectively (purple and blue plots), as seen on the graph amplitude of the vectors are larger compared to others. This is also common behavior for all lines.

For the partial load, 144m19d and 174m19d (purple and blue plots), axial velocity on all lines, are negative on the closer area on the centerline of the runner. It means that there is flow reversal. According to all axial velocity graphs, axial flow

distribution on all lines is getting uniform with the axial direction excluding partial load operations.

Circumferential velocity reaches its minimum value at the centerline of the runner for all lines and for all operating conditions due to characteristics of the vortex flow. The positive sign of the circumferential velocity means that the vortex rotates the counterclockwise direction which is the opposite rotation direction of the runner. In the partial loads, 174m19d and 144m19d (blue and purple plots), vortex rotates counterclockwise for all axial levels. In line 1, according to Figure 7.7, the sign of the axial velocity changes in $\pm 0.2\text{m}$ distance from center. In this distance range, at some points, circumferential velocity is equal to zero which means there are vortices at this location.

Maximum circumferential velocity is obtained for partial loads on all lines. While circumferential velocity is decreasing close to the draft tube wall for all operation conditions, at the 144m19d (blue plot) operation condition, circumferential velocity reaches its maximum value. The high value of the circumferential velocity in the close fields of the draft tube walls is one of the reasons for the vibration [44].

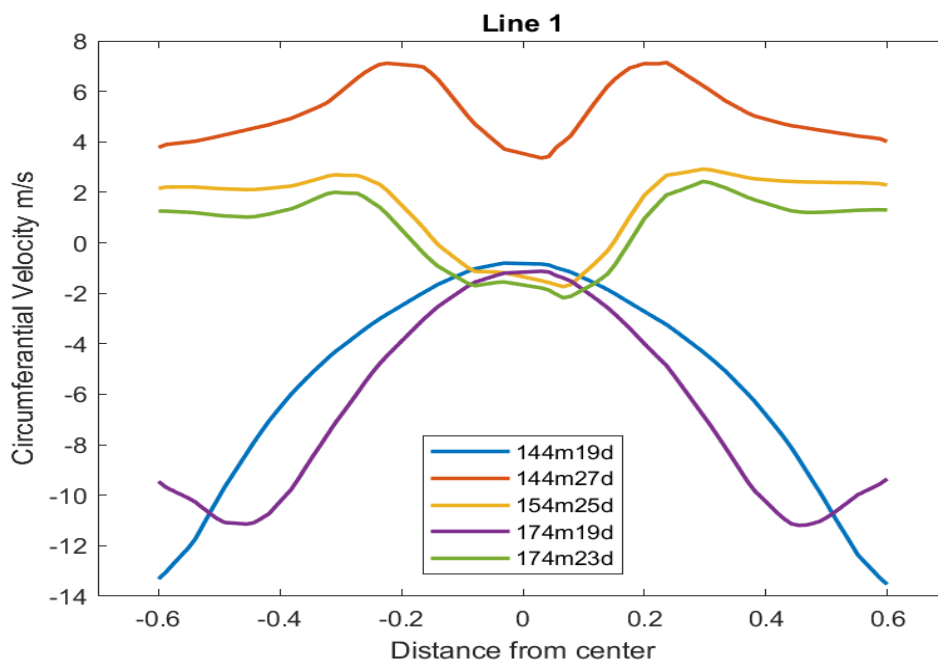
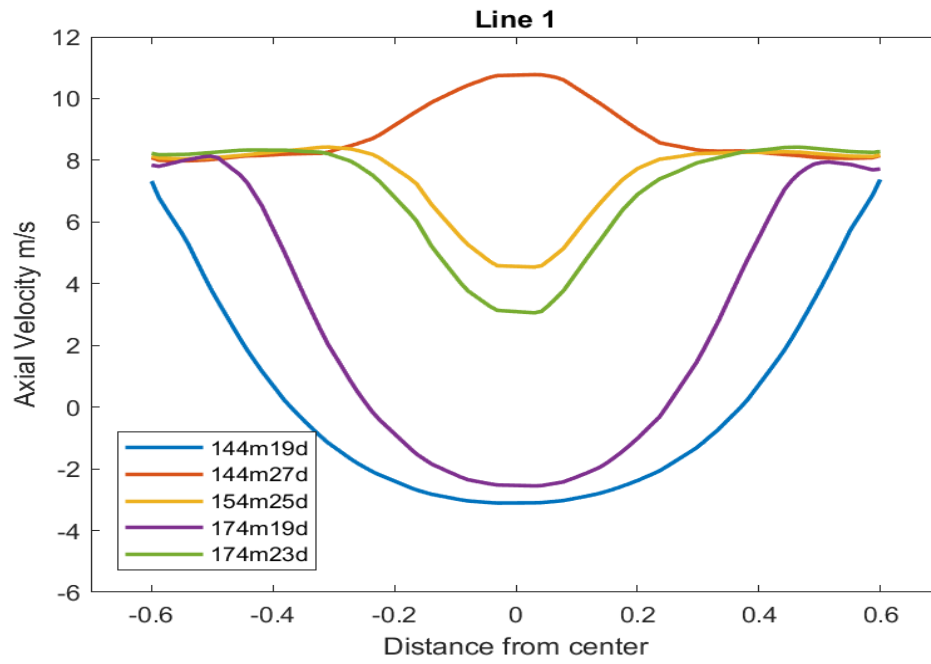


Figure 7.7: Axial and Circumferential Velocity Distribution on Line 1

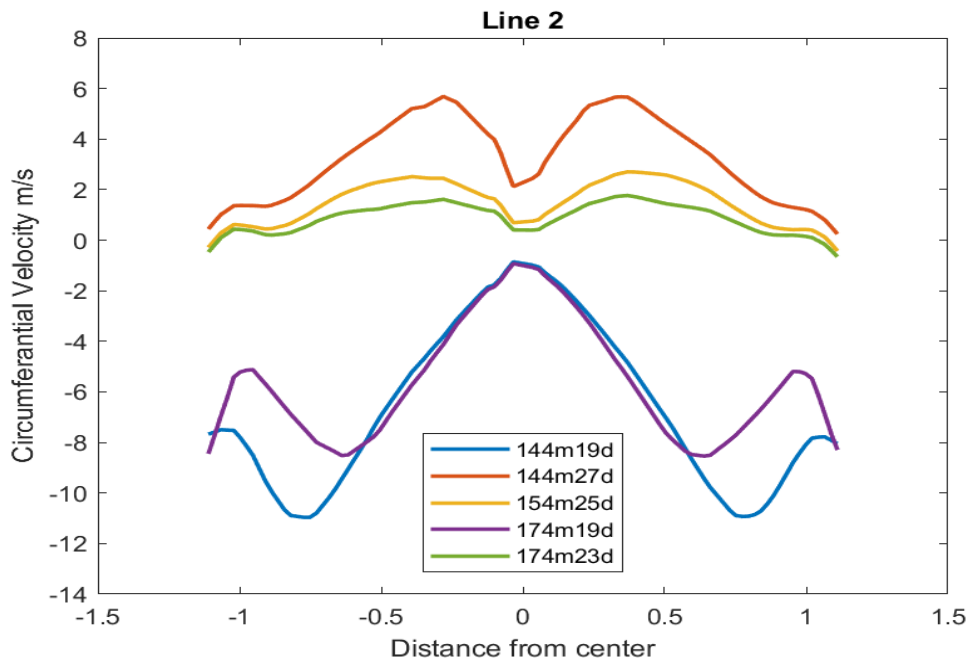
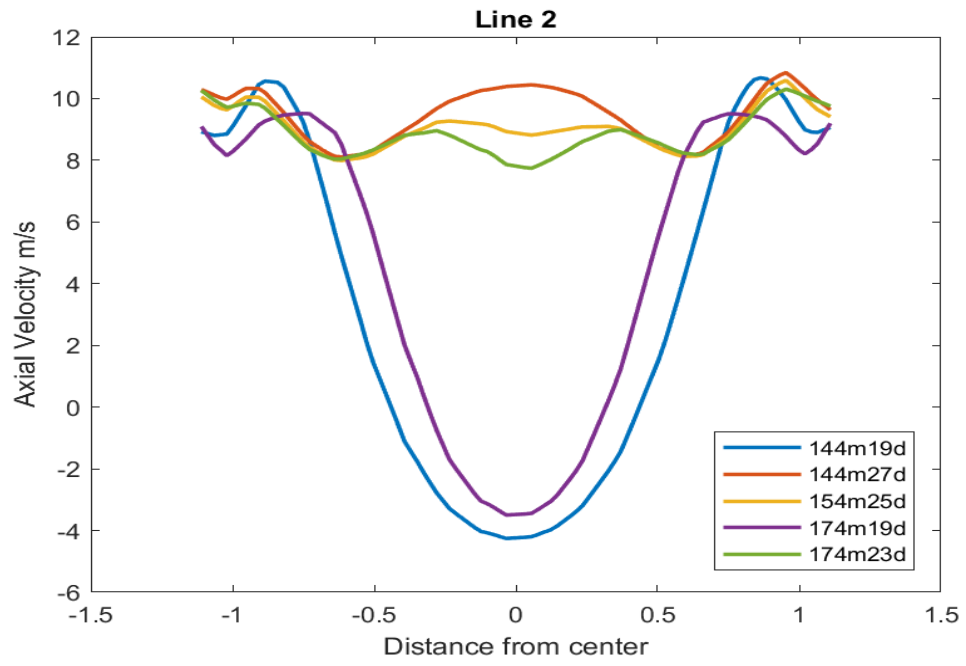


Figure 7.8: Axial and Circumferential Velocity Distribution on Line 2

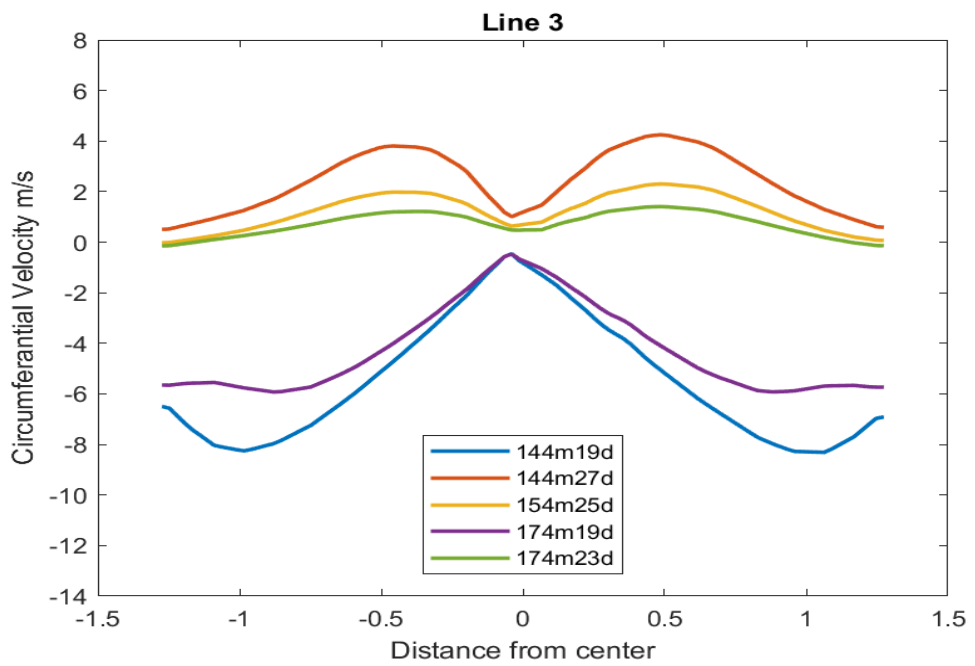
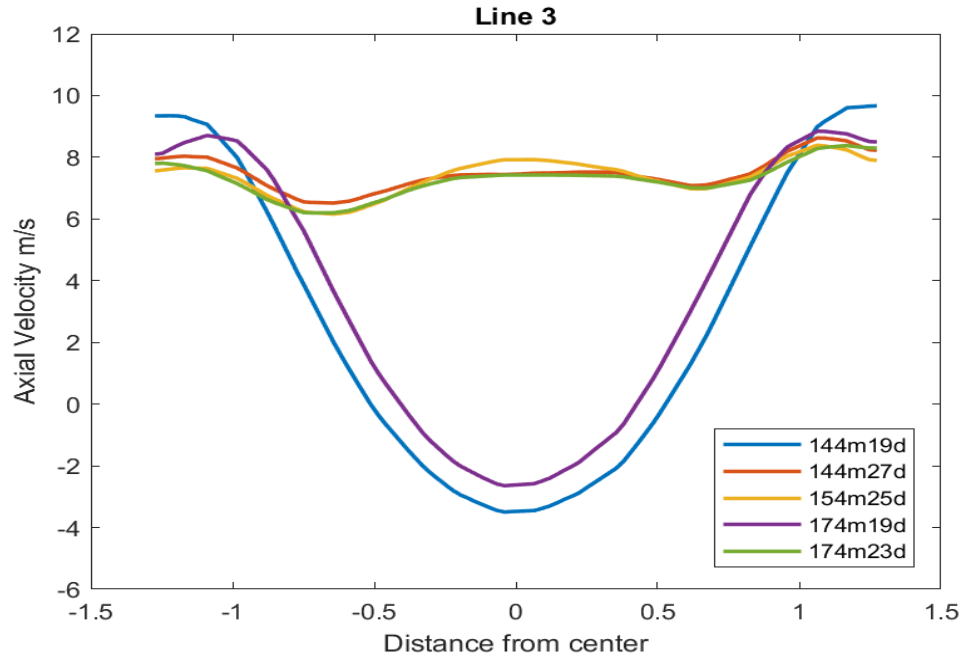


Figure 7.9: Axial and Circumferential Velocity Distribution on Line 3

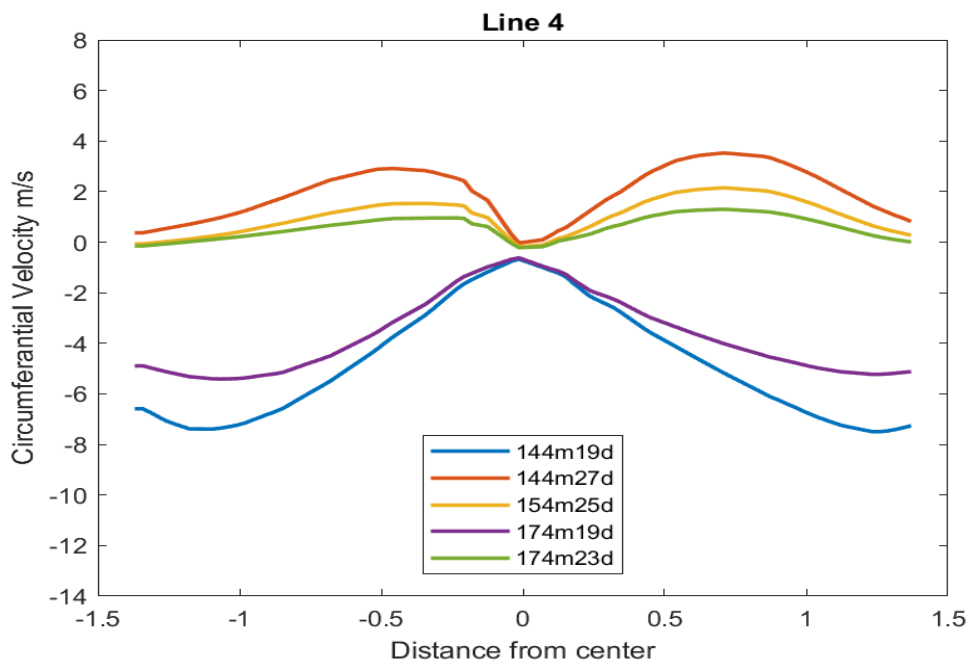
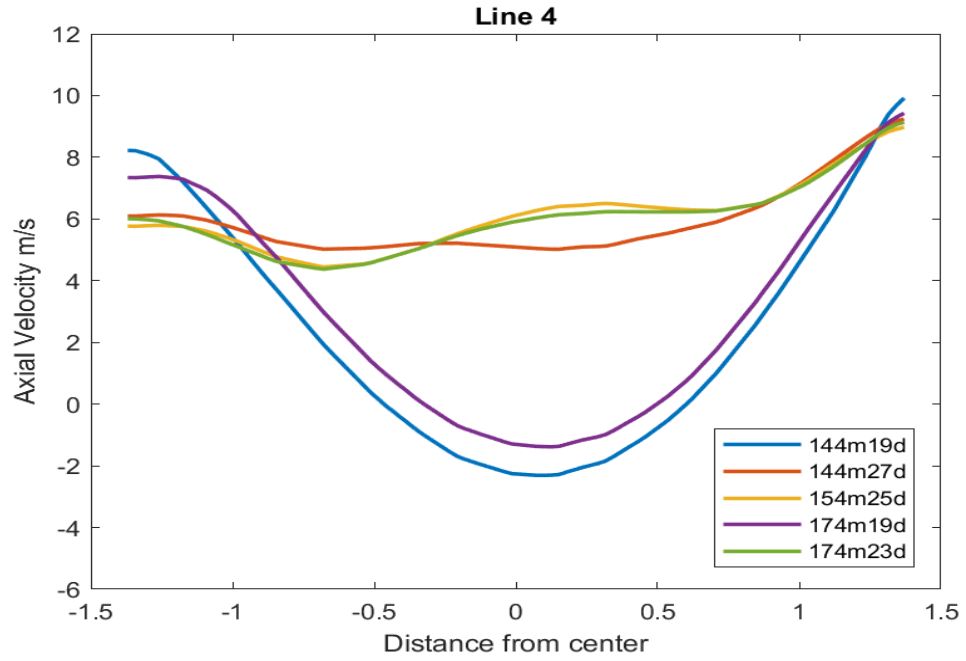


Figure 7.10: Axial and Circumferential Velocity Distribution on Line 4

7.3 PRESSURE RECOVERY FACTOR EFFECT ON TURBINE PERFORMANCE

As it is seen in Figure 7.11, for 144 m head and 19 ° guide vane opening pressure does not increase uniformly from the draft tube inlet to outlet. On the other hand, when Figure 7.11b is examined in 174 m head and 23° guide vane opening pressure

increases uniformly from inlet to outlet. This uniform flow field is observed for all of the operating conditions except 19 ° guide vane opening scenarios.

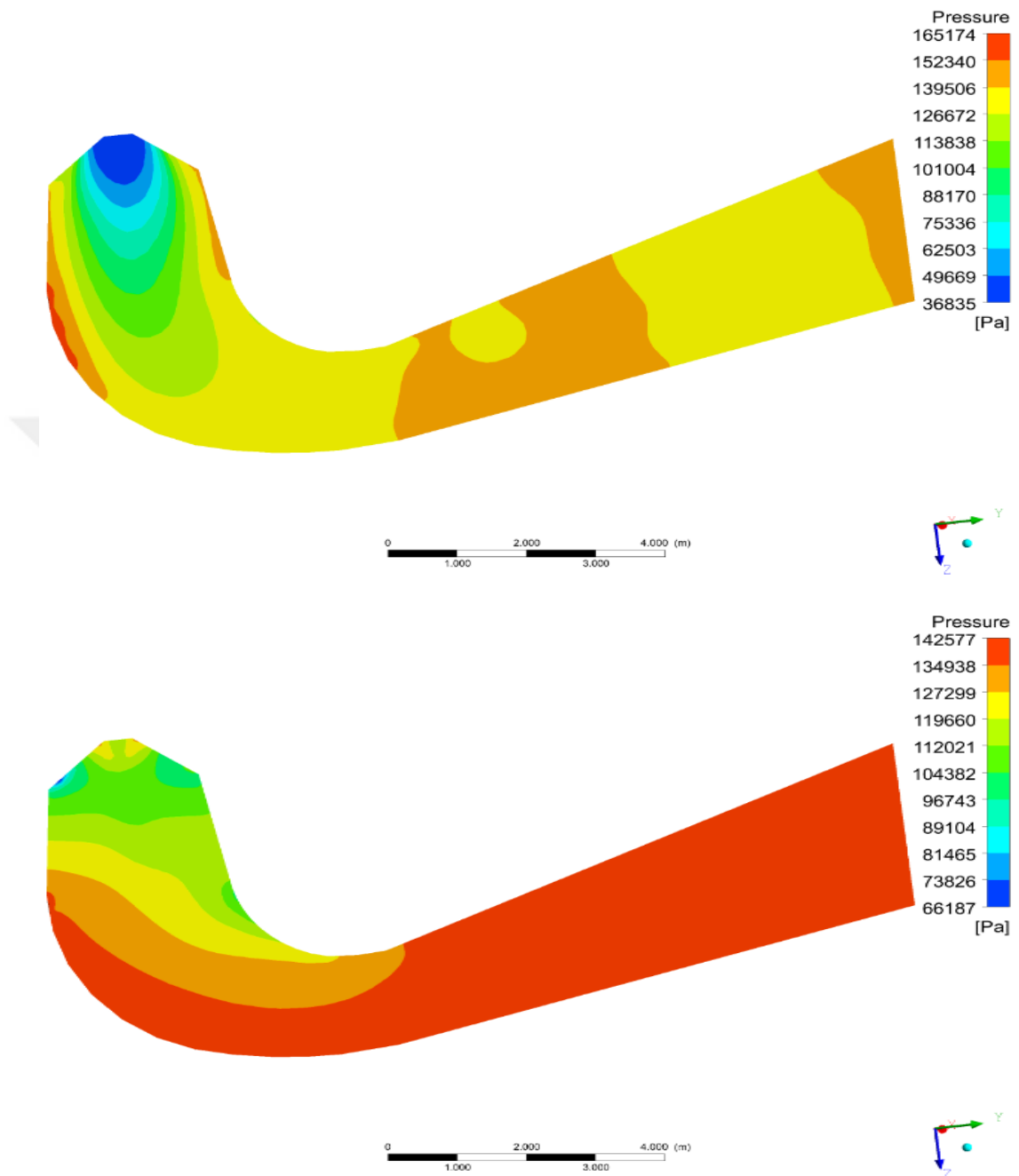


Figure 7.11: Draft tube pressure distribution and vortex structure for (a) 144 m head and 19 ° guide vane opening (b) 174 m head and 23° guide vane opening

Table 7-1: Component Based Efficiency Table and Cp (Full Turbine)

CASE		Head (m)	Guide Vane Opening (degree)	Component Eff.			Draft Tube (C_p)	Full Turbine Efficiency (%)
				Spiral Case and Stay Vanes (%)	Guide Vanes (%)	Runner (%)		
Case 1	144m19d	144	19	99.78	98.76	97.3	0.4	0.904
Case 2	144m27d	144	27	99.58	99.44	96.9	0.81	0.954
Case 3	154m25d	154	25	99.58	99.34	97.1	0.89	0.958
Case 4	174m19d	174	19	99.76	98.92	95.5	0.42	0.916
Case 5	174m23d	174	23	99.62	99.29	96.7	0.91	0.954

As seen in Table 7.1, full turbine efficiency is higher when the pressure increases uniformly (almost 0.95). When there is non-uniform distribution efficiency value decreases to 0.9. As seen in same Table, when C_p value also decreases as full turbine efficiency decreases. Especially for 19° guide vane opening which pressure distribution is not uniform, C_p values decreases to 0.4 which directly affects the full turbine efficiency.

According to the Table 7.2, C_p values of the draft tube are also a function of flow rate. At the operation condition with the volume flow rates that are close to nominal value, C_p increases. Similarly, at the partial load operation, C_p gets smaller. Moreover, net head of the operation has no evident effect on the C_p . The main reason of that reduction is secondary flows and vortices occurring in the cone of the draft tube.

With increasing circumferential velocity, pressure increases near the points of the draft tube wall. Furthermore, the lowest pressure occurs at the draft tube cone center due to the low axial velocity. Since pressure difference between wall sides and around the centerline of the cone, fluid particles start to rotate on the Y-Z plane. This behavior causes secondary vortices on the draft tube cone. The fluid inside the draft

tube cone can be visualized using tangential projection vectors on the YZ -plane given Figure 7.12 to 7.16.

Table 7-2: C_p variations with the Volume Flow Rate

	Case	C_p	Volume Flow Rate (m^3/s)
Case 1	14419d	0.405	25.231
Case 2	14427d	0.808	37.51
Case 3	15425d	0.89	36.473
Case 4	17419d	0.416	28.477
Case 5	17423d	0.91	36.195

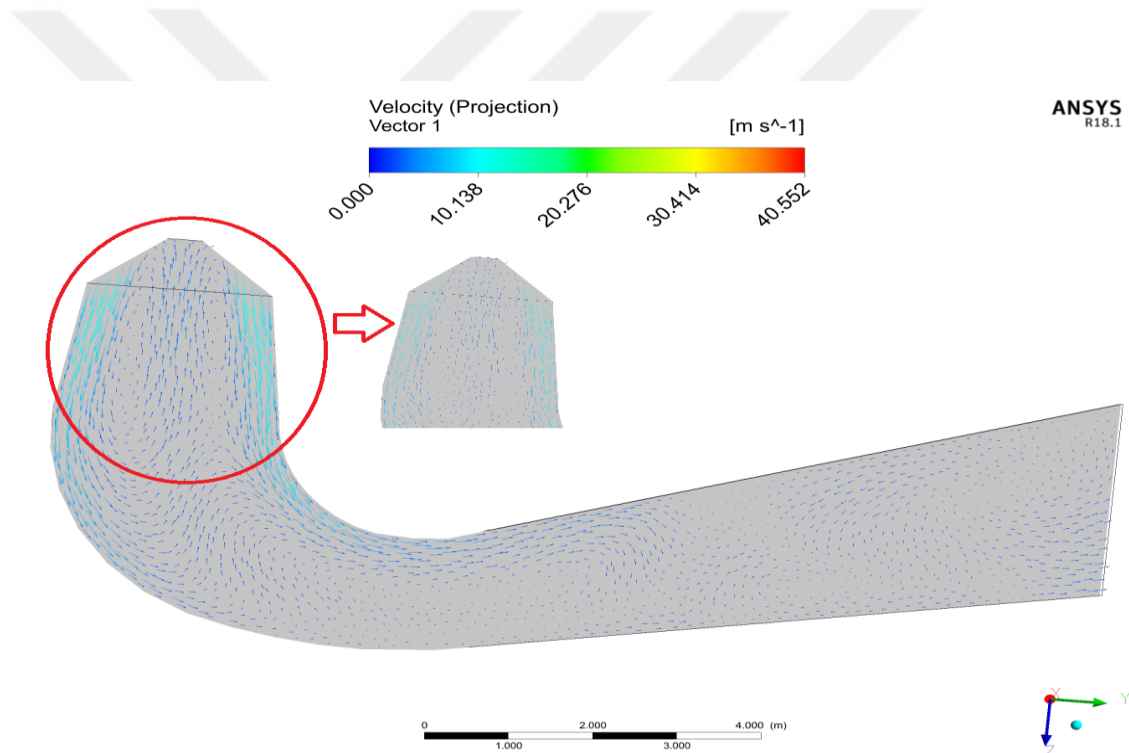


Figure 7.12: Streamlines on the cross-sectional area for 144 meters Head 19 degree Opening

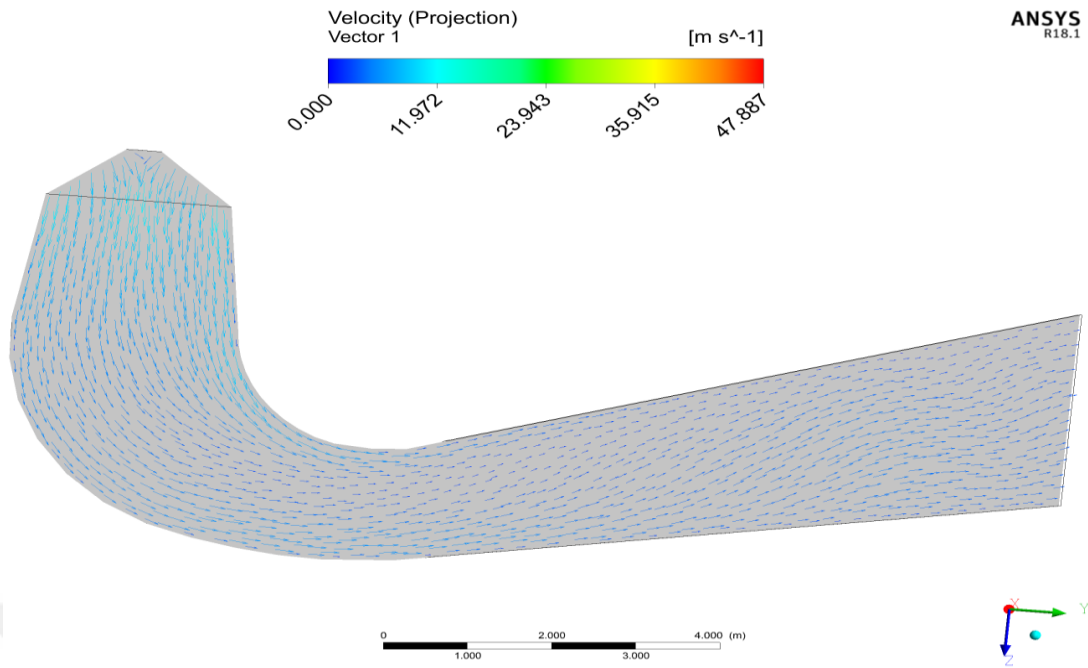


Figure 7.13 : Streamlines on the cross-sectional area for 144 meters Head 27°
Opening

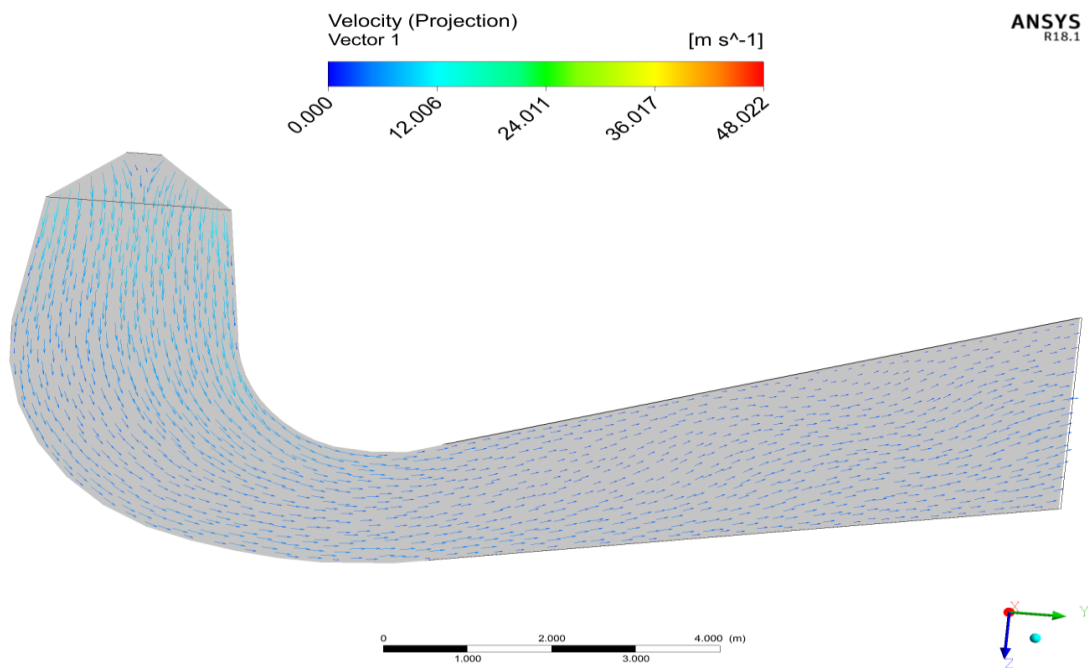


Figure 7.14: Streamlines on the cross-sectional area for 154 meters Head 25°
Opening

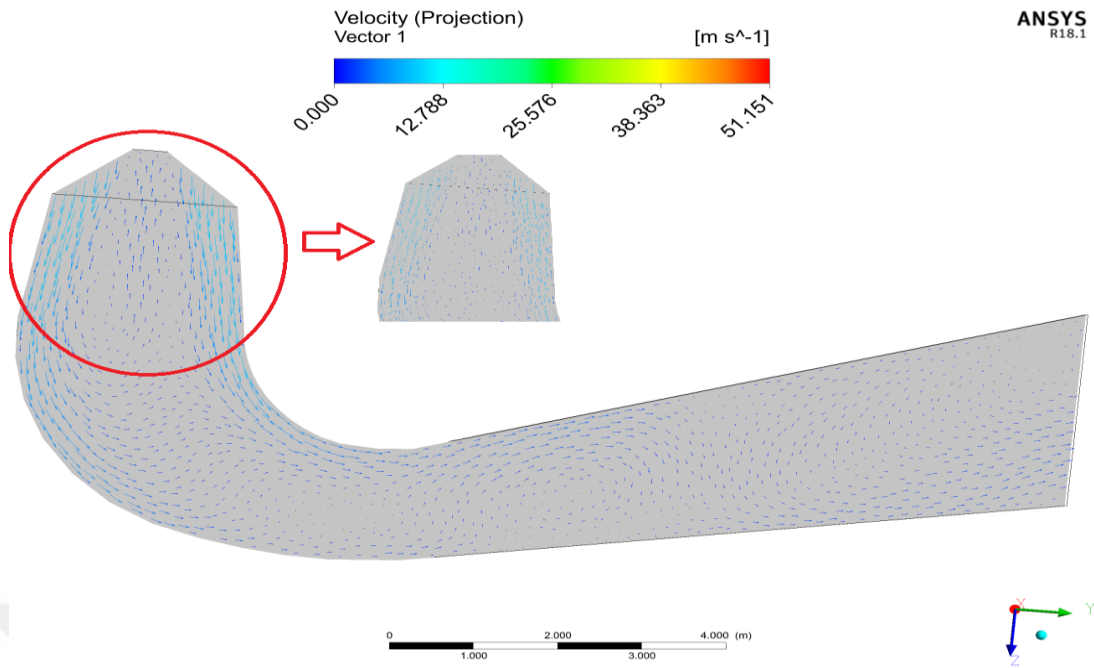


Figure 7.15: Streamlines on the cross-sectional area for 174-meters Head 19° Opening

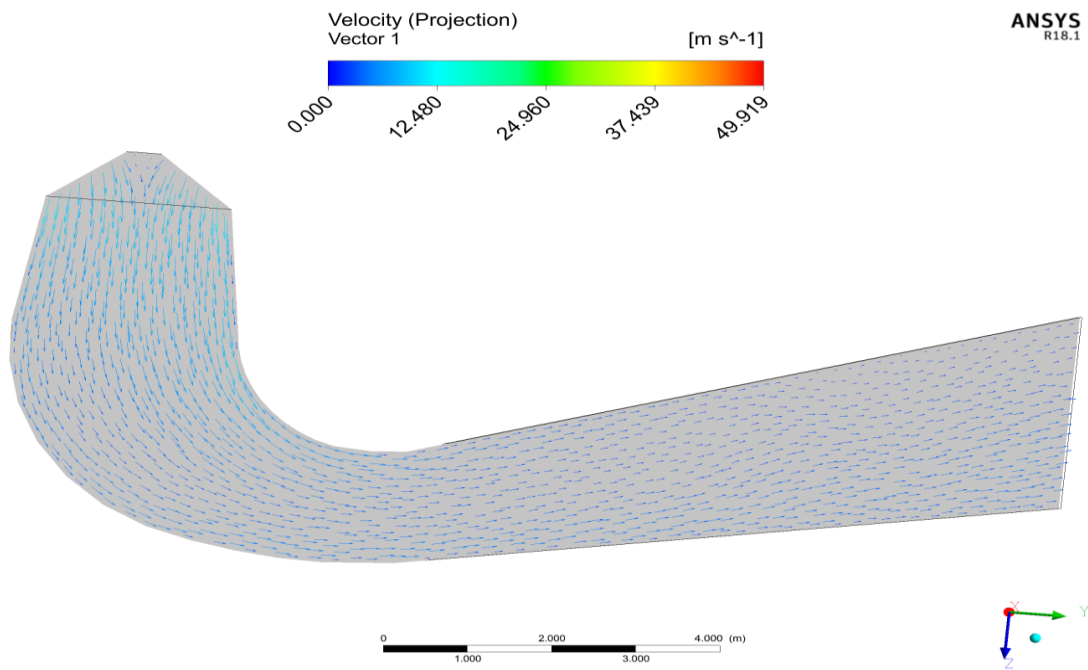


Figure 7.16: Streamlines on the cross-sectional area for 174-meters Head 23° Opening

7.4 COMPARISON OF STEADY AND UNSTEADY RESULTS

The performance table for limit operating conditions are given in the Table 7-3 which include volume flow rate, efficiency, and power. For unsteady analysis, performance values are computed at time = 3.06 s.

Table 7-3: Performance comparison between transient (average) and steady state.

Case		Steady	Transient	Steady	Transient	Steady	Transient
Head (m)	Guide Vane opening	Power (MW)		Volume Flow Rate (m ³ /s)		Efficiency	
	(degree)						
144	19	31.86	32.13	25.27	25.23	0.893	0.904
144	27	49.34	50.41	37.49	37.51	0.933	0.954
154	25	51.56	52.63	36.43	36.47	0.938	0.958
174	19	44.47	44.41	28.56	28.48	0.913	0.916
174	23	57.75	58.77	36.08	36.2	0.939	0.954

According to results, transient simulation performance values are higher than the steady state results. This difference is the result of using different types of interfaces that are used at the guide vane to runner and runner to draft tube. While the frozen rotor type of the interface used in the steady-state simulations, transient rotor-stator type is used for the transient simulations. According to the calculated results, the flow rate is overpredicted in the unsteady analysis when it is compared with steady-state results. [79]

CHAPTER 8

SUMMARY OF CONCLUSIONS, RECOMMENDATIONS AND FUTURE WORK

Project objectives are condition assessments, performance testing, and evaluation of upgrade potential as well as Computational Fluid Dynamics (CFD) analysis of hydroelectric power plants (HPPs). The purpose of this study is to show and analyze opportunities to increase the capacity, energy efficiency of the HPP in sight of the CFD results.

In this thesis, the main objective is to analyze the flow field within the turbines and assess the flow field for irregularities and problems. For this reason, a systematic approach is used which is given in Figure 8.1. In the first part of the study, using the available technical drawings, the runner and guide vanes are connected to other turbine parts such as spiral case and draft tube. Turbine is scanned, and the necessary drawings are obtained from manufacturer drawings. This data is used to create three-dimensional models. These models are then used to analyze the flow within the turbine.

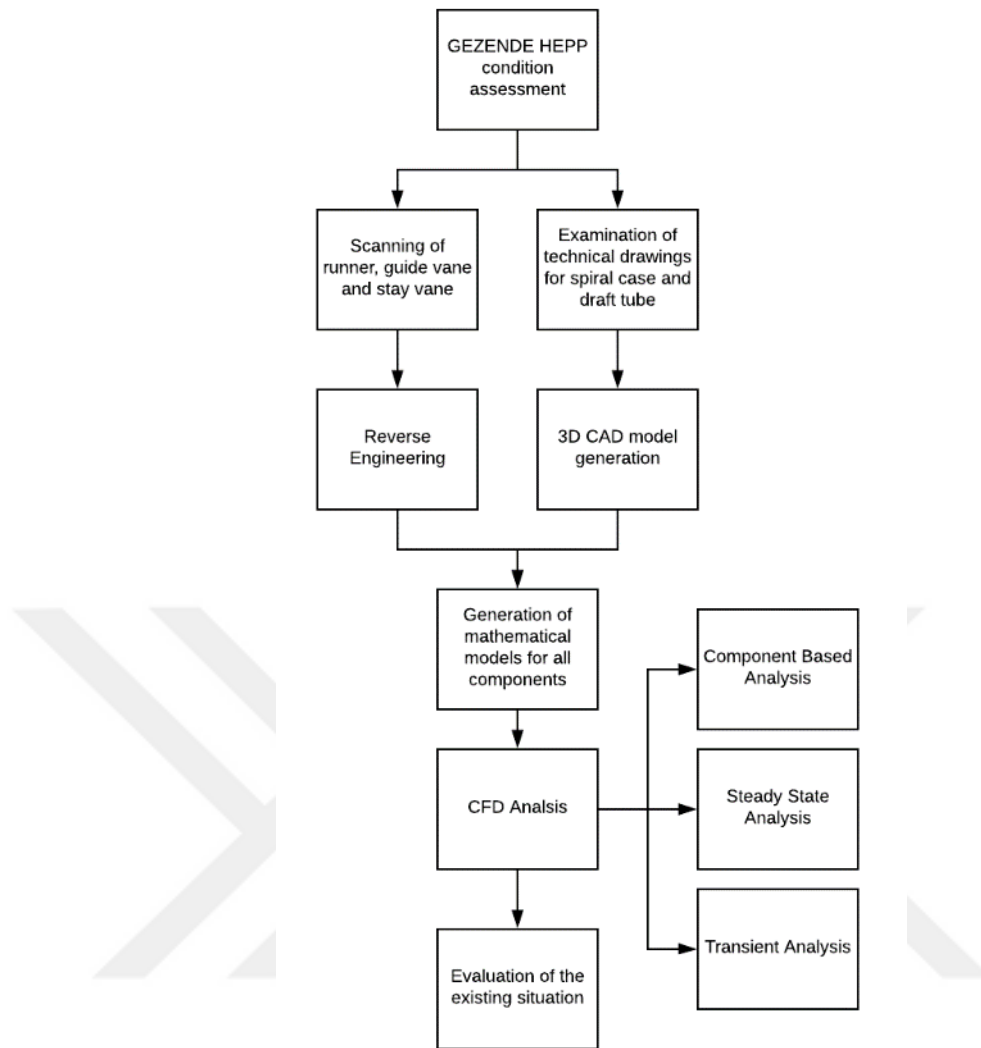


Figure 8.1: Process chart for the CFD study of the Gezende HPP

Steady and unsteady analyses are performed to determine the efficiency and power output of the turbine. A hill chart is generated to investigate the behavior of the turbine at different head and flow rate values.

Cavitation is the biggest problem in the turbines as it reduces the performance, power output, and power plant life. Unsteady state analysis and visualization techniques are used for diagnostics of turbine and enables identification of different cavitation mechanisms. According to the results no cavitation zone is observed in the runner blades. This is one of the most important reason that this turbine is working with high performance for decades.

With the investigation of the circumferential velocity component in the runner inlet and runner exit, it is noticed that there is still circulation at the exit of the runner. Therefore, the turbine cannot use all the hydraulic energy of the water. The

performance of the runner can be increased by using all of the circulation created in the guide vanes. This can be done by changing the conventional runner design to x blade and requires runner renewal.

The biggest reported problem in this turbine is the vibration. Generally, vibration occurs as a result of the cavitation. But as this HPP is almost cavitation-free according to CFD analysis, vibration problems should not be arising due to cavitation. The possible reason of this vibration may be the non-profiled trailing edges of the runner causing non-cavitating vortex. It is suggested that comparing these frequency response analyses to site vibration measurements. The system should be monitored for at least 6 months and leading vibration frequencies should be determined. These frequencies should then be compared to these findings of study to determine the root cause. In case of an indication to runner frequency, then a local at site rehabilitation work to the trailing edge of the runner blades should be considered.

Draft tube swirl is the main reason of the vibration that occurs in the turbine and powerhouse. When pressure pulsations are analyzed at part load vibration may be expected due to draft tube swirl. Magnitude of the circumferential velocity in the draft tube is directly proportional with the vibration. Thus, a measure should be taken to minimize circumferential velocity in the draft tube cone section. A further detail study should be performed for rehabilitation of the cone. The draft tube design has a big impact on efficiency for Gezende HPP, especially at part load.

For part load operation, the value of C_p , thus efficiency can be increased by water jet injection at the cone because when the axial velocity of the flow at the draft tube cone increases, C_p value increases. This will have a positive impact on draft tube flow stability even full turbine efficiency.

The CFD results show that at the full load condition HPP has 93.27 % efficiency with 51.56 MW power output. According to the literature, when well designed, a Francis turbine can capture 93–95% of the energy in the water. Therefore, the efficiency value at the full load condition is close to state of the art for Gezende HPP.

REFERENCES

- [1] Wuebbles, D.J., Sanyal, S., Air Quality in a Cleaner Energy World, Current Pollution Reports, vol 1, pp: 117-129, 2014. DOI: 10.1007/s40726-015-0009-x
- [2] WorldEnergyCouncil, website:
<https://www.worldenergy.org/data/resources/resource/hydropower/>
- [3] Nuner, C., Hydropower, explained, National Geographic, website:
<https://www.nationalgeographic.com/environment/global-warming/hydropower/>
- [4] Teran, L.A., Larrahondo, F.J., Rodrigues S.A., Performance improvement of a 500-kW Francis turbine based on CFD, Renewable Energy, vol: 96, pp: 977-992, 2016.
- [5] Thakur, TN. Rehabilitation of hydropower equipment, Third international conference of power development in Afro Asian Countries, Kathmandu, pp. 538–45, Nepal;1996.
- [6] Celebioglu, K., Aradag, S., Ayli, E., Altintas, B., Rehabilitation of Francis Turbines of Power Plants with Computational Methods, Hittite Journal of Science and Engineering, vol 5(1), pp: 37-48, 2018.
- [7] Jackson RJ, Lawrence RA, Rudd SR. Refurbishment of turbogenerators for plant life extension, International Conference on Refurbishment of Power Station Electrical Plant; pp. 160–64, 7–8 Nov. 1988
- [8] Mack, R., Gola, B., Smertnig, M., Wittwer, B., Meusbürger, P., Modernization of vertical Pelton turbines with the help of CFD and model testing, 27th IAHR Symposium on Hydraulic Machinery and Systems (IAHR 2014), vol: 22, 2014.
- [9] Vitvar, M., Kaplan turbine uprating at Orlik power plant, Water Power, vol: 31 (10), pp: 24-26, 1989.
- [10] Manjean, J.M., Jouve, J., Ferme, J. M., Electronic speed governing system for the Pierre Eybesse plant, Water Power Dam Construction, pp: 8-11, 1990.
- [11] Ferme J, Nicolas J. Digital speed governor for Vainden., International conference on uprating and refurbishing hydropower plant-III, Water Power Dam Construction; p. 351–57, Oct. 1991.
- [12] Rahi, O.P., Chandel, A.K., Refurbishment, and upgrading of hydropower plants- a literature review, Renewable, and Sustainable Energy Reviews, vol: 48, pp: 726-737, 2015.
- [13] Garcia, M.J., Boulanger, P., Barbosa, J., Betancur, J., Quintero, B., Castaneda, L., Betancur, G.R., Application of the reverse engineer in the modelling of a Francis

turbine in a hydroelectric mini power station, 23rd ISPE International Conference on CAD/CAM Robotics and Factories of the Future, 2007.

[14] Kaplan, A., Cetinturk, H., Celebioglu, K., Aradag, S., Reverse Engineering Design of a Hydraulic Turbine Runner, Proceedings of the World Congress on Engineering, Vol:2, 1-3 July 2015, London, UK.

[15] Celebioglu, K., Kaplan, A., Development, and implementation of a methodology for reverse engineering design of Francis turbine runners, Pamukkale University Journal of Engineering Sciences, doi:10.5505/pajes.2018.43959 (Just accepted).

[16] Zivkovic, S., Cerce, L., Kostic, J., Majstorovic, V., Kramar, D., Reverse engineering of turbine blades Kaplan's type for small hydroelectric power station, 15th CIRP Conference on Computer Aided Tolerancing, vol: 75, pp: 379-384, 2018.

[17] Ciocănea, A., Nicolaie, S., Băbutanu, C., Reverse engineering for the rotor blades of a horizontal axis moci-hydrokinetic turbine, Energy Procedia, vol: 112, pp: 35-42, 2017.

[18] Demirel, G., Acar, E., Celebioglu, K., & Aradag, S. (2017). CFD-driven surrogate-based multi-objective shape optimization of an elbow type draft tube. International Journal of Hydrogen Energy, 42(28), 17601–17610. <https://doi.org/10.1016/j.ijhydene.2017.03.082>

[19] G. I. Krivchenko., Hydraulic Machines: Turbines and Pumps., Mir Publishers, Moscow,(1986).

[20] Ayli, E., Celebioglu, K., & Aradag, S. (2016). Determination and generalization of the effects of design parameters on Francis turbine runner performance. Engineering Applications of Computational Fluid Mechanics, 10(1), 545–564. <https://doi.org/10.1080/19942060.2016.1213664>

[21] THAPA, B. S., TRIVEDI, C., & DAHLHAUG, O. G. (2016). Design and development of guide vane cascade for a low speed number Francis turbine. Journal of Hydrodynamics, 28(4), 676–689. [https://doi.org/10.1016/S1001-6058\(16\)60648-0](https://doi.org/10.1016/S1001-6058(16)60648-0)

[22] Çelebioğlu, K. (2020). Pamukkale Üniversitesi Mühendislik Bilimleri Dergisi Pamukkale University Journal of Engineering Sciences Numerical investigation of the effects of design parameters on hydraulic turbine guide vane design Tasarım parametrelerinin hidrolik türbin ayar kanadı tasarımına etkilerinin sayısal olarak incelemesi. 26(4), 666–673. <https://doi.org/10.5505/pajes.2019.70850>

[23] Akin, H., Aytac, Z., Ayancik, F., Ozkaya, E., Arioz, E., Celebioglu, K., & Aradag, S. (2013). A CFD aided hydraulic turbine design methodology applied to Francis turbines. International Conference on Power Engineering, Energy and Electrical Drives, (May 2013), 694–699. <https://doi.org/10.1109/PowerEng.2013.6635694>

[24] Ayancik, F., Aradag, U., Ozkaya, E., Celebioglu, K., Unver, O., & Aradag, S. (2013). Hydroturbine Runner Design and Manufacturing. International Journal of Materials, Mechanics and Manufacturing, (November 2012), 162–165. <https://doi.org/10.7763/ijmmm.2013.v1.35>

[25] Manoj Kumar Shukla, Rajeev Jain, Vishnu Prasad, and S Shukla. Cfd analysis of 3-d flow for francis turbine. Int. J. Mech. Eng, 2:93–100, 2011.

- [26] Jain, S., Saini, R. P., & Kumar, A. (2010). CFD Approach for Prediction of Efficiency of Francis Turbine, India
- [27] Yao, Z., Xiao, R., Wang, F., & Yang, W. (2015). Numerical Investigation of Cavitation Improvement for a Francis Turbine, 9th International Symposium on Cavitation (CAV2015). doi:10.1088/1742-6596/656/1/012075
- [28] Choi, H. J., Zullah, M. A., Roh, H. W., Ha, P. S., Oh, S. Y., & Lee, Y. H. (2013). CFD Validation of performance Improvement of a 500 kW Francis Turbine, *Renewable Energy* 54 (2013), 101-123
- [29] Nicolle, J., Morissette, J. F., & Giroux A. M., Transient CFD Simulation of a Francis Turbine Startup, 26th IAHR Symposium on Hydraulic Machinery and Systems, 2012. doi:10.1088/1755-1315/15/6/062014
- [30] Kavurmaci, B., Akin, H., Ayli, E., Celebioglu, K., & Aradag, S. (2013). Design of an experimental test stand for francis type hydraulic turbines. *International Conference on Power Engineering, Energy and Electrical Drives*, (February), 876–880. <https://doi.org/10.1109/PowerEng.2013.6635725>
- [31] IEC 60193 (1999). International Standart, IEC 60193, Hydraulic turbines, pumps and pump turbines- Model acceptance tests, Amerika
- [32] Li SC. Cavitation of hydraulic machinery. Imperial College Press; 2000.
- [33] Avellan, F. (2004). Introduction to cavitation in hydraulic machinery. 6th Int. Conf. on Hydraulic Machinery and Hydrodynamics, (January 2004), 11–22. Retrieved from http://mmut.mec.upt.ro/mh/Conferinta_MH/102Avellan.pdf
- [34] Escaler, X., Egusquiza, E., Farhat, M., Avellan, F., & Coussirat, M. (2006). Detection of cavitation in hydraulic turbines. *Mechanical Systems and Signal Processing*, 20(4), 983–1007. <https://doi.org/10.1016/j.ymsp.2004.08.006>
- [35] Escaler, X., Farhat, M., Ausoni, P., & Egusquiza, E. (2006). Cavitation monitoring of hydroturbines : Tests in a Francis turbine model. 6th International Symposium on Cavitation, September, 1–5.
- [36] Zuo, Z. G., Liu, S. H., Liu, D. M., Qin, D. Q., & Wu, Y. L. (2015). Numerical analyses of pressure fluctuations induced by inter blade vortices in a model Francis turbine. *Journal of Hydrodynamics*, 27(4), 513–521. [https://doi.org/10.1016/S1001-6058\(15\)60511-X](https://doi.org/10.1016/S1001-6058(15)60511-X)
- [37] Ausoni, P., Farhat, M., Escaler, X., Egusquiza, E., & Avellan, F. (2007). Cavitation influence on von Kármán vortex shedding and induced hydrofoil vibrations. *Journal of Fluids Engineering, Transactions of the ASME*, 129(8), 966–973. <https://doi.org/10.1115/1.2746907>
- [38] Celebioglu, K., Altintas, B., Aradag, S., & Tascioglu, Y. (2017). Numerical research of cavitation on Francis turbine runners. *International Journal of Hydrogen Energy*, 42(28), 17771–17781. <https://doi.org/10.1016/j.ijhydene.2017.03.180>
- [39] Wack, Jonas & Riedelbauch, Stefan. (2017). Numerical simulation of a cavitating draft tube vortex rope in a Francis turbine at part load conditions for different σ -levels. *Journal of Physics: Conference Series*. 813. 012019. 10.1088/1742-6596/813/1/012019.
- [40] Kang, Z., Feng, C., Liu, Z., Cang, Y., & Gao, S. (2017). Analysis of the incipient cavitation noise signal characteristics of hydroturbine. *Applied Acoustics*, 127, 118–125. <https://doi.org/10.1016/j.apacoust.2017.05.029>

- [41] Vu, T., Nennemann, B., Ausoni, P., Farhat, M., & Avellan, F. (2007). Unsteady CFD Prediction of von Kármán Vortex Shedding in Hydraulic Turbine Stay Vanes. *Hydro 2007*, January. [http://infoscience.epfl.ch/record/113757/files/Ausoni et al.pdf](http://infoscience.epfl.ch/record/113757/files/Ausoni_et_al.pdf) C1 - Granada, Spain%5Cn<http://infoscience.epfl.ch/record/113757>
- [42] Li, S. (2015). Tiny bubbles challenge giant turbines: Three gorges puzzle. *Interface Focus*, 5(5), 1–25. <https://doi.org/10.1098/rsfs.2015.0020>
- [43] D’Agostini Neto, A., Gissoni, H., Gonçalves, M., Cardoso, R., Jung, A., & Meneghini, J. (2016). Engineering diagnostics for vortex-induced stay vanes cracks in a Francis turbine. *IOP Conference Series: Earth and Environmental Science*, 49(7). <https://doi.org/10.1088/1755-1315/49/7/072017>
- [44] Dou, H., Niu, L., & Cao, S. (2014). Effects of tangential velocity distribution on flow stability in a draft tube. *Journal of Thermal Science*, 23(5), 446–453. <https://doi.org/10.1007/s11630-014-0728-0>
- [45] KC, A., Lee, Y. H., & Thapa, B. (2016). CFD study on prediction of vortex shedding in draft tube of Francis turbine and vortex control techniques. *Renewable Energy*, 86, 1406–1421. <https://doi.org/10.1016/j.renene.2015.09.041>
- [46] J. Gomes, P., Favrel, A., Nicolet, C., & Avellan, F. (2019). Part load resonance risk assessment of francis hydropower units. 13th European Turbomachinery Conference on Turbomachinery Fluid Dynamics and Thermodynamics, ETC 2019, June.
- [47] Wack, J., & Riedelbauch, S. (2015). Numerical simulations of the cavitation phenomena in a Francis turbine at deep part load conditions. *Journal of Physics: Conference Series*, 656(1). <https://doi.org/10.1088/1742-6596/656/1/012074>
- [48] Østby, P. T. K., Billdal, J. T., Sivertsen, K., Haugen, B., & Dahlhaug, O. G. (2016). Dynamic Stresses In High Head Francis Turbines. June.
- [49] Luna-Ramírez, A., Campos-Amezcuca, A., Dorantes-Gómez, O., Mazur-Czerwicz, Z., & Muñoz-Quezada, R. (2016). Failure analysis of runner blades in a Francis hydraulic turbine - Case study. *Engineering Failure Analysis*, 59, 314–325. <https://doi.org/10.1016/j.engfailanal.2015.10.020>
- [50] Anup, K. C., Thapa, B., & Lee, Y. H. (2014). Transient numerical analysis of rotor-stator interaction in a Francis turbine. *Renewable Energy*, 65, 227–235. <https://doi.org/10.1016/j.renene.2013.09.013>
- [51] Javadi, A., & Nilsson, H. (2017). Active flow control of the vortex rope and pressure pulsations in a swirl generator. *Engineering Applications of Computational Fluid Mechanics*, 11(1), 30–41. <https://doi.org/10.1080/19942060.2016.1235515>
- [52] Resiga, R., Vu, T., Muntean, S., Academy, R., & Ciocan, G. D. (2006). Jet Control of the Draft Tube Vortex Rope in Francis Turbines at Partial Discharge. May 2014.
- [53] Foroutan, H., & Yavuzkurt, S. (2014). Flow in the simplified draft tube of a Francis turbine operating at partial load-Part II: Control of the vortex rope. *Journal of Applied Mechanics, Transactions ASME*, 81(6). <https://doi.org/10.1115/1.4026818>
- [54] Zhou, X., Wu, H. G., & Shi, C. Z. (2019). Numerical and experimental investigation of the effect of baffles on flow instabilities in a Francis turbine draft

- tube under partial load conditions. *Advances in Mechanical Engineering*, 11(1), 1–15. <https://doi.org/10.1177/1687814018824468>
- [55] Wei, Q. S., Choi, Y. D., & Zhu, B. S. (2012). Application of J-groove to the suppression of swirl flow in the draft tube of a francis hydro turbine. *IOP Conference Series: Earth and Environmental Science*, 15(PART). <https://doi.org/10.1088/1755-1315/15/2/022017>
- [56] Turbine, F. (2015). A STUDY ON SUPPRESSION OF CAVITATION SURGE BY J-GROOVES OF A AJK2015-09163. April.
- [57] Garcia R., M. J., Boulanger, P., Barbosa P., J., Betancur M., J., Quintero A., B., Castaneda, L. F., Betancur G., G. R., (2006). Application of the Reverse Engineer in the Modelling of a Francis Turbine ina Hydroelectric Minipower Station, Betancur G., G. R., 23rd ISPE International Conference on CAD/CAM Robotics and Factories of the Future.
- [58] Chen, L. C., Lin, G. C. I., (2000). Reverse Engineering in the Design of Turbine Blades – A Case Study in Applying the MAMDP, Robotics and Computer Integrated Manufacturing 16
- [59] Çelebioğlu, K., & Kaplan, A. (2019). Development and Implementation of a Methodology for Reverse Engineering Design of Francis Turbine Runners. *Pamukkale University Journal of Engineering Sciences*, 25(4), 430–439. <https://doi.org/10.5505/pajes.2018.43959>
- [60] Maruzewski, P., Hayashi, H., Munch, C., Yamaishi, K., Hashii, T., Mombelli, H. P., Avellan, F. (2010). Turbulence modeling for Francis turbine water passages simulation. *IOP Conference Series: Earth and Environmental Science*, 12(September), 012070. <https://doi.org/10.1088/1755-1315/12/1/012070>
- [61] Arayici, Y., Hamilton, A., Gamito, R., Modelling 3D Scanned Data to Visualise and Analyse the Built Environment for Regeneration, *Sruveying and Built Enviroment*, vol: 17 (2), pp:7-28,2006.
- [62] Portable Laser Scanner Romer Absolute Arm, Hexagon Manufacturing Intelligence, web page: <https://www.hexagonmi.com/>
- [63] Nourbakhsh, A., Razavi, O. S., Khodabakhsh, H., Mehrabadi, A., New Approach for Hydraulic Design of Francis Runner Based on Empirical Correlation, *International Conference on Small Hydropower*,2007
- [64] A. Karimi, F. Avellan, Comparison of erosion mechanisms in different types of cavitation, *Wear*, Volume 113, Issue 3, 1986, Pages 305-322, ISSN 0043-1648, [https://doi.org/10.1016/0043-1648\(86\)90031-1](https://doi.org/10.1016/0043-1648(86)90031-1).
- [65] Custer, C. (n.d.). Simulation of the Francis-99 Hydro Turbine During Steady and Transient Operation. 012003. <https://doi.org/10.1088/1742-6596/755/1/011001>
- [66] T. Von Karman. “Some remarks on the statistical theory of turbulence”. *Proc. 5th Int. Congr. Appl. Mech*, Cambridge, MA, 347, 1938.
- [67] J. O. Hinze. “Turbulence”. McGraw-Hill, New York, 1959.
- [68] G. T. Chapman and M. Tobak. “Observations, Theoretical Ideas, and Modeling of Turbulent Flows — Past, Present and Future, in *Theoretical Approaches to Turbulence*”. Dwoyer et al.(eds), Springer-
- [69] Heskestad, G., & Olberts, D. R. (1960). Influence of trailing-edge geometry on hydraulic-turbine-blade vibration resulting from vortex excitation. *Journal of*

- Engineering for Gas Turbines and Power, 82(2), 103–109.
<https://doi.org/10.1115/1.3672718>
- [70] Knapp, R.T., Dally, J.W., and Hammitt, F.G. Cavitation. McGraw-Hill, New York, 1970
- [71] Kaplan A., Reverse engineering design and rehabilitation of a francis turbine runner, MSc Thesis, 2016.
- [72] Celebioglu., K., Aradag, S., Altintas, B., Ayli, E., Rehabilitation of Francis Turbines of Power Plants with Computational Methods, Hittite J Sci Eng., ISSN 2148 4171, 2017.
- [73] Billdal J. T., “The X-factor”, International Water Power and Dam Construction. August 2006.
- [74] Celic, D., Ondracka, H., The influence of disc friction losses and labyrinth losses on efficiency of high head Francis turbine, Journal of Physics: Conference Series 579 (2015) 012007, doi:10.1088/1742-6596/579/1/012007.
- [75] Feng, J., Luo, X., Zhu, G., Wu, G., Investigation on disk friction loss and leakage effect on performance in a Francis model turbine, Advances in Mechanical Engineering, vol (9), pp: 1-10, 2017
- [76] J. Osterwalder & L. Hippe (1984) Guidelines For Efficiency Scaling Process Of Hydraulic Turbomachines With Different Technical Roughnesses of Flow Passages, Journal of Hydraulic Research, 22:2, 77-102, DOI: 10.1080/00221688409499386
- [77] ANSYS, “ANSYS CFX – Solver Modelling Guide,” Knowl. Create. Diffus. Util., vol. 15317, no. November, pp. 724-746, 2011.
- [78] Zhang, Y., Liu, K., Xian, H., & Du, X. (2018). A review of methods for vortex identification in hydroturbines. Renewable and Sustainable Energy Reviews, 81(March 2017), 1269–1285. <https://doi.org/10.1016/j.rser.2017.05.058>
- [79] ANSYS, “ANSYS CFX – Solver Modelling Guide,” Knowl. Create. Diffus. Util., vol. 15317, no. November, pp. 724-746, 2011.
- [80] Apacoglu, B., Cfd analyses of uncontrolled and controlled laminar and turbulent flows over a circular cylinder, MSc Thesis, TOBB ETU, 2017